ETH zürich D PHYS

Benjamin Neubauer

Optimization of high-overtone bulk acoustic resonators for multimode microwave to optical transduction

Master's thesis
Department of Physics
ETH Zürich

Supervision
Prof. Yiwen Chu
Dr. Samuel Pautrel

May 13, 2025

Abstract

A major challenge in realizing distributed quantum networks is linking superconducting circuits to optical fibers. Quantum transducers bridging microwave and optical frequencies are an essential building block in this effort. Their operation requires an efficient nonlinear interaction to mediate frequency conversion of single quanta with near unity efficiency. A popular choice is to use a parametrically enhanced optomechanical interaction between optical and acoustic resonator modes for this. Also coupling these acoustic modes to superconducting circuits via a resonant piezoelectric interaction enables full transduction between the microwave and optical platforms. This work investigates several aspects of a transducer design with a high-overtone bulk acoustic resonator (HBAR). The peculiarity of this design is that the frequency spacing between acoustic eigenmodes of the HBAR is smaller than the transducer bandwidth. This requires operation in the multimode regime. In the first part of the thesis, we simulate the time dynamics of the microwave to optical transduction protocol in different device geometries. We find that achieving unity transduction efficiency requires uniform acoustic mode spacing, as well as symmetry between the electromechanical and optomechanical coupling strength distributions. The second part of the thesis experimentally tests the electromechanical interaction of transducers in the weak coupling regime. By recording the radiation of a qubit excitation into the acoustic modes, we derive values for coupling strengths and bounds on phonon coherence times.

Contents

1. Introduction

Circuit quantum electrodynamics (cQED) is one of the leading fields for quantum information processing [1]. The Josephson junction in transmon qubits grants easy access to a quantum nonlinearity and allows for high fidelity creation of quantum states in superconducting circuits [2]. Since cQED systems are operated in the microwave regime, they need to be cooled to millikelvin temperatures in order to inhibit decoherence from blackbody radiation of the environment. This makes transportation of quantum information over longer distances on this platform a challenging task [3]. A more suitable platform for the transport of fragile quantum states are optical fibres, where creation of entanglement over distances of 100 km has been shown [4]. Quantum transducers between these platforms are thus essential building blocks for distributed quantum networks [5, 6]. Specifically, microwave to optical transducers can be used to create long range entanglement between two remote microwave superconducting processors [7, 8]. In addition, microwave to optical quantum transduction could provide a scalable tool to create quantum states of light for applications in quantum metrology [9], or quantum algorithms such as boson sampling [10].

In general, a quantum transducer can be modeled as a chain of bosonic quantum channels, with the end nodes coupled to the external platforms [11]. By establishing linear beam-splitter type couplings between the channels, a single photon can be directly transduced. There is also the possibility for a more complicated coupling scheme based on squeezing and quantum teleportation [12], but here we will focus on the direct method. Important figures of merit for a quantum transducer are the transduction efficiency, the bandwidth, and the added noise [8], which can be combined in a single metric, the quantum capacity [13]. The latter quantifies the amount of quantum information of a transduced signal, which is only nonzero for one way transduction if at least 50 % transduction efficiency is achieved. To prove experimentally that a quantum state has been transduced, quantum features of light, such as sub-Poissonian statistics or negativity of the Wigner-function have to be shown [14]. This still remains a challenge in the field.

When coupling microwaves to optical fields, more than four orders of magnitude in frequency between the microwave (10 GHz) and optical (100 THz) regime must be bridged. To establish linear coupling between channels at these very different frequencies, a nonlinear parametric interaction is usually employed. There are various physical platforms which try to achieve this. In an electro-optic platform, which mediates a direct interaction between microwaves and optical light, entanglement has been shown in the continuous variable regime [15]. Another unique approach is to use transitions of Rb-atoms in the optical regime combined with transitions between Rydberg states in the microwave regime to mediate transduction [16]. More commonly however, mechanical oscillators are employed as intermediaries between the microwave and optical regimes, as they come

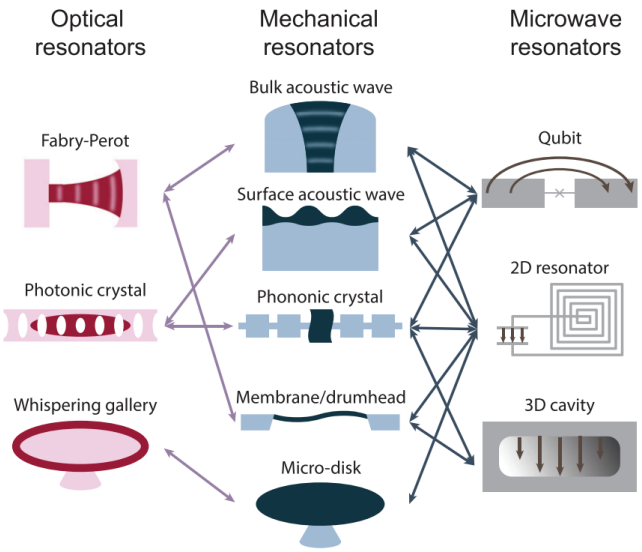

Figure 1.1.: Different types of optical, mechanical, and microwave resonators that have been used in experimental demonstrations. Arrows indicate demonstrated couplings between systems. [14]

in a variety of shapes and coupling possibilities. Figure 1.1 shows an overview of different experimentally demonstrated couplings between microwave, mechanical and optical resonators [14]. Approaching the hybrid system from the optical side, optomechanical crystals are a well established way of achieving strong optomechanical interaction by confining the acoustic and optical modes to the same volume [17]. Simultaneous coupling to a superconducting qubit can be achieved by means of piezoelectric interaction, allowing microwave to optical transduction [18]. These systems suffer severely from heating due to laser light partaking in the optomechanical interaction. For this reason, efforts are put into extending these crystals into two dimensions, making it easier for heat to dissipate [19]. Drumhead resonators are another mechanical platform used for transduction. They can couple to an optical Fabry-Pérot resonator through moving dielectric boundaries, and simultaneously to a superconducting microwave resonator by modifying its capacitance. Optical qubit readout has been demonstrated on this platform by transducing the microwave pulse of dispersive qubit readout [20]. These drumhead resonators usually have resonance frequencies in the MHz domain, which allows them to reach very high quality factors [21]. The downside is that active cooling is necessary to suppress thermal noise.

In the hybrid quantum systems (HyQu) group at ETH Zurich, we want to use a high-overtone bulk acoustic resonator (HBAR) as a mechanical oscillator for the transduction experiment. The electromechanical interaction between superconducting circuits and HBARs has been extensively studied in the field of circuit quantum acoustodynamics (cQAD), and the preparation of mechanical quantum states of motion has been shown

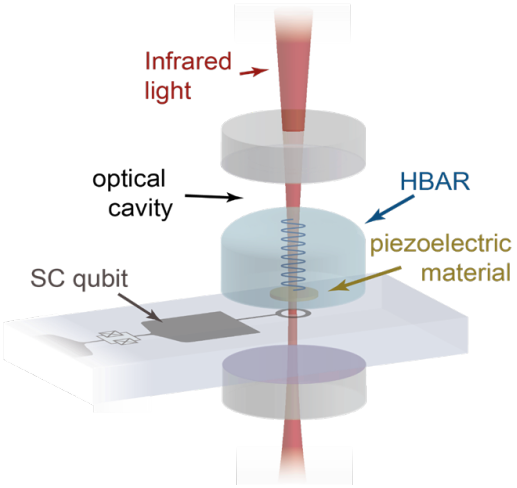

Figure 1.2.: Schematic of our transducer design.

[22, 23]. Optomechanical interaction with HBARs can be achieved by Brillouin scattering of mechanical waves with two modes of an optical Fabry-Pérot cavity [24, 25]. Figure 1.2 shows a schematic of our transducer design. The electric field of a superconducting transmon qubit with a ring antenna couples to mechanical waves in the HBAR made of quartz (α-SiO_2) by means of piezoelectric interaction in a thin aluminum-nitride (AlN) film on the bottom of the HBAR. We will refer to this device as the $\hbar$BAR. The center of the HBAR is aligned with the Gaussian modes of an optical Fabry-Pérot cavity. The transmon's antenna is shaped as a ring around the optical field. Using bulk acoustic waves promotes long mechanical coherence times because the small energy participation ratio at the surface suppresses surface loss. It has also been highlighted that heating of the mechanical modes is very weak in these systems [25]. This is the case even when pumping with high laser power, which can make up for the comparably small single photon coupling. Together with a free space optical cavity with small linewidth, we hope to be able to achieve optomechanical cooperativities on the order of 20. One downside however is the macroscopic size of the device. As we will see in this work, this requires the operation of the transducer with multiple mechanical modes of the HBAR, which poses additional challenges on successfully achieving transduction of single quanta.

This work aims to contribute to achieving microwave to optical transduction of single photons with an HBAR. Chapter 2 introduces the eigenmode structure of HBARs, the mechanism of electro- and optomechanical coupling, as well as a theoretical framework for the multimode nature of the transducer. We will then go on in Chapter 3 to perform simulations on geometry optimization of the transducer. There, we will see how the multimode structure influences the transduction efficiency in different geometries. To better understand theoretically which parameter regimes are optimal for a multimode transducer, we perform calculations and simulations on a toy model with two mechanical modes in Chapter 4. Finally, in Chapter 5 we analyze measurements on electromechanical interactions in the most recent transducer design.

2. Theoretical framework for HBAR transducers

Having introduced qualitatively the working principle of quantum transducers and the components of the HBAR transducer, we will now turn to a mathematical description. Section 2.1 summarizes the relevant aspects of acoustic waves and resonance conditions in HBARs. In Section 2.2, we will look at the mechanisms of electromechanical and optomechanical coupling, and see in Section 2.3 how these ingredients combine to a multimode transducer.

2.1. Mechanical modes of the HBAR

2.1.1. Bulk acoustic waves in quartz

Elastic acoustic waves in solids are governed by Christoffels' equations. For each normalized wave vector, $\vec{q}/\|\vec{q}\|$ ($q = \|\vec{q}\|$), of the acoustic wave, there exist three orthogonal polarization vectors, $\vec{\epsilon}_i$ ($i = 1, 2, 3$), which solve the equations. Each of them is associated with distinct phase velocity v_i. The phase velocities and polarization vectors depend on the material's density, ρ, and stiffness tensor, C_{jk}. The frequency of the wave is related to the wave vector by linear dispersion, $\omega = v_i q$. [26, 27]

For the transduction experiment, we use z-cut quartz (α-SiO_2) as the HBAR material as it is best suitable for the optomechanical interaction (see Subsection 2.2.2). Figure 2.1 shows the three phase velocities in quartz, along the q_x/q_z-plane (left) and q_y/q_z-plane (right) of reciprocal space, which is called the velocity surface. The red branch corresponds to quasi-longitudinally polarized waves, meaning their polarization vector has the smallest angle to the wave vector, out of the three. The two black branches correspond to quasi-transversely polarized waves. In the direction of q_z, the waves are exactly longitudinally (transversely) polarized with phase velocities $v_l = 6.34\,\mathrm{km\,s^{-1}}$ ($v_t = 4.68\,\mathrm{km\,s^{-1}}$). The velocity surfaces were calculated using the *christoffel* python package [27] and material constants from [28].

The transduction experiment will make use of these longitudinally polarized acoustic waves with wave vector in the z-direction. As we will see in Subsection 2.2.2, the optomechanical interaction is only efficient for acoustic waves around the Brillouin frequency $\Omega_B/2\pi = 12.64\,\mathrm{GHz}$. This corresponds to an acoustic wavelength of $\lambda = \frac{2\pi v_l}{\Omega_B} = 0.50\,\mu\mathrm{m}$.

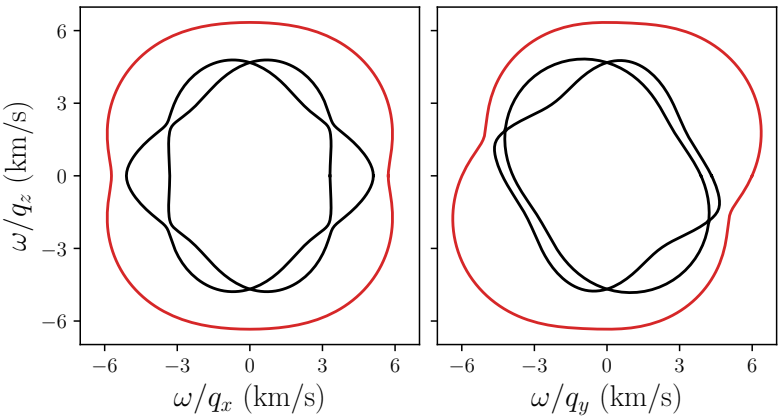

Figure 2.1.: Velocity surface of quartz in the q_x/q_z-plane (left) and q_y/q_z-plane (right). The red branch corresponds to quasi-longitudinally polarized waves and the black branches to quasi-transversely polarized ones. In direction of q_z the waves are exactly longitudinally and transversely polarized. The velocity surfaces were calculated using the *christoffel* python package [27] and material constants from [28].

2.1.2. Resonant bulk acoustic waves

To make use of bulk acoustic waves in a transducer, they need to be confined in a resonator. Figure 2.2 shows the schematic of an HBAR, which works like a Fabry-Pérot cavity for acoustic waves traveling in the z-direction. The bottom of the quartz substrate as well as a dome made of aluminum-nitride (AlN) act as acoustic mirrors. The AlN piece allows coupling to the superconducting qubit through piezoelectric interaction (see Subsection 2.2.1). Its profile $p(x, y)$, called the piezo shape, is much smaller in height ($d_\mathrm{p} = 430\,\mathrm{nm}$) than the thickness of the quartz chip ($L = 1\,\mathrm{mm}$). The transverse extent of the dome is on the order of few $100\,\mu\mathrm{m}$. The piezo shape provides a potential landscape for the acoustic waves that determines the frequencies and displacement fields of a discrete set of resonant acoustic eigenmodes.

Since the piezo shape sets a transverse extent of the mode volume much larger than the acoustic wavelength, diffraction in the HBAR is low [30]. We therefore assume the displacement fields of the eigenmodes to separate into a longitudinal and transverse part as,

$$\vec{u}(x, y, z) = \vec{\epsilon} \cos\left(\frac{l\pi z}{L}\right) u_\eta(x, y), \tag{2.1}$$

where ϵ is the polarization vector, u_η is the transverse mode function, and harmonic time dependence is assumed. We employed a longitudinal resonance condition, $qL = \pi l$ with the longitudinal mode number l, which lets us define the free spectral range (FSR) between successive modes,

$$\mathrm{FSR}_j = \frac{v_j}{2L}, \tag{2.2}$$

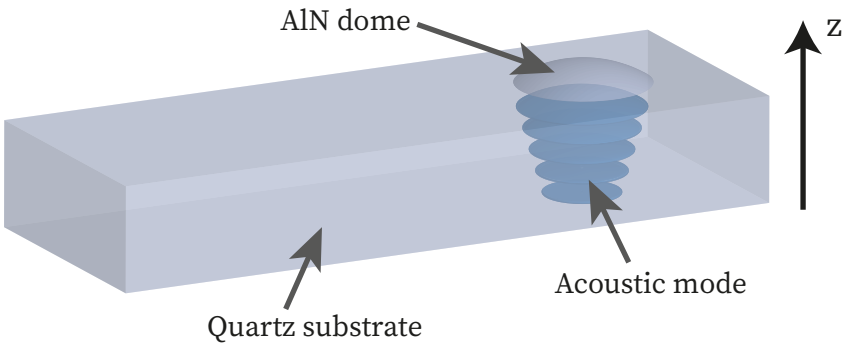

Figure 2.2.: Schematic an HBAR. The piezoelectric AlN dome creates a resonant condition for acoustic waves in the quartz substrate. Image from [29].

where $j = l, t$ for longitudinal and transverse polarization. For the devices in this work, we have $\mathrm{FSR}_l = 3.17\,\mathrm{MHz}$ and $\mathrm{FSR}_t = 2.34\,\mathrm{MHz}$, meaning that the HBAR is operated at mode numbers $l \gtrsim 10^3$.

For the case of longitudinal polarization, we continue to find the transverse mode functions and their resonant frequencies using the acoustic Schrödinger equation (ASE), which describes linear wave propagation in the paraxial approximation [31, 32]. The equation's name comes from the equivalence to a time independent Schrödinger equation,

$$\left[-\frac{1}{2\mu}\left(\frac{\partial^2}{\partial x^2}+\frac{\partial^2}{\partial y^2}\right)+U(x,y)\right]u_\eta(x,y)=\eta u_\eta(x,y), \tag{2.3}$$

with equivalent mass $\mu = \frac{\omega^2}{v_\perp^{\mathrm{eff}}}$, the potential $U(x,y) = -\frac{p(x,y)}{L} - \frac{p^2(x,y)}{2L^2}$, and energy eigenvalues $\eta \ll 1$. The effective transverse velocity $v_\perp^{\mathrm{eff}} = 7.78\,\mathrm{km\,s^{-1}}$ approximates the curvature of the velocity surface in the q_z-direction, and is not to be confused with the velocity of transversely polarized waves v_t. As the velocity surface for transverse polarization does not have a well defined curvature in the q_z-direction (see Figure 2.1), the formalism is not applicable for this polarization.

As in quantum mechanics, the solutions to Equation 2.3 form a discrete set of bound modes with corresponding eigenvalues. For specific piezo shapes, there exist analytical solutions to this problem. Most prominently, the cylinder HBAR's eigenmodes are described by the Bessel functions of the first kind [30], and the spherical cap HBAR, which produces approximately a harmonic potential, supports Hermite-/Laguerre-Gaussian eigenmodes [33]. Throughout this work, we will simulate the transverse mode functions and eigenvalues using DASE, an ASE eigenmode solver (Subsection 3.1.2). The eigenfrequencies associated with the eigenvalues are given by,

$$\omega_k = \omega\frac{1-\eta_0}{1-\eta_k}, \tag{2.4}$$

where ω is the frequency at which the ASE is evaluated, and the integer k enumerates the transverse eigenmodes. The frequency splitting between successive transverse modes

is much smaller than between longitudinal modes, such that the eigenmode spectrum of the HBAR is composed of a series of longitudinal modes, each consisting of a family of transverse modes. For piezo shapes with rotational symmetry, $p(x, y) = p(r)$, where r is the radial coordinate, the transverse mode number k can further be discriminated into a radial mode number m and an angular mode number j (see Subsection 3.1.2). For simplicity, we will use a single mode number n to label the mode's frequency ω_n and displacement field $\vec{u}_n$ throughout this work, unless the specific type of mode number needs to be emphasized.

In the discussion so far, we fully omitted the fact that the HBAR is made of two materials, quartz and AlN, in which acoustic waves travel with different phase velocities. This introduces reflections at the material boundary, which we assume negligible in this model. When solving the ASE, the material boundary is taken into account by rescaling the potential, as will be further elaborated on in Subsection 3.1.2. The thickness of the AlN piece is such that it equals half an acoustic wavelength, $d_\mathrm{p} = p(0, 0) = \lambda/2$. Choosing this piezo thickness maximizes the electromechanical coupling, as we will see in Subsection 2.2.1.

2.1.3. Quantum-mechanical description

Analogously to the quantization of electro-magnetic fields [34], each mechanical eigenmode can be quantized as a quantum harmonic oscillator (HO) with Hamiltonian

$$\hat{H}_n = \hbar\omega_n \hat{b}_n^\dagger \hat{b}_n, \tag{2.5}$$

where $\hat{b}_n$ is the mode's lowering operator. This gives rise to the notion of the phonon, a particle of sound, which is defined as a single excitation of an eigenmode. Throughout this work, we will often refer to the eigenmodes as phonon modes.

The displacement field operators is then,

$$\hat{\vec{u}}_{l,k}(\vec{r}) = u_0 \vec{\epsilon} \cos\left(q_l(z) z\right) f_k(x, y)(\hat{b}_{l,k} + \hat{b}_{l,k}^\dagger), \tag{2.6}$$

in the Schrödinger picture, where u_0 is a normalization constant, $q_l(z)$ is the wave vector for mode l that changes at the material boundary, and f_k are the normalized transverse mode functions. As a means to normalize fields, f, on the transverse plane we will use the $L^2(\mathbb{R}^2)$-norm,

$$\|f\|^2 = \langle f, f \rangle = \int_{\mathbb{R}^2} f^2(x, y)\, \mathrm{d}x\mathrm{d}y, \tag{2.7}$$

which evaluates to unity for the normalized functions f_k.

We will see in the following sections how the mechanical eigenmodes couple to the other quantum degrees of freedom in the hybrid device.

2.2. The hybrid quantum system

In the microwave to optical transducer, the eigenmodes of the HBAR mediate between the two electromagnetic degrees of freedom. Interactions of this type occur if an applied electric field induces mechanical stress, and if in turn mechanical strain changes the electromagnetic environment. The interaction energy is then given by [35, 24],

$$H_{\text{int}} = -\int_V \sum_{j=1}^{6} \sigma_j(\vec{r}) S_j(\vec{r})\, \mathrm{d}V, \tag{2.8}$$

where V is the interaction volume, $\vec{\sigma}(\vec{r})$ is the electrically induced stress, and $\vec{S}(\vec{r})$ is the mechanical strain field.

For longitudinally polarized acoustic waves, only the longitudinal strain $S_3 = S_{zz}$, and the shear strain components $S_4 = S_{zx}$, $S_5 = S_{zy}$ are nonzero. Since the acoustic wavelength is much smaller than amplitude variations in the transverse direction, $S_3 \gg S_4, S_5$ and we can reduce Equation 2.8 to the dominant term,

$$H_{\text{int}} \approx -\int_V \sigma_3(\vec{r}) S_3(\vec{r})\, \mathrm{d}V. \tag{2.9}$$

In the following, we will compute this interaction Hamiltonian in a quantum description and present the key aspects of both the electromechanical and optomechanical couplings.

2.2.1. Electromechanical interaction

Electromechanical interaction between the qubit electric field and the mechanical strain field can be achieved in piezoelectric materials. Piezoelectric interactions occur in non-centrosymmetric materials, and the key signature of this interaction is its linearity, meaning the induced stress is proportional to the applied electric field, $\sigma_j = e_{ji} E_i$, where e is the piezoelectric stress tensor [36]. For AlN we have,

$$e = \begin{bmatrix} 0 & 0 & 0 & 0 & e_{15} & 0 \\ 0 & 0 & 0 & e_{15} & 0 & 0 \\ e_{31} & e_{31} & e_{33} & 0 & 0 & 0 \end{bmatrix}, \tag{2.10}$$

where $e_{33} = 1.55\,\mathrm{C\,m^{-2}}$ [37]. This means that longitudinal stress σ_3, and thus coupling to longitudinally polarized phonons, is induced by the z-component of the qubit electric field. Figure 2.3 shows a sketch of how we achieve piezoelectric interaction in our device. The quartz chip hosting the phonon modes is flip-chip bonded to the chip hosting the qubit such that the AlN film is located above the qubit antenna. We refer to the hybrid device as the $\hbar$BAR.

Quantizing the qubit electric field,

$$\hat{\vec{E}}(\vec{r}) = \vec{E}_0(\vec{r})(\hat{\sigma} + \hat{\sigma}^\dagger), \tag{2.11}$$

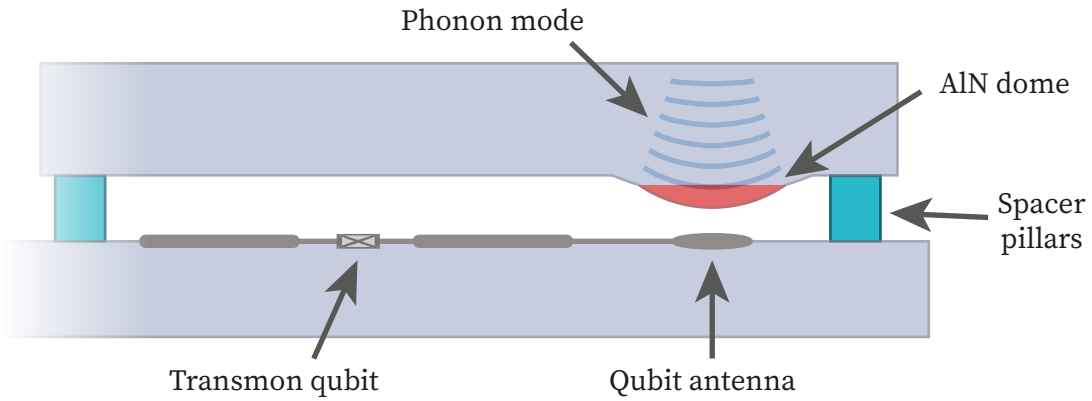

Figure 2.3.: Sketch of an $\hbar$BAR. The bottom chip made of sapphire hosts a transmon qubit. The HBAR chip made of quartz is flip-chip bonded to the bottom chip with spacer pillars as a separation. The bonding is such that the AlN film is located above the qubit antenna for strong piezoelectric interaction. Image from [29].

where $\vec{E}_0(\vec{r})$ is the single photon qubit mode function, and $\hat{\sigma}$ is the qubit lowering operator, employing a rotating wave approximation (RWA) and equating Equation 2.9 to the Jaynes-Cummings-Hamiltonian,

$$\hat{H}_{\mathrm{JC}} = \sum_n \hbar g_{\mathrm{e},n} (\hat{\sigma}^\dagger \hat{b}_n + \hat{\sigma} \hat{b}_n^\dagger), \tag{2.12}$$

we can find the electromechanical coupling strength $g_{\mathrm{e},n}$ between the qubit and a mechanical mode n. Including the normalization of the strain field which respects the AlN quartz boundary, we arrive at the expression [38],

$$g_{\mathrm{e},n} = \frac{e_{33} v_l^{\mathrm{p}}}{\sqrt{\hbar \omega_n \left(C_{33}^{\mathrm{p}} d_{\mathrm{p}} + C_{33}^{\mathrm{q}} L\right)}} \left(1 - \cos\left(\frac{\omega_n}{v_l^{\mathrm{p}}} d_{\mathrm{p}}\right)\right) \int_{A_{\mathrm{p}}} E_z(x,y) f_n(x,y)\, \mathrm{d}x\mathrm{d}y, \tag{2.13}$$

where $v_l^{\mathrm{p}} = 10.9\,\mathrm{km\,s^{-1}}$ is the phase velocity of longitudinally polarized phonons in AlN, C_{33}^{p} and C_{33}^{q} are the stiffness tensor components for AlN and quartz (values from [28]), and E_z is the z-component of $\vec{E}_0$. The center term in parenthesis results from integrating the z-axis. It is maximized if the piezo thickness, d_{p}, respects $\frac{\omega_n}{v_l^{\mathrm{p}}} d_{\mathrm{p}} = \pi$, i.e. if $d_{\mathrm{p}} = \lambda_{\mathrm{p}}/2$ with λ_p the acoustic wavelength in AlN. For $\omega_n = \Omega_B$, this is the case for $d_p = 430\,\mathrm{nm}$, which is the value aimed for in fabrication of transduction HBARs. The prefactors are due to the integration and normalization of the strain field. The last term is the overlap integral between the qubit electric field and the transverse strain profile. The electric field is assumed to be constant over the piezo thickness.

The electromechanical coupling strengths are the key parameters of the piezoelectric interaction, and we will perform measurements which aim at deriving values for these quantities in Chapter 5. As a comparison, we will evaluate Equation 2.13 with simulations of the electric field in Ansys (see Subsection 3.1.1) and the strain field in DASE

(see Subsection 3.1.2), and find poor agreement. For the simulations in Chapter 3, we will therefore evaluate only the normalized overlaps,

$$\mathfrak{g}_{\mathrm{e},n} = \int_{A_\mathrm{p}} \mathfrak{E}_q(x,y) f_n(x,y)\,\mathrm{d}x\mathrm{d}y, \tag{2.14}$$

and assume an overall scaling factor based on measurements to get the values for $g_{\mathrm{e},n}$. $\mathfrak{E}_q$ is the normalized qubit electric field using the norm defined in Equation 2.7.

For the transduction experiment it is necessary to turn on and off the piezoelectric interaction. This is achieved by rapidly tuning the qubit frequency in or out of resonance with the mechanical modes, by applying an off-resonant drive with frequency ω_d and strength ξ_d to the qubit. The drive induces a frequency shift, the so called Stark shift, $\delta_{\mathrm{Stark}} = \frac{\alpha\xi_d^2}{2\Delta_d(\Delta_d+\alpha)}$, where $\Delta_d = \omega_q - \omega_d$ is the drive detuning and $\alpha < 0$ is the transmon's anharmonicity [39].

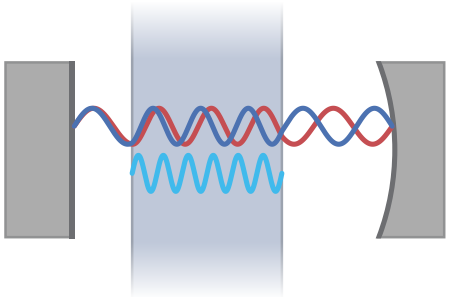

Figure 2.4.: Sketch of the modes participating in the optomechanical interaction. The red and blue waves represent adjacent longitudinal modes of the optical cavity. The cyan wave is a mechanical eigenmode of the substrate. Image from [29].

2.2.2. Optomechanical interaction

In contrast to the electromechanical interaction, the optomechanical interaction is nonlinear involving two modes of an optical Fabry-Pérot cavity as well as the mechanical mode. Figure 2.4 shows a sketch of the system where the two optical modes are displayed as red/blue standing waves and the mechanical mode as a cyan standing wave. The interaction between these modes is a Brillouin optomechanical process, where the beatnote of the two optical modes can excite mechanical oscillation through the time modulated electrostrictive force that electric fields exert on dielectrics. In turn, mechanical oscillations modulate the refractive index of the material, effectively forming a Bragg grating, at which optical waves can scatter.

The Brillouin interaction requires the frequency as well as the wavelength of the optical beatnote to match the mechanical oscillation, which we call the phase matching

condition,

$$\omega_n = \omega_2 - \omega_1, \tag{2.15}$$

$$q_n = k_2 + k_1, \tag{2.16}$$

where ω_1 (k_1) and ω_2 (k_2) are the frequency (wavevector) of adjacent optical modes of the resonator. When using optical modes at $\sim 1550\,\mathrm{nm}$ and quartz as the dielectric, the phase matching condition is fulfilled at $\omega_n = 12.65\,\mathrm{GHz} = \Omega_B$, which we call the Brillouin frequency. It is desirable to have this frequency as low as possible, to still be able to properly operate the superconducting circuitry. This is the reason for choosing quartz as the HBAR material, where Ω_B is relatively low compared to other popular dielectrics like sapphire and silicon.

Fabry-Pérot resonators usually have a uniform spectrum with a well defined FSR, which would make it hard to select two unique optical modes to participate in the interaction. Fortunately, this problem is naturally solved by placing the HBAR inside the cavity. This introduces optical reflections at the material boundaries which make the spectrum nonuniform and allows to choose two optical mode with a separation of Ω_B.

Comparison of Equation 2.9 to the three particle interaction Hamiltonian,

$$\hat{H}_3 = -\sum_n \hbar g_{0,n} \left(\hat{a}_2^\dagger \hat{a}_1 \hat{b}_n + \hat{a}_2 \hat{a}_1^\dagger \hat{b}_n^\dagger \right), \tag{2.17}$$

yields the single photon optomechanical coupling strength $g_{0,n}$, where $\hat{a}_1$ and $\hat{a}_2$ are the lowering operators of the two optical modes. We included multiple mechanical modes into the Hamiltonian as the linewidth of the optical modes is usually large enough to support multiple transverse modes of the HBAR. Assuming linearly polarized electric fields, we can express the coupling strength as

$$g_{0,n} \propto \int_{V_\mathrm{q}} E_1(\vec{r}) E_2(\vec{r}) S_n(\vec{r})\,\mathrm{d}V \propto \int_{A_\mathrm{p}} \mathfrak{E}_\mathrm{o}^2(x,y) f_n(x,y)\,\mathrm{d}x\mathrm{d}y = \mathfrak{g}_{\mathrm{o},n}, \tag{2.18}$$

where V_q is the HBAR volume, and E_1, E_2, S_n are the electric or strain fields of the optical and mechanical modes. Writing the first proportionality, we omitted normalization factors, permittivities and photoelastic constants. In the second proportionality, z-integration was performed, we normalized the laser electric fields using Equation 2.7, and we assumed equal shapes, $\mathfrak{E}_\mathrm{o}$, for both optical modes. We will refer to this second integral as the normalized overlap $\mathfrak{g}_{\mathrm{o},n}$.

Note that the overlap integral contains two electric field modes, which is due to the fact that the electrostrictively induced stress does not linearly depend on the applied electric field in contrast to piezo electrically induced stress. In optomechanical experiments of this kind, values of $g_{0,n} \sim 2\pi \cdot 10\,\mathrm{Hz}$ were achieved [24, 25]. For the transduction experiment, coherent swapping from the mechanics to the optics is desired, which requires much larger coupling rates and a beam splitter type interaction. This can be achieved by strongly pumping the lower frequency optical mode with a laser, resulting

in the Hamiltonian,

$$\hat{H}_{\text{pump}} = -\sqrt{\bar{n}_1} \sum_n \hbar g_{0,n} \left(\hat{a}^\dagger \hat{b}_n + \hat{a} \hat{b}_n^\dagger \right), \tag{2.19}$$

where $\bar{n}_1$ is the average intracavity photon number of mode 1, and we omit the subscript on mode 2 from now on. We can now define the cavity enhanced optomechanical coupling as $g_{\text{o},n} = g_{0,n}\sqrt{\bar{n}_1}$, which lets us effectively tune the optomechanical interaction strength, based on the applied pump power.

For the simulations (Chapter 3), we will calculate the overlap in Equation 2.18 and have the scaling factor subject to optimization.

2.3. Multimode transduction

The goal of the transduction experiment is to coherently transfer single microwave photons from a transmon qubit to the optical regime, with mechanical modes in the HBAR as an intermediary. We saw in the last section how we achieve tunable linear coupling between the modes of the HBAR and the electromagnetic degrees of freedom. Let us now turn our attention to the implications on the geometry of the device.

Linear coupling is achieved by spatial overlap between the electric and strain fields. To optimize coupling, the modes of the HBAR should thus have large overlap with both the qubit electric field, which is localized near the qubit antenna, and the laser field, which has a Gaussian shape. Meanwhile, the laser field must not overlap with the qubit antenna, since reflections off the qubit metal drastically limit the optical quality factor. This sets requirements on the transverse extend of the mechanical modes, because the qubit ring antenna has to have a certain diameter in order to not clip the laser beam.

As it will turn out in simulations (see Section 3.3), the transverse eigenmodes of the HBAR, which we labeled with k, have frequency splittings which are smaller than the bandwidth of the transducer, set by the coupling rates and the optical linewidth κ_{o}. There are now two possibilities to design the transducer. In a design aiming for transduction with a single mechanical mode, the bandwidth needs to be smaller than the mode spacing, which can be achieved by intentionally reducing the electromechanical coupling. This would result in an overall decrease in the figures of merit characterizing the performance of the transducer. The bandwidth would be lower by design, the efficiency would decrease, due to a decrease in electromechanical cooperativity, and noise would be added from thermal population of unused mechanical modes within the optical linewidth. Instead, we aim for a multimode transducer, which we describe in the following.

2.3.1. Electric and optical bright states

The interaction of the transmon qubit with the transverse eigenmodes of the HBAR, and the subsequent interaction with the optical cavity are describe by the electromechanical

(EM) and optomechanical (OM) Hamiltonians. They can be written as,

$$\hat{H}_{\mathrm{EM}}/\hbar = \omega_q \hat{\sigma}^\dagger \hat{\sigma} + \sum_k \left(\omega_k \hat{b}_k^\dagger \hat{b}_k + g_{\mathrm{e},k} \left(\hat{b}_k \hat{\sigma}^\dagger + \hat{b}_k^\dagger \hat{\sigma} \right) \right) \tag{2.20}$$

$$= \omega_q \hat{\sigma}^\dagger \hat{\sigma} + \sum_k \omega_k \hat{b}_k^\dagger \hat{b}_k + g_{\mathrm{e,tot}} \left(\hat{b}_{\mathrm{e}} \hat{\sigma}^\dagger + \hat{b}_{\mathrm{e}}^\dagger \hat{\sigma} \right), \tag{2.21}$$

$$\hat{H}_{\mathrm{OM}}/\hbar = \Delta_{12} \hat{a}^\dagger \hat{a} + \sum_k \left(\omega_k \hat{b}_k^\dagger \hat{b}_k + g_{\mathrm{o},k} \left(\hat{b}_k \hat{a}^\dagger + \hat{b}_k^\dagger \hat{a} \right) \right) \tag{2.22}$$

$$= \Delta_{12} \hat{a}^\dagger \hat{a} + \sum_k \omega_k \hat{b}_k^\dagger \hat{b}_k + g_{\mathrm{o,tot}} \left(\hat{b}_{\mathrm{o}} \hat{a}^\dagger + \hat{b}_{\mathrm{o}}^\dagger \hat{a} \right), \tag{2.23}$$

where ω_q is the qubit resonance frequency, Δ_{12} is the detuning between the two optical modes, and $g_{j,\mathrm{tot}} = \sqrt{\sum_k g_{j,k}^2}$ is the total EM (OM) coupling with $j = \mathrm{e}$ (o). In Equation 2.20 and 2.22, we wrote down the interaction derived in the previous section together with the bare evolution, and in Equation 2.21 and 2.23 we introduced the lowering operator $\hat{b}_{\mathrm{e}}$ ($\hat{b}_{\mathrm{o}}$) for the electric (optical) bright state. These operators act on the vacuum, $|0\rangle$, as follows,

$$|B_j\rangle = \hat{b}_j^\dagger |0\rangle = \frac{1}{g_{j,\mathrm{tot}}} \left(\sum_k g_{j,k} |1_k\rangle \right), \tag{2.24}$$

where $|1_k\rangle$ is the single phonon state of mode k with all other modes in the vacuum. This means that EM (OM) coupling only occurs for a certain superposition of mechanical states called the bright states.

It turns out that the electric and optical bright states are approximately orthogonal,

$$\langle B_{\mathrm{e}} | B_{\mathrm{o}} \rangle \propto \sum_{k,k'} \mathfrak{g}_{\mathrm{e},k} \mathfrak{g}_{\mathrm{o},k'} \langle 1_k | 1_{k'} \rangle \tag{2.25}$$

$$= \sum_k \int_{A_{\mathrm{p}}} \mathfrak{E}_q(x,y) f_k(x,y) \,\mathrm{d}x\mathrm{d}y \int_{A_{\mathrm{p}}} f_k(x',y') \mathfrak{E}_{\mathrm{o}}^2(x',y') \,\mathrm{d}x'\mathrm{d}y' \tag{2.26}$$

$$= \sum_k \langle \mathfrak{E}_q, f_k \rangle \langle f_k, \mathfrak{E}_{\mathrm{o}}^2 \rangle \approx \langle E_z, E_{\mathrm{o}}^2 \rangle \tag{2.27}$$

$$= \int_{\mathbb{R}^2} \mathfrak{E}_q(x,y) \mathfrak{E}_{\mathrm{o}}^2(x,y) \,\mathrm{d}x\mathrm{d}y = 0. \tag{2.28}$$

In Equation 2.27 we used that the functions f_k are solutions to the ASE, a Schrödinger equation, and thus form an orthogonal basis on the Hilbert space $L^2(\mathbb{R}^2)$ with the inner product $\langle \cdot, \cdot \rangle$ defined in Equation 2.7. This is only approximately true though, as the potentials in Equation 2.3 only have a finite depth, and thus only feature a finite number of bound modes, of which only six will be considered in the simulations (see Section 3.3). The overlap integral in Equation 2.28 is zero, because the qubit and laser electric fields must not overlap, as we established.

While at first this seems like it would make transduction impossible, we have to keep in mind that the electric bright state is not an eigenstate of the HBAR. This

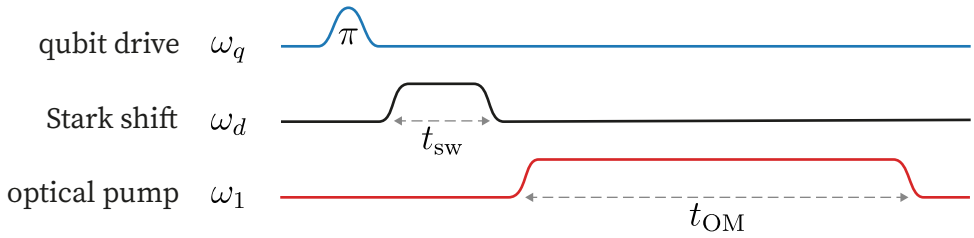

Figure 2.5.: Pulse sequence for transduction of a single photon. t_{sw} is the EM swap time, and t_{OM} is the pulse duration of the pump laser.

means that it evolves in time such that the resulting mechanical state is no longer orthogonal to the optical bright state. This rephasing of mechanical states is the key aspect that distinguishes a multimode transducer from a single mode transducer. We will investigate in Section 3.3 how the geometry of HBARs influences the rephasing properties of mechanical states and thus the transduction efficiency.

2.3.2. The transduction sequence

Figure 2.5 shows the sequence of pulses for transducing a single photon from the microwave to the optical domain. The qubit is driven to its excited state and then Stark shifted into resonance with a family of transverse eigenmodes of the HBAR. It coherently transfers its excitation to the electric bright state, which simultaneously starts to rephase into a state closer to the optical bright state. The optical pump is applied to drive the OM interaction, which swaps population from the optical bright state to the optical cavity. Two single photon detectors (SPDs) then record the leakage of the photon out of the cavity in an HBT interferometer [40].

Out of the multiple figures of merit for quantum transducers, we will only be interested in the transduction efficiency η_t throughout this work, as it can be substantially lowered by being in the multimode regime. It quantifies the average number of transduced optical photons per microwave photon. While experimentally, state preparation and measurement (SPAM) errors play a big role and limiting this efficiency [18, 20], we will only be focusing on factors introducing loss during the transduction sequence itself. These factors include imperfect rephasing of the electric into the optical bright state, qubit relaxation at rate γ, and phonon relaxation of mode n at rate Γ_n. Qubit dephasing γ_ϕ, will not be considered in the simulations, although we will see that it can play an important role in the experiment (Chapter 5). Furthermore we will assume, that the optical cavity only has external losses at rate κ_{o}, such that all photons leaking the cavity can be detected. Throughout this work, we will consider a simple Markovian noise model, such that all decoherences occur as an exponential decay. The transduction efficiency is calculated as,

$$\eta_t(t) = \kappa_{\mathrm{o}} \int_0^t \langle a^\dagger a \rangle(t')\, \mathrm{d}t', \tag{2.29}$$

where t is the optomechanical interaction time.

A useful figure of merit to characterize mechanical states is their fidelity with respect to the electric and optical bright states. It is defined as [41],

$$\mathcal{F}_j(\rho) = \left(\mathrm{Tr}\sqrt{\sqrt{\rho}|B_j\rangle\langle B_j|\sqrt{\rho}}\right)^2, \tag{2.30}$$

where $j = \mathrm{e}, \mathrm{o}$, and ρ is the density matrix of the mechanical state. If ρ is a pure state, the fidelity is equal to the population of ρ in the respective bright state.

3. Simulations on geometry optimization of HBAR transducers

With a theoretical framework at hand, we will now optimize aspects of the transducer geometry in terms of transduction efficiency. The components of the device are a Gaussian optical mode surrounded by a ring qubit antenna, both coupling to a rotationally symmetric HBAR, much like in Figure 1.2. Since the Gaussian shape of the optical mode is set by the optical cavity, which has been carefully designed by the team already, we will focus on optimizing the piezo profile as well as the qubit ring antenna. The piezo profile has two geometry parameters, a cutoff radius r_{cut}, as well as a shape. The shapes we will look at are the cylinder, the spherical cap dome, as well as the p-norm dome, which is a middle ground between the two. The qubit antenna has an inner, r_{in}, and an outer radius, r_{out}. The first of which is not subject to optimization as the optical mode waist, $w_{\mathrm{o}} = 60\,\mu\mathrm{m}$, sets a minimum value for the inner antenna radius. It has been determined to be $r_{\mathrm{in}} = 200\,\mu\mathrm{m}$ through measurements of the optical quality factor for different antenna positions by the transduction team.

The device with a cylinder piezo shape has previously been optimized to $r_{\mathrm{out}} = 253\,\mu\mathrm{m}$ and $r_{\mathrm{cut}} = 266\,\mu\mathrm{m}$. This optimization used a very simplified assumption about the qubit electric field, which we will improve on in Section 3.2. Through electromechanical measurements of devices of this design (see Chapter 5) we were also able to get more realistic values of the electromechanical coupling. These improvements let us redo the optimization of the cylinder HBAR, and additionally optimize other piezo shapes in Section 3.3. The simulation methods used for this are presented in Section 3.1.

3.1. Simulation methods

3.1.1. Ansys HFSS

In order to evaluate the electromechanical coupling rates (Equation 2.13), we use Ansys HFSS to simulate the qubit electric field. Ansys HFSS is a 3D electromagnetic simulation software for designing and simulating high-frequency electronic products [42]. It uses the finite element method (FEM) to solve Maxwells' equations on a nontrivial geometry. Many iterations of simulation and experiments by the transduction team went into designing the coupled system of qubit and readout resonator (see Subsection 5.2.1) with this software. Here, we use it to simulate the electric field of the qubit eigenmode for different antenna geometries.

Figure 3.1 shows the 3D model of the transduction $\hbar$BAR in the geometry of previous optimization inside a tunnel cavity (gray). The qubit chip (blue) hosts the transmon

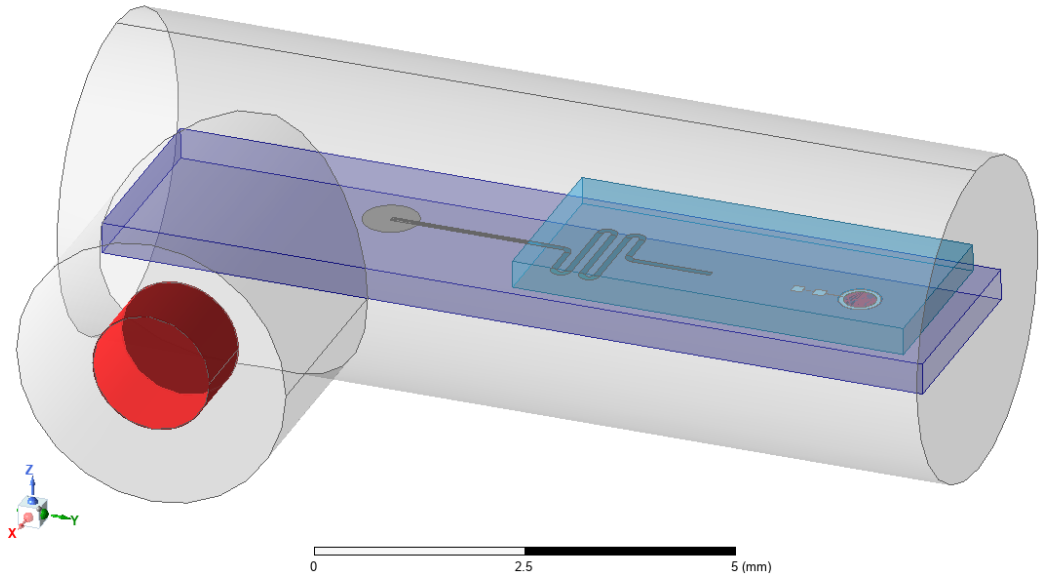

Figure 3.1.: Model of the $\hbar$BAR for transduction in Ansys HFSS. Red: Microwave input/output pin. Gray: Tunnel cavity. Blue: Qubit chip with readout resonator and qubit with ring antenna on top. Cyan: HBAR with AlN film (red) on its bottom.

qubit with the ring antenna, as well as a stripline readout resonator. The top chip is the HBAR (cyan), which host the AlN film (red) on its bottom side above the qubit antenna. The metal components are modeled as 2D perfect conductors, and the chips and the AlN are modeled as dielectrics. In the software, the qubit is simulated as a harmonic resonator with geometric capacitance, and lumped element inductance L_J and capacitance C_J at the Josephson junction. The nonlinear parameters of the coupled qubit-resonator system can be evaluated with the EPR-method [43], from the linear HFSS simulation solutions. The resolution of the electric field solutions, depends on the initial mesh settings. Setting a finer mesh requires significantly more simulation time, which is why we will use different mesh settings for different applications in this work.

To evaluate Equation 2.13, we will export the z-component of the simulated electric field, E_z^{sim}, above the qubit antenna inside the AlN film. To normalize the field to one photon, we extract the energy ϵ_{mode} of the qubit mode from the simulation and rescale the electric field to,

$$E_z = \frac{1}{2}\sqrt{\frac{\hbar\omega}{\epsilon_{\text{mode}}}}E_z^{\text{sim}}, \tag{3.1}$$

where ω is the frequency at which the resonant EM-interaction is simulated, which is usually the Brillouin frequency Ω_B.

3.1.2. DASE

DASE is an acronym for Dimensionally reduced Acoustic Scrödinger Equation. The dimensional reduction of Equation 2.3 uses the rotational symmetry of the piezo profile $p(r)$, which lets us do a separation Ansatz $u_\eta(r) = u_r(r)u_\phi(\phi)$. Since the ASE only depends on the radial coordinate in this case, we get the trivial solutions $u_\phi^j(\phi) = e^{i\phi j}$ for the angular coordinate, where the integer j can be identified with the phonon angular momentum. The radial part is now governed by a dimensionally reduced ASE whose solutions, $u_r^{m,j}(r)$, can be labeled with a radial mode number m and the angular mode number j. It turns out that only the modes with $j = 0$ respect rotational symmetry. The electromechanical coupling is thus dominated by these modes since the qubit electric field is designed to also respect this symmetry. We will therefore only consider these symmetric modes throughout this work, which we notate as $f_m(r)$ and normalize using Equation 2.7.

DASE is implemented as a python library for numerical diagonalization of the dimensionally reduced Hamiltonian. The parameters of the simulation are the frequency, ω, the wave velocities, v_l and $v_\perp^{\text{eff}}$, of longitudinally polarized phonons in quartz, as well as the HBAR thickness, L, and the piezo profile, $p(r)$. It is important to consider the AlN quartz material boundary in the simulation due to the different speeds of sound in the piezo film, v_l^{p}, and the quartz substrate, v_l. We do so by rescaling the piezo shape, $p_{\text{scale}}(x, y) = \frac{v_l}{v_l^{\text{p}}} p(x, y)$, such that the rescaled profile (assumed to be made of quartz) provides the same boundary conditions as the physical one. The software returns the normalized mode functions $f_m(r)$ as well as their eigenvalues η_m, from which we calculate the mode frequencies using Equation 2.4.

The advantage of DASE over other methods to find the HBAR eigenmodes, based on beam propagating for example, is its speed. DASE is very fast because it only has to compute numerical diagonalizations of matrices. Its disadvantage is that loss rates of the eigenmodes cannot reliably be determined. For more information on the DASE we refer to reference [31].

In Section 4.4 we will simulate the eigenmodes of piezo shapes in a double-well geometry, i.e. without rotational symmetry. The ASE has to be solved in two dimensions now which we do with a modified version of DASE, 2D-DASE.

3.1.3. Simulation of the transduction efficiency

We simulate the transduction sequence, by solving the time dynamics of the EM and OM Hamiltonians ((see Equation 2.20 and 2.22) using QuTiP's master equation solver *mesolve*. As initial state, $|\psi_0\rangle = |1_q\rangle \otimes_m |0_m\rangle \otimes |0_{\text{o}}\rangle$, we have the qubit being in the excited state and all other oscillators in the ground state, neglecting thermal population. All oscillators are modeled as two level system, because the total population of the system can never exceed one excitation if heating due to the thermal environment is neglected. We assume Markovian relaxation of all oscillators at rates $\gamma = 1/(10\,\mu\text{s})$ for the qubit, $\Gamma_m = 1/(50\,\mu\text{s})$ for all mechanical modes, and $\kappa_{\text{o}} = 2\pi \cdot 1\,\text{MHz}$ for the optical cavity. The transduction team aims to achieve values of this order for the transduction experiment.

The parameters of the Hamiltonians are the resonance frequencies of all oscillators, ω_q, ω_m and Δ_{12}, as well as the electromechanical and optomechanical coupling rates $g_{\mathrm{e},m}$ and $g_{\mathrm{o},m}$. For a given geometry, $N_{\mathrm{mech}} = 6$ mechanical mode functions $f_m(r)$ and frequencies ω_m are simulated using DASE. The EM (OM) couplings are then obtained by calculating the EM (OM) forcing overlaps $\mathfrak{g}_{\mathrm{e},n}$ ($\mathfrak{g}_{\mathrm{o},n}$) using Equation 2.14 (Equation 2.18) and scaling them by the total coupling $g_{\mathrm{e,tot}}$ ($g_{\mathrm{o,tot}}$). In Section 5.6 we will estimate $g_{\mathrm{e,tot}} = 2\pi \cdot 75\,\mathrm{kHz}$, and $g_{\mathrm{o,tot}}$ will be subject to optimization as we can control it with the pump laser power. To calculate the forcing overlaps, we simulate the qubit electric field, $\mathfrak{E}_q$, in Section 3.2, and use a Gaussian shape with optical mode waist $w_{\mathrm{o}} = 60\,\mu\mathrm{m}$ for the laser field $\mathfrak{E}_{\mathrm{o}}$. This value was extracted from knife edge measurements of the physical optical cavity. We will refer to these fields as the electric and optical forcing fields. The qubit frequency ω_q and optical mode pair detuning Δ_{12} are put on resonance with the most strongly coupled mechanical modes.

The simulation is performed in two steps. At first, the EM Hamiltonian is simulated giving rise to vacuum Rabi oscillations between the qubit and the mechanical modes. We define the first minimum in qubit population as the swap time, t_{sw}, and use the mechanical state at this time as the initial state for the second step, the OM interaction. The simulation of the OM interaction yields the optical cavity population as a function of time, from which we finally calculate the transduction efficiency with Equation 2.29. As the figure of merit for geometry optimization (see Section 3.3), we evaluate the transduction efficiency at the time $t_{\mathrm{OM}} = 25\,\mu\mathrm{s}$. It is possible to include a wait time of free evolution, t_{wait}, between the two steps, which allows the mechanical state to increase its fidelity with respect to the optical bright state. We will investigate if it is advantageous to include a wait time in the context of the two mode toy model in Chapter 4. For the simulations in Section 3.3, we will have $t_{\mathrm{wait}} = 0$.

3.2. Parametrization of the electric forcing field

In the previous state of optimization of the cylinder HBAR, the electric forcing field was assumed as a simple door function, which is constant above the qubit antenna and zero elsewhere. A more realistic estimate of the qubit electric field can be provided with Ansys simulations of the system. The left panel of Figure 3.2 compares the simple door forcing function with two versions of electric fields from Ansys simulations with coarse and fine mesh settings for the previously optimized geometry. The one-dimensional representations of the electric field were obtained by averaging over the angle coordinate as described in Subsection 3.2.1. The two versions of fields slightly deviate, and the fine mesh seems to produce sharper features. Throughout this section, we will use the $L^2(\mathbb{R})$-norm,

$$\|E\|^2 = \langle E, E\rangle = \int_I E^2(x)\,\mathrm{d}x, \tag{3.2}$$

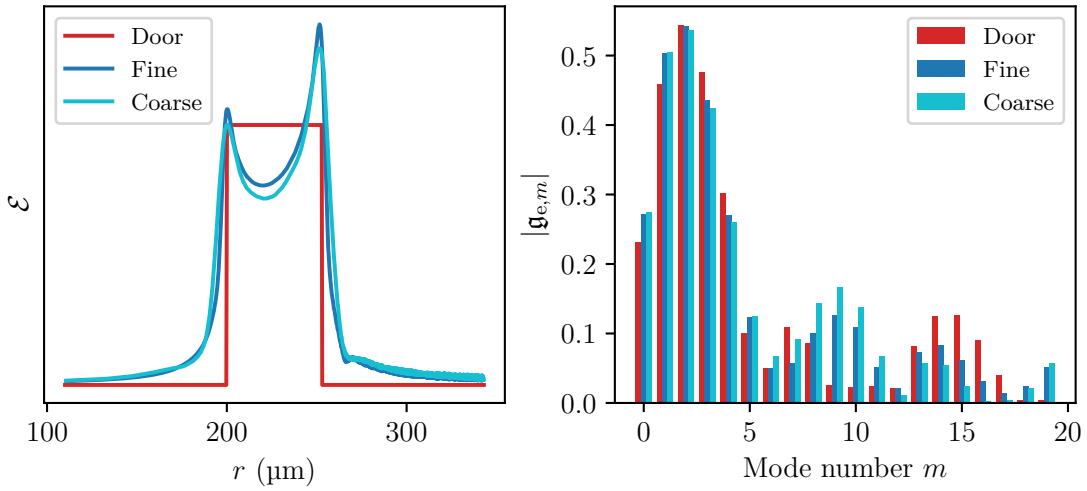

Figure 3.2.: Left: Simple assumption (door), and simulated electric fields (fine and coarse mesh) for the qubit antenna geometry resulting from previous optimization. Right: Resulting electromechanical forcing overlaps (see Equation 3.4).

to normalize the one-dimensional representations of electric field simulations E on an interval I, and measure the distance d between normalized fields $\mathcal{E}_1$ and $\mathcal{E}_2$ as,

$$d^2 = \|\mathcal{E}_1 - \mathcal{E}_2\|^2 = \int_I (\mathcal{E}_1(x) - \mathcal{E}_1(x))^2 \, \mathrm{d}x. \tag{3.3}$$

Assuming that the simulation with fine mesh, is closest to the true electric field, we can calculate its distances $d_{\text{coarse}} = 0.135$ to the simulation with coarse meshing, and $d_{\text{simple}} = 0.424$ to the simple door forcing.

The right panel of Figure 3.2 shows the overlaps (see Equation 2.13) of the three forcing fields with the eigenmodes of the cylinder HBAR in the previous state of optimization. We can observe that all fields mostly follow the same trend up to mode numbers of six, where significant deviations between the simulated and simple fields arise. In the first six modes, there are notable differences in overlaps except for mode number two. Although the deviations between simple and simulated fields may look insignificant here, they might still cause the optimal geometry to be different from the previous optimization.

Having to simulate the electric forcing fields in Ansys for every geometry of the optimization process is not feasable, since the simulation takes $\sim 10\,\text{min}$ with the coarse, and $\sim 4\,\text{h}$ with the fine mesh settings. Instead, the goal of this section is to simulate training and test data sets with the coarse mesh settings that let us train and benchmark a model to predict the electric forcing field for arbitrary antenna geometries. With this model, we will then be able to rerun the geometry optimizations with a better estimate of the electric forcing field.

3.2.1. Collecting and preprocessing data

To create training and test data sets, we perform Ansys simulations of the qubit-resonator system (see Figure 3.1) and vary the inner and outer antenna radii, while keeping the rest of the design identical. For each geometry, we extract the E_z component right below the piezo cylinder, instead of inside it. The reason for this, is that especially with the coarse mesh settings, the electric field inside the piezo becomes quite noisy in the simulation. Physically, the z-component of electric fields right before and after the boundary between dielectrics, should only differ in magnitude, which is not important here, since we will normalize the fields anyway.

For the training set, we simulate 110 geometries in total, varying the inner radius from 100 µm to 200 µm, and the antenna thickness $T = r_{\text{out}} - r_{\text{in}}$ from 10 µm to 100 µm, both in steps of 10 µm. The test set includes 99 geometries with the same inner radii, and thicknesses from 19 µm to 91 µm in steps of 9 µm. Before training the model, we preprocess the electric field data in two steps.

Averaging over the angle coordinate

The transduction device is designed around mechanical modes with rotational symmetry. The electromechanical overlaps (see Equation 2.14) for these modes compute to,

$$\mathfrak{g}_{\text{e},m} = \int_{A_p} \mathfrak{E}_q(r,\phi) f_m(r) r \, \mathrm{d}r\mathrm{d}\phi = 2\pi \int_0^{r_{\text{cut}}} \bar{\mathfrak{E}}_q(r) f_m(r) r \, \mathrm{d}r, \tag{3.4}$$

where $\bar{\mathfrak{E}}_q(r)$ is the qubit electric field, averaged over the angle coordinate. Asymmetric components in the electric field, e.g. due to the antenna lead, can thus only couple to asymmetric mechanical modes. These modes could be relevant especially if $r_{\text{cut}} \gg r_{\text{out}}$ such that the AlN film covers large parts of the antenna lead. The relevance of asymmetry in such geometries could be worth exploring in the future.

Performing the average over the angle coordinate is implemented in the following way. First, we define a array of radii on the interval $I = (r_{\text{in}} - 90\,\mu\text{m}, r_{\text{out}} + 90\,\mu\text{m})$ with 700 elements. Then, for each radius of the array, we compute the average electric field of all points, whose radial coordinate is closest to that radius. The radii in the grid are spaced, so that each average is computed over the same number of data points. The resulting data are one-dimensional arrays of electric fields, which we normalize using Equation 3.2, $\mathcal{E}$, defined on an interval I for each geometry.

Averaging over variations of the inner radius

Looking at geometries with the same thickness and varying inner radii, we notice that the normalized electric fields look very similar. The left panel of Figure 3.3 shows the electric field data of geometries with $T = 50\,\mu\text{m}$, where the intervals I have been shifted to have the inner radius values be zero. The mean field is plotted as the red dashed line. To quantify the error of taking the mean, we compute the average distance of the data to the mean. Doing so for all geometries, we get $\bar{d}^{\text{train}}_{\text{inner}} = 0.034 \pm 0.016$ for the training

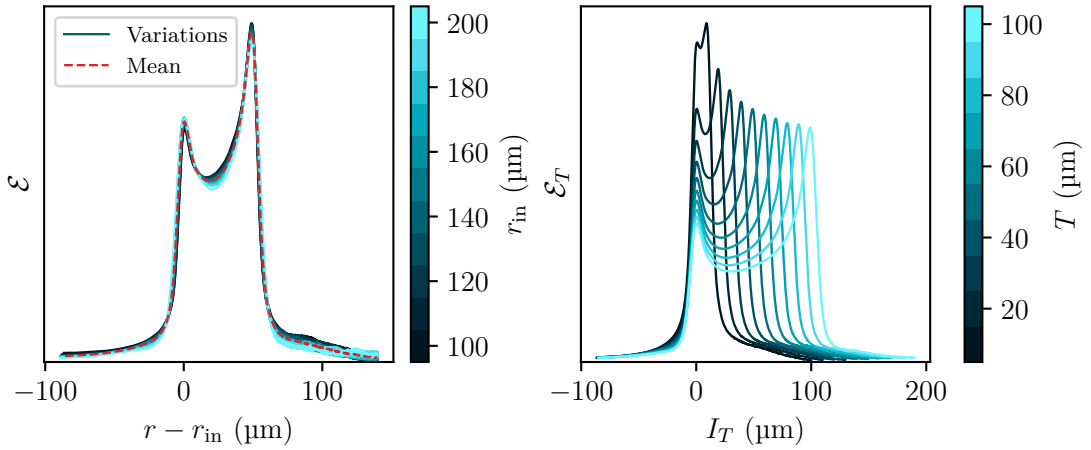

Figure 3.3.: Left: electric field data for geometry variations with antenna thickness $T = 50\,\mu\text{m}$ (colored solid lines), and their mean (red dashed line). Right: full training data set, resulting from both preprocessing steps.

set, and $\bar{d}^{\text{test}}_{\text{inner}} = 0.033 \pm 0.016$ for the test set, where the errors specify the standard deviations. These distances are much smaller than the distance between coarse and fine mesh solutions, which justifies taking the mean here.

The right panel of Figure 3.3 shows the full training data set after the preprocessing steps, consisting of ten electric field arrays $\mathcal{E}_T$ defined on intervals I_T for different qubit antenna thicknesses T. The same applies for the training set, which includes nine antenna thicknesses.

3.2.2. Training a model for electric field prediction

With the training data, we now want to train a model that lets us quickly predict an electric field array for any antenna thickness $T \in (10\,\mu\text{m}, 100\,\mu\text{m})$. The procedure we use is based on interpolation. One way to interpolate between the training data is pointwise, for each point on the interval I_T. This procedure would capture every detail of the data, potentially also non-systematic ones. Instead we will reduce the dimensionality of the data from 700 values to $p+1$ values by choosing $p+1$ basis functions to project the data onto. Interpolation can then be performed between the coefficients c^i_T of the projection, where $i = 0, ..., p$. We hope to only capture the systematic evolution of the electric field with antenna thickness this way.

As basis functions, we use the Hermite-Gauss-function,

$$\psi_i(x) = \exp\left(\frac{-x^2}{2}\right) H_i(x), \tag{3.5}$$

where H_i are the Hermite-polynomials, because they naturally drop off to zero for $x \to \pm\infty$, much like our data. These function form a basis on $L^2(\mathbb{R})$, and for them to be

a valid basis for our data we need to rescale or intervals I_T accordingly. We choose to rescale the intervals to

$$I_{p,s}^{\text{rescale}} = (-s \cdot x_p^{\max}, s \cdot x_p^{\max}), \tag{3.6}$$

where we introduced a scaling parameter s, and $x_p^{\max}$ is the x-value, where the basis function of the highest degree used in the fit, ψ_p, has its last maximum before dropping off to zero due to the Gaussian envelope. The projection thus results in a function,

$$h_T^{p,s} = \sum_{i=0}^{p} \langle \mathcal{E}_T, \psi_i \rangle_{p,s} \, \psi_i = \sum_{i=0}^{p} c_T^{i,p,s} \psi_i, \tag{3.7}$$

where the inner product is evaluated on the interval $I_{p,s}^{\text{rescale}}$ (see Equation 3.2). Interpolating the coefficients $c_T^{i,p,s}$ on the antenna thicknesses of the training set, using linear or cubic spline interpolation, yields the continuous coefficients $c^{i,p,s}(T)$, which we use to define the predictor functions,

$$h_{\text{pred}}^{p,s}(T) = \sum_{i=0}^{p} c^{i,p,s}(T) \psi_i. \tag{3.8}$$

It is now time to evaluate the performance of the predictors by using the test set. As a measure, we use the average distance between the test data and the predictor on all thicknesses, T_i, of the test set,

$$\bar{d}^{p,s} = \frac{1}{9} \sum_{i=1}^{9} \left\| \mathcal{E}_{T_i} - h_{\text{pred}}^{p,s}(T_i) \right\|, \tag{3.9}$$

where the distance is evaluated on the interval I_{T_i}. The projections were performed with the *LinearRegression* module from the python library *sklearn*.

Figure 3.4 shows the performance of the model on a grid of s and p for both linear and cubic spline interpolation. Both plots show the same qualitative behavior, with the better performance to be found with cubic interpolation. For all values of s, the average distance decreases, when increasing p, eventually reaching a plateau. The plateau is approximately at the same average distance for all values of $s < 1$. One interpretation of this plateau, is that all systematic behavior of the training data has been captured at this point, and increasing the number of basis functions cannot further improve the models performance. Going to a very large number of basis functions, one would expect the performance of the model to decrease again, as non systematic features of the data start getting captured. Apparently, this is not the case yet for the values of p tested here.

The best perfomance of the model is found for $p = 64$ and $s = 0.85$. The average distance between test set and prediction is $\bar{d}_{\min} = 0.0093 \pm 0.0032$, where the error is the standard deviation. This outperforms significantly the distances from choosing coarse meshing and averaging over variations of the inner radius. Figure 3.5 shows the simulated and predicted electric fields, as well as their distance, for the best and worst

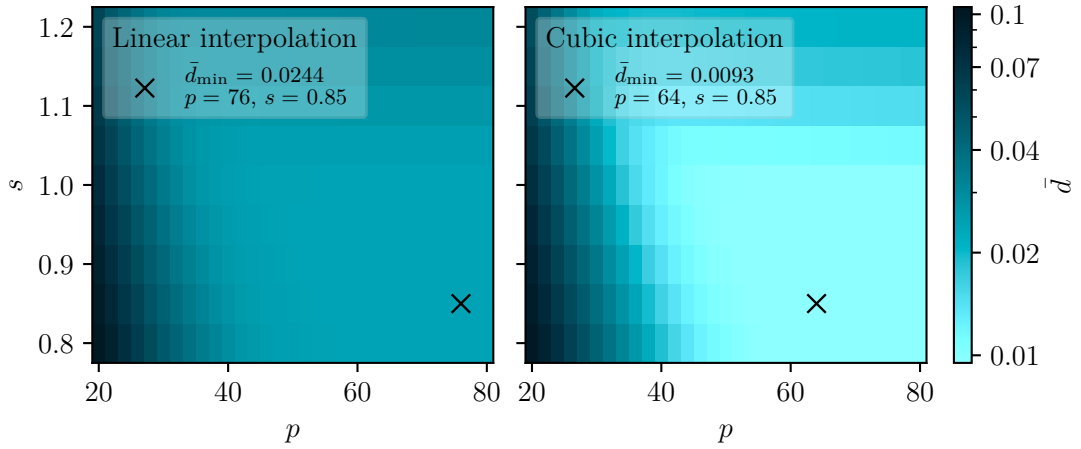

Figure 3.4.: Average distance $\bar{d}^{p,s}$ (see Equation 3.9) between simulations from test set and model prediction as a function of scaling parameter s, and number of basis functions p for linear and cubic interpolation. Colorbars are logarithmic for better visibility. The (p, s)-pair with the least distance is marked with a black X.

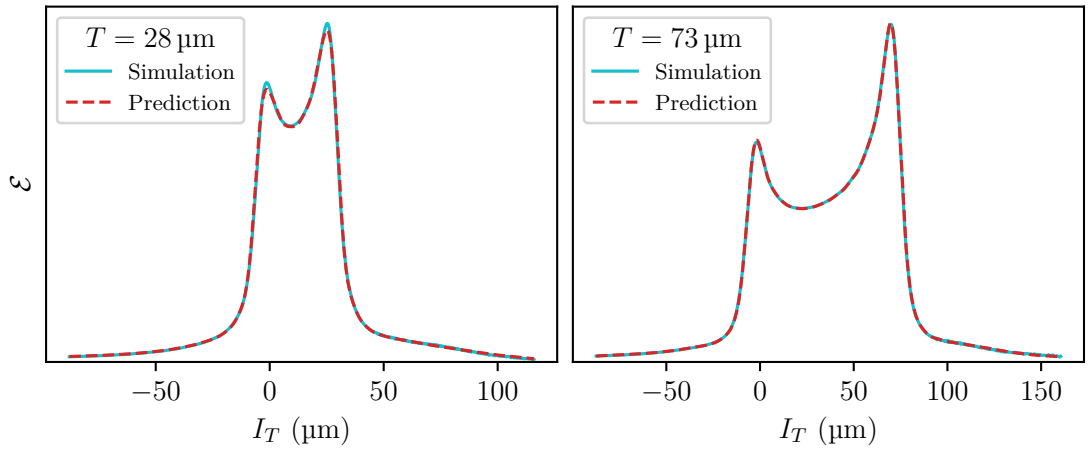

Figure 3.5.: Test data and model prediction for the antenna thickness with highest (left) and lowest (right) distance between simulation data and prediction for $p = 64$, $s = 0.85$, and cubic interpolation.

performing thickness from the test set. Even for the worst performance, the deviations between prediction and simulation can barely be spotted.

It is clear, that not the model itself but mostly the coarse meshing, and to some extend the preprocessing step of averaging fields of geometries with the same antenna thickness, limit the accuracy of predicting the electric field. This indicates that it could have been worth to decrease the number of simulated geometries, improve the meshing on those simulations, and perform a two-dimensional interpolation of the coefficients on antenna thickness and inner radius instead of averaging.

3.3. Optimization of HBAR geometries

With the improved prediction of the electric forcing field, let us now run the simulations on geometry optimization of the cylinder, spherical cap dome, and p-norm dome piezo shapes.

3.3.1. Cylinder

The cylinder has previously been optimized to $r_{\text{out}} = 253\,\mu\text{m}$, $r_{\text{cut}} = 266\,\mu\text{m}$, and $g_{\text{o,tot}} = 167\,\text{kHz}$, yielding a transduction efficiency of $\eta_t = 0.662$. Here, we rerun the optimization with some differences. The main differences are the improved electric field, and estimate of the electromechanical coupling $g_{\text{e,tot}} = 2\pi \cdot 75\,\text{kHz}$, whereas the previous optimization used $g_{\text{e,tot}} = 2\pi \cdot 250\,\text{kHz}$. Another minor difference is that previously, eight mechanical modes were simulated using DASE, but only the six with the strongest coupling were included in simulating the transduction sequence. This also led to slight inaccuracies. Here, we will use the first six mechanical modes for all calculation steps.

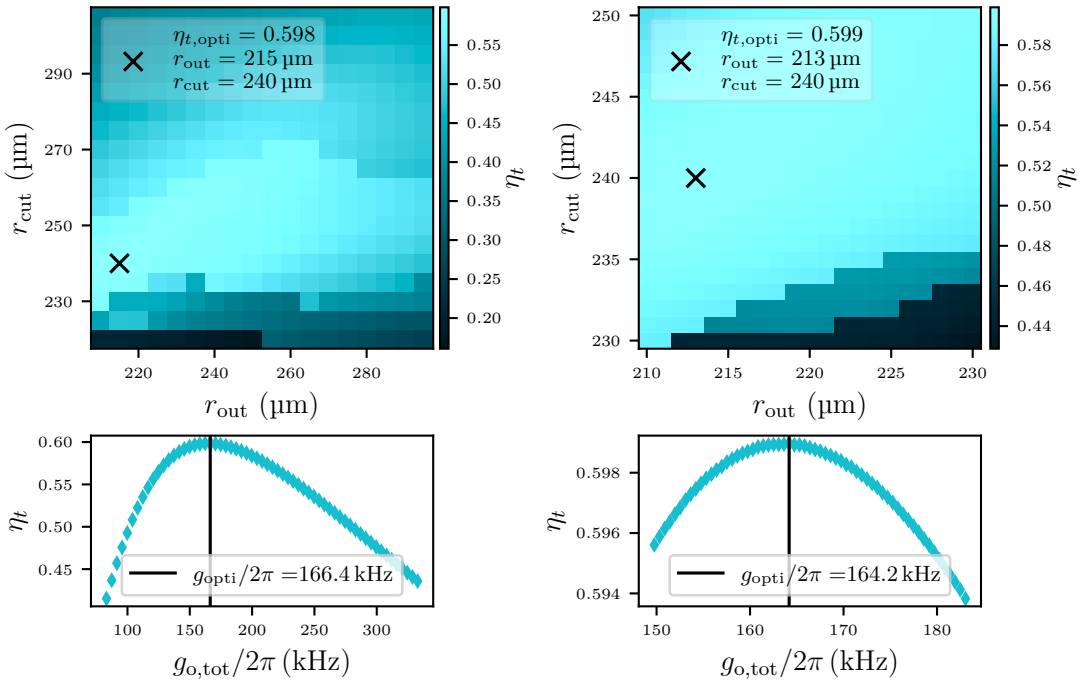

Figure 3.6.: Optimization of the cylinder HBAR geometry. Details in the text.

Geometry optimization procedure

Figure 3.6 shows the process of geometry optimization. We start with $g_{\text{o,tot}} = 167\,\text{kHz}$ and simulate the transduction efficiency on a wide grid of geometries, including all of

the training range of the electric field (upper left plot). We then proceed to find the optimal optomechanical coupling by simulating the optimized geometry, marked with a black cross, for different OM couplings (lower left plot). It is not obvious, why increasing the coupling too much, lowers the transduction efficiency, and we will comment on this in Section 4.2. With the optimal OM coupling, we repeat the two steps on a finer grid (right plots). The new optimal result for the cylinder is $r_{\text{out}} = 213\,\mu\text{m}$, $r_{\text{cut}} = 240\,\mu\text{m}$, and $g_{\text{o,tot}} = 164.2\,\text{kHz}$, yielding a transduction efficiency of $\eta_t = 0.599$. This result is similar to the previous one, with the main difference that a thinner antenna is favored. This could be the case, because the realistic forcing field is slightly broader than the antenna in contrast to the previous assumption of the forcing field.

The optimized geometry

The left column of Figure 3.7 plots the amplitudes of the mechanical mode functions together with the potential created by the piezo profile (upper plot). The mechanical modes are approximately described by the zeroth order Bessel function of the first kind. The forcing fields (center plot), have a Gaussian shape for the optics, or the shape resulting from Section 3.2 for the electric field. The bottom plot shows the EM and OM overlaps, where positive values are plotted in red, and negative ones in blue. We can observe that for the optimal geometry, the EM and OM overlaps draw a similar envelope, i.e. they are similar in magnitude for each mode. This favors rephasing of the electric bright state into the optical bright state.

Time dynamics in the optimized geometry

The time dynamics of the system are shown in the right column of Figure 3.7. The phonon populations (upper plot) increase to their maximum at the EM swap time, $t_{\text{sw}} = 4.41\,\mu\text{s}$, and then start to decline due to the optomechancial interaction and decoherence. Interestingly, not all phonon modes are strictly declining, but e.g. modes 0 and 1 are increasing in population at first. This is due to the multimode nature of the transducer, which causes different modes to have different phases with respect to the optical mode, and thus different time dynamics. We observe that modes one to three transfer most of the population, because of their large EM overlaps and because their mode detunings are smaller than $g_{\text{e,tot}}$.

The qubit excited state population p_{e}, the optical cavity population p_{o}, the transduction efficiency, and the population lost due to decoherence are shown in the center plot. We employed two y-scales for better visibility. The arrows in the legend indicate, which quantity is plotted on which scale. The qubit swaps almost all of its population to the mechanical modes during the EM interaction time. The optical mode population starts to increase as soon as the OM interaction is turned on, indicating that the mechanical state has already evolved away from the electric bright state to the optical bright state. The transduction efficiency is the integral of the optical population. It is evaluated at $t_{\text{OM}} = 25\,\mu\text{s}$ for the geometry optimization. At this time it has mostly saturated. The population lost due to decoherence is 3.5×10^{-3} at t_{OM}, indicating that the transduction

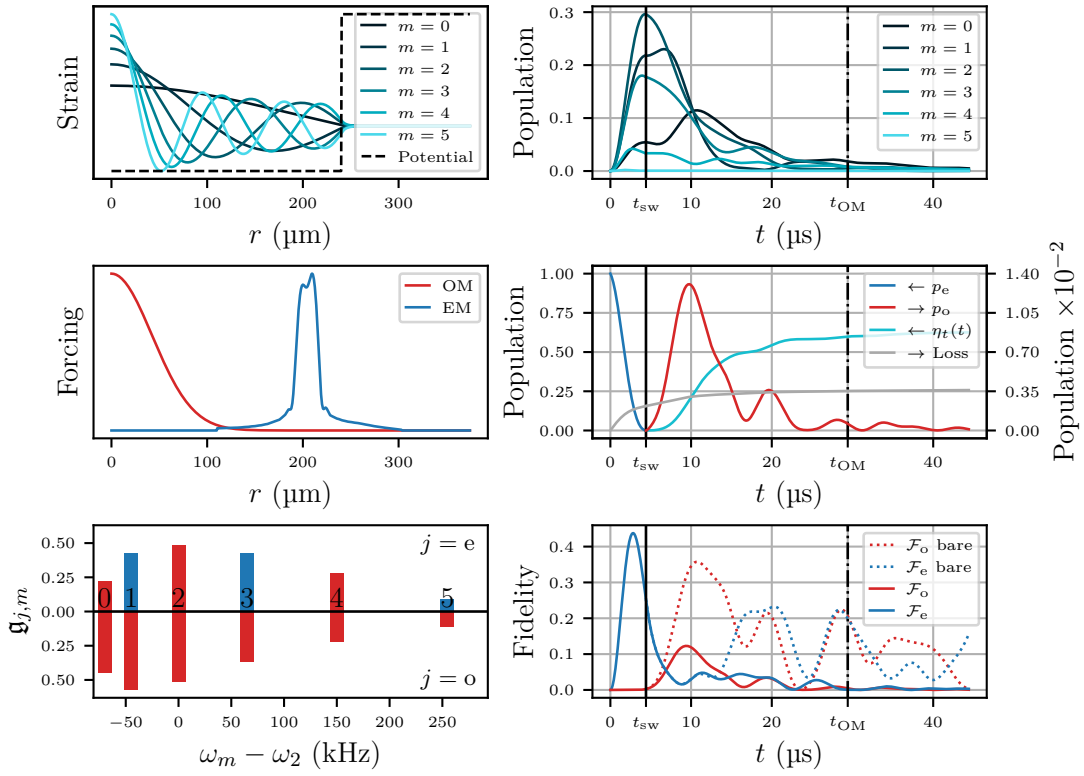

Figure 3.7.: Mode functions, forcing fields, and mode overlaps (left column), and time dynamics of populations and fidelities (right column) for the optimal geometry. Details in the text.

efficieny is not limited by decoherence in this simulation.

The mechanical bright state fidelities during the interactions are shown in the lower plot as solid lines. The electric bright state fidelity, $\mathcal{F}_e$, peaks already before t_{sw}, because the mechanical state evolves significantly already during the EM interaction. When starting the OM interaction, the optical bright state fidelity, $\mathcal{F}_o$, starts to increase to its maximum right away. Each peak in $\mathcal{F}_o$ coincides with a peak in the optical population because coupling is enabled. Interestingly, $\mathcal{F}_o$ never exceeds ~ 0.12. This is because population is transferred to the optical cavity, limiting $\mathcal{F}_o$. To get a feeling for how the pure mechanical phase evolution behaves, we plot $\mathcal{F}_e$ and $\mathcal{F}_o$ as a function of time in the absence of optomechanical interaction as dotted lines. Here, a maximum of $\mathcal{F}_o \sim 0.35$ is reached. The fidelity is limited by the nonuniform frequency spacing of mechanical modes, which prevents their phases to align at the same time. This imperfection is likely limiting the transduction efficiency in the end.

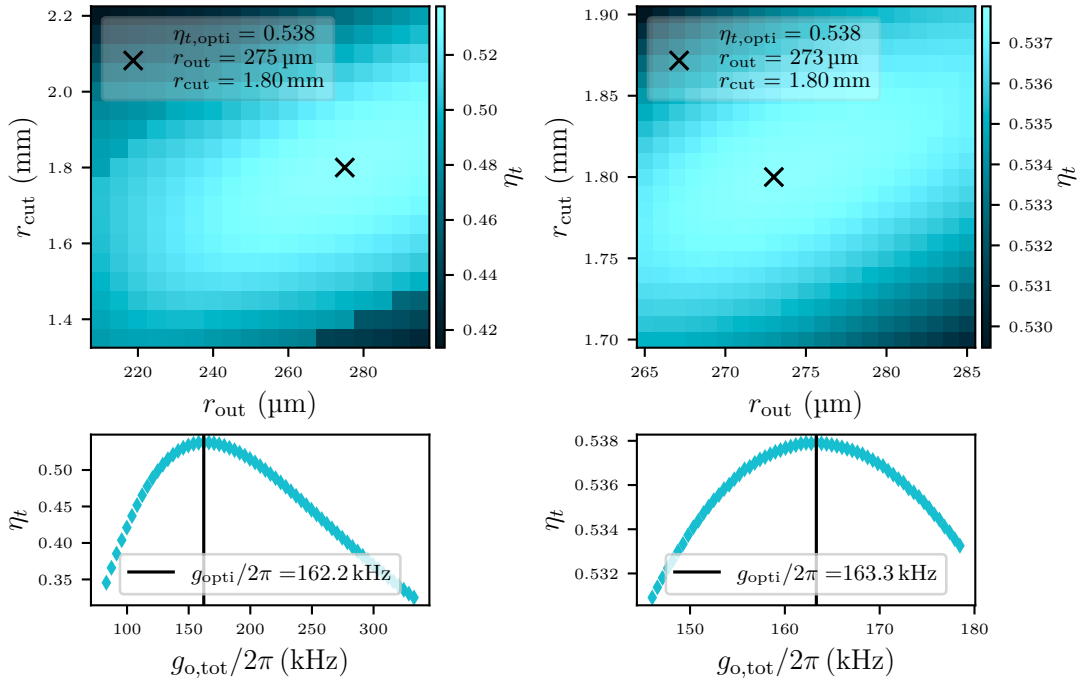

Figure 3.8.: Optimization of the spherical cap HBAR geometry. Details in the text.

3.3.2. Spherical cap dome

The spherical cap dome approximately produces a harmonic potential for the acoustic modes. It can be parametrized with either its cutoff radius r_{cut} or its radius of curvature R_{c}, which are related by $r_{\mathrm{cut}}^2 = (2R_{\mathrm{c}} - d_{\mathrm{p}})d_{\mathrm{p}}$, where $d_{\mathrm{p}} = 430\,\mathrm{nm}$ is the piezo thickness at the center of the dome.

Figure 3.8 and Figure 3.9 show the same plots as for the cylinder. Let us comment on similarities and differences. The geometry optimization is qualitatively very similar. There is an optimal geometry and optimal OM coupling, with decreasing efficiency around that point. Looking at the resulting optimal geometry though, we assert that a much larger structure with $r_{\mathrm{out}} = 273\,\mu\mathrm{m}$ and $r_{\mathrm{cut}} = 1.80\,\mathrm{mm}$ is optimal. The optimal OM coupling, $g_{\mathrm{o,tot}} = 2\pi \cdot 163.3\,\mathrm{kHz}$, is similar to the cylinder and the resulting transduction efficiency $\eta_t = 0.538$ is slightly lower.

We can understand the requirement for such large structures by looking at the mechanical mode functions. For the spherical cap dome, they are approximately the Laguerre-Gauss modes, which are confined much closer to the center of the dome than for the cylinder. This also makes it impossible to match the envelopes of the EM and OM overlaps, which is a disadvantage for rephasing into the optical bright state. This disadvantage is partially made up for, by the equal frequency spacing of the mechanical modes of the spherical cap dome, causing the phases of the modes to align at the same time.

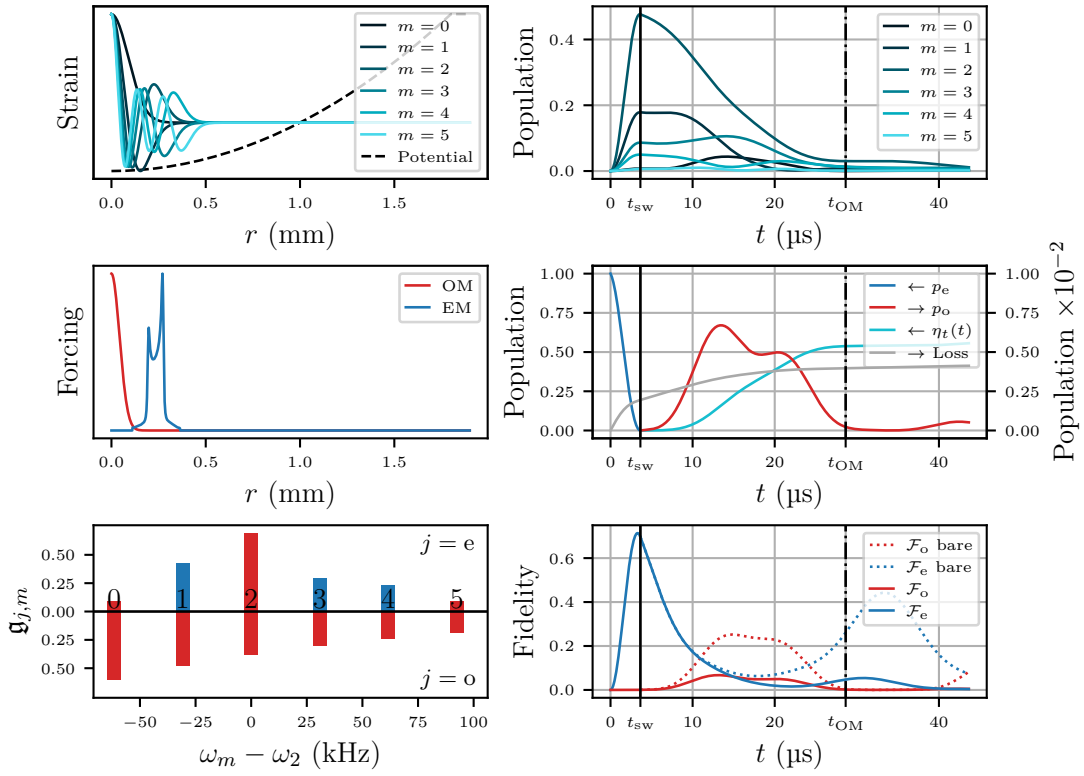

Figure 3.9.: Mode functions, forcing fields, and mode overlaps (left column), and time dynamics of populations and fidelities (right column) for the optimal geometry. Details in the text.

Looking at the time dynamics, mechanical mode 2 now clearly transfers most of the population due to its large EM overlap. Because the mode spacing for the spherical cap is smaller than the spacing between modes one to three for the cylinder, the overall rephasing dynamics are slowed down. One symptom of this is that $\mathcal{F}_e$ peaks at t_{sw}, instead of before t_{sw} like in the cylinder. Another symptom is that the optical population and bright state fidelity only start to increase $\sim 3\,\mu s$ after t_{sw}. Overall, the time dynamics are smoother and with less oscillations, which can be attributed to the equal frequency spacing. The bare evolution of $\mathcal{F}_o$ peaks below 0.3, which confirms that the rephasing dynamics of the spherical cap dome are slightly disadvantageous compared to the cylinder. Decoherence is again not limiting the transduction efficiency, as the decayed population is below 5×10^{-3} at t_{OM}.

3.3.3. p-norm dome

The p-norm dome's profile is defined as $p(r) = d_p - R_c + (R^p - r^p)^{1/p}$ for $r < r_{cut} = (R_c^p - (d_p - R_c)^p)^{1/p}$, where for $p = 2$ it is a sperical cap dome, and for $p \to \infty$, the

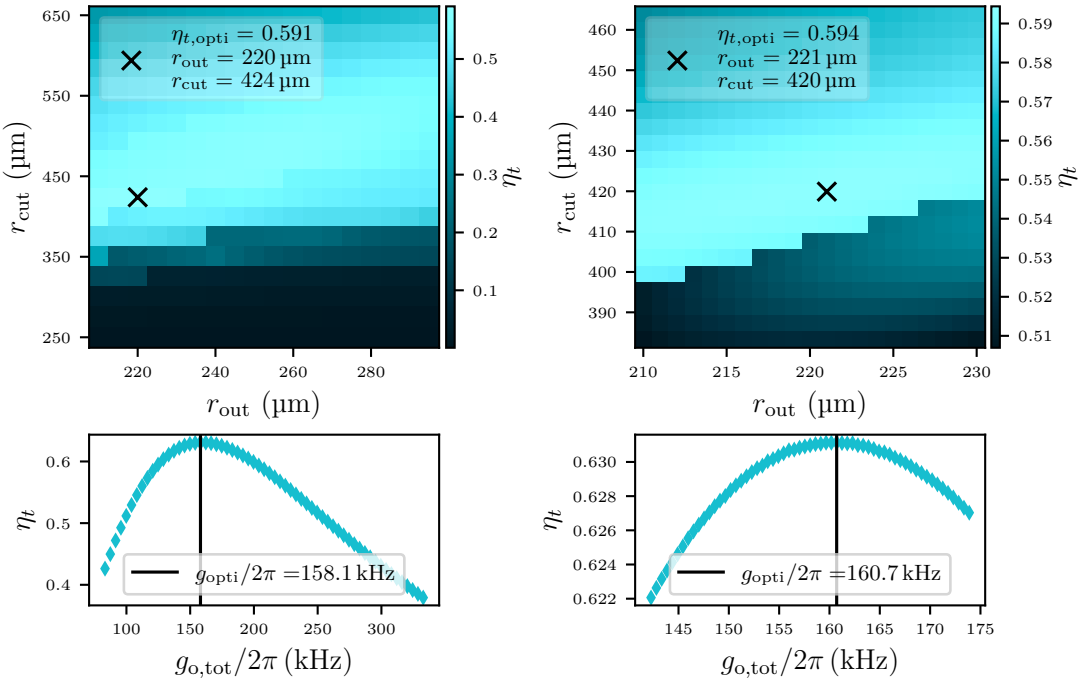

Figure 3.10.: Optimization of the p-norm dome HBAR geometry. Details in the text.

cylinder is recovered. Choosing an intermediate value of p, is a compromise between the cylinder and the spherical cap.

Figure 3.10 and 3.11 show the simulation results for $p = 6$. We see that indeed most of the aspects of the simululation are a comprimise between the cylinder and the spherical cap dome. The optimal structure has an intermediate size of $r_{\mathrm{cut}} = 420\,\mu\mathrm{m}$ and $r_{\mathrm{out}} = 221\,\mu\mathrm{m}$. The optimal OM coupling is similar to both other shapes with $g_{\mathrm{o,tot}} = 2\pi \cdot 160.7\,\mathrm{kHz}$, and the achieved transduction efficiency is similar to the cylinder with $\eta_t = 0.594$.

The mechanical mode functions are not as closely confined to the center of the potential as in the spherical case, but they also do not extend all the way to the cutoff radius. On one hand, the resulting EM and OM overlaps have envelopes which are more similar to each other than for the spherical cap, but less than for the cylinder. On the other hand, the frequencies of the modes are more regularly spaced than in the cylinder, but not equally spaced as in the spherical cap.

Three mechanical modes significantly participate in transduction, as we can see from the phonon populations. The rephasing speed seems to be similar to the cylinder, as p_{o} and $\mathcal{F}_{\mathrm{o}}$ start to incrase right at the beginning of the OM interaction. In the bare evolution, the p-norm dome is able to produce the highest value of $\mathcal{F}_{\mathrm{o}} \sim 0.4$, which however does not increase the final transduction efficiency over the cylinder because this high value is only maintained for a short time.

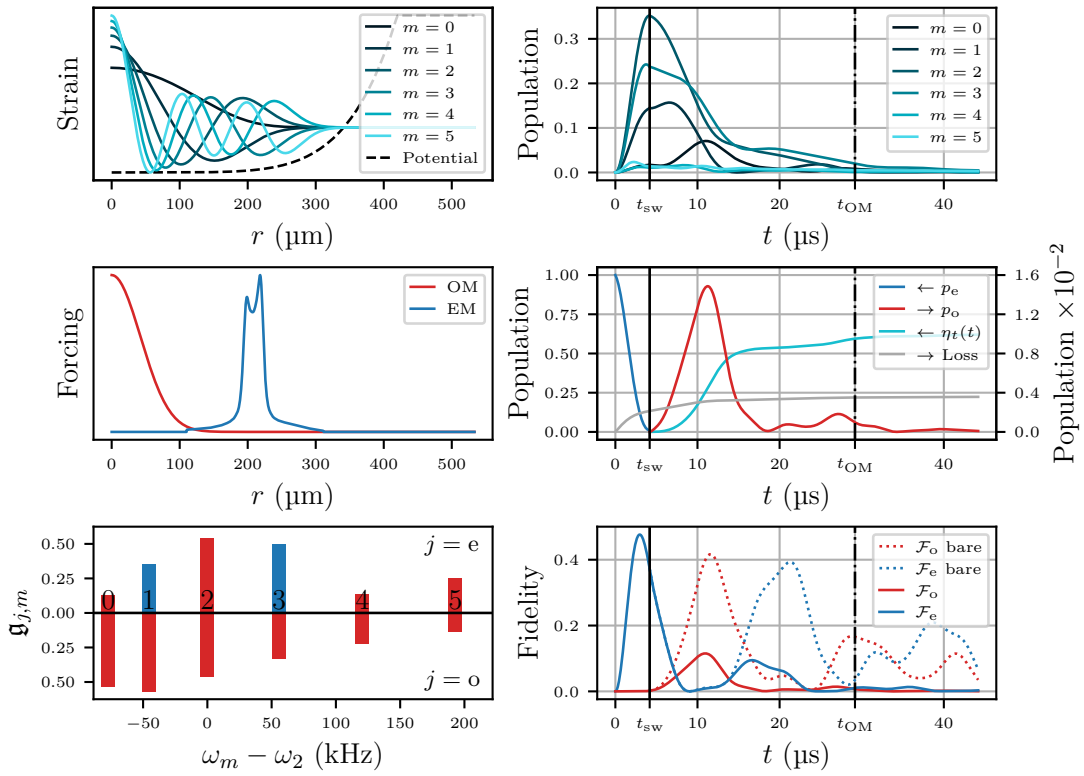

Figure 3.11.: Mode functions, forcing fields, and mode overlaps (left column), and time dynamics of populations and fidelities (right column) for the optimal geometry. Details in the text.

3.3.4. Discussion of the results

With the simulations in this section, we investigated how the multimode structure of HBARs in different geometries influences the transduction efficiency. For the chosen parameters, the efficiency was not limited by decoherence, but by the ability of the electric bright state to evolve into the optical bright state. In all investigated piezo shapes, the peak optical bright state fidelity was below $\mathcal{F}_{\mathrm{o}} \sim 0.4$ for bare mechanical evolution. Rephasing was either limited by nonuniform frequency spacing for the cylinder, differing overlap envelopes for the sphere, or a combination of the two for the p-norm dome. Perfect rephasing would require equal frequency spacing and equal envelopes of overlaps. This does not seem to be possible for the rotationally symmetric transducers investigated here.

From these simulations we can conclude, that neither piezo shape significantly outperforms the others, when it comes to transduction efficiency as the figure of merit. We should thus focus our attention to practical issues associated with the different shapes. In Chapter 5, we will measure the electromechanical interaction for the cylinder HBAR in the previously optimized geometry. In neither measurements, Rabi oscillations could be observed, which we concluded, is due to lacking phonon coherence times. This could in general be a problem for the cylinder HBAR, since the large mode amplitude at the edges of the mode volume could cause high diffraction loss, and loss to potentially rough cylinder walls. The group is very experienced in fabricating high quality spherical cap HBARs [23, 44], which is why the transduction team decided to move towards these structures as a results from the measurements. The disadvantage here is that large cutoff radii are necessary for the optimal geometry, introducing lots of piezoelectric material into the system, which could in turn limit qubit coherence. A solution to this, could be the double sided HBAR [45], which distributes the potential on both sides of the HBAR chip, limiting the piezoelectric material to the area of the qubit antenna. The p-norm dome could also provide an alternative, as its mode functions drop off way before the potential edges, promising high phonon coherence, while simultaneously limiting the amount of piezoelectric material needed. These alternatives come with the caveat, that they are more challenging to fabricate than the cylinder and spherical cap HBARs.

4. Microwave to optical transduction with two mechanical modes

In the last chapter, we saw that the time dynamics of multimode transduction are quite complicated. The goal of this chapter will be to develop a deeper understanding of the physics behind multimode transduction in a minimal toy model with two mechanical modes and perfect rephasing. Specifically, we will investigate how the EM and OM coupling rates, as well as the optical linewidth influence the transduction speed in the absence of qubit and mechanical loss.

In Section 4.1, we will try to extract as much information as possible from analytical calculations. Section 4.2 will then go on to simulate the transduction sequence in different parameter regimes. The results from the toy model will be discussed in Section 4.3. Finally, Section 4.4 introduces an HBAR geometry without rotational symmetry that approximately resembles the two mode toy model.

4.1. Analytical formulation

Let us write down the full transduction Hamiltonian for two mechanical modes in the rotating frame of the qubit frequency ω_q and the optical mode detuning Δ_{12},

$$\hat{H}_t = -\delta\hat{b}_1^\dagger\hat{b}_1 + \delta\hat{b}_2^\dagger\hat{b}_2 + g_{\mathrm{e},1}\hat{\sigma}^\dagger\hat{b}_1 + g_{\mathrm{e},2}\hat{\sigma}^\dagger\hat{b}_2 + g_{\mathrm{o},1}\hat{a}^\dagger\hat{b}_1 + g_{\mathrm{o},2}\hat{a}^\dagger\hat{b}_2 + \mathrm{H.c.}, \tag{4.1}$$

where 2δ is the detuning between the mechanical modes, $\hat{b}_i$ is the lowering operator for mechanical mode i, $g_{j,i}$ is the coupling rate for $j = \mathrm{e}, \mathrm{o}$ and $i = 1, 2$, and H.c. is the hermitian conjugate of the coupling terms. We will assume all couplings to be equal in magnitude and have all couplings positive with the exception of $g_{\mathrm{e},2}$ being negative. This gives the the electric and optical bright states (see Equation 2.24),

$$|B_\mathrm{e}\rangle = \hat{b}_\mathrm{e}^\dagger|0\rangle = \frac{1}{\sqrt{2}}\left(\hat{b}_1^\dagger - \hat{b}_2^\dagger\right)|0\rangle = \frac{1}{\sqrt{2}}\left(|1\rangle_1|0\rangle_2 - |0\rangle_1|1\rangle_2\right), \tag{4.2}$$

$$|B_\mathrm{o}\rangle = \hat{b}_\mathrm{o}^\dagger|0\rangle = \frac{1}{\sqrt{2}}\left(\hat{b}_1^\dagger + \hat{b}_2^\dagger\right)|0\rangle = \frac{1}{\sqrt{2}}\left(|1\rangle_1|0\rangle_2 + |0\rangle_1|1\rangle_2\right), \tag{4.3}$$

which satisfy the orthogonality of Equation 2.25. We can now rewrite Equation 4.1 in terms of the operators $\hat{b}_\mathrm{e}$ and $\hat{b}_\mathrm{o}$,

$$\hat{H}_t = g_{\mathrm{e,tot}}\hat{\sigma}_+\hat{b}_\mathrm{e} - \delta\hat{b}_\mathrm{e}\hat{b}_\mathrm{o}^\dagger + g_{\mathrm{o,tot}}\hat{a}^\dagger\hat{b}_\mathrm{o} + \mathrm{H.c.} \tag{4.4}$$

Notice that the energies of the mechanical modes disappeared and was replaced by a linear coupling at rate $-\delta$ between the bright modes. Figure 4.1 shows a sketch of the

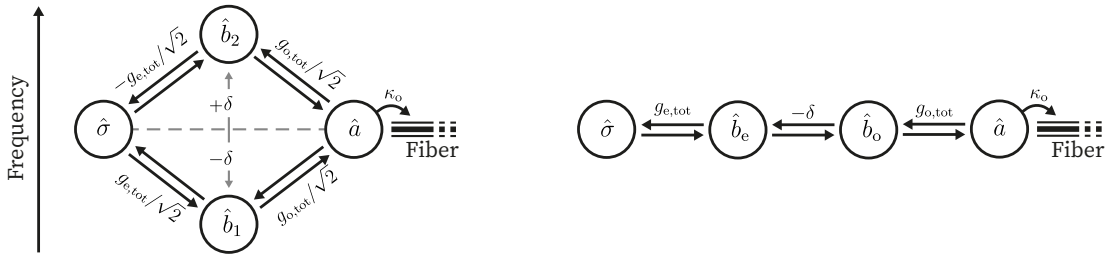

Figure 4.1.: Coupling scheme of the two mode toy model. Left: In the basis of mechanical eigenmodes. Right: In the basis of bright modes.

coupling scheme in the two mechanical bases. We will use the bright mode basis for further calculations.

Let us separate again the EM and OM interaction. Including only states with 1 excitation in total we can write the EM or OM Hamiltonian in matrix form,

$$\hat{H}_{\mathrm{XM}} = \begin{pmatrix} 0 & g & 0 \\ g & 0 & -\delta \\ 0 & -\delta & 0 \end{pmatrix}, \tag{4.5}$$

where we use the basis $\{|e\rangle, |B_{\mathrm{e}}\rangle, |B_{\mathrm{o}}\rangle\}$ ($\{|1\rangle_{\mathrm{o}}, |B_{\mathrm{o}}\rangle, |B_{\mathrm{e}}\rangle\}$), and $g = g_{\mathrm{e,tot}}$ ($g = g_{\mathrm{o,tot}}$) for the EM (OM) Hamiltonian. $|e\rangle$ is the qubit excited state, and $|1\rangle_{\mathrm{o}}$ is the single photon optical cavity state. Diagonalization of this matrix form Hamiltonian yields the eigenvalues $-\Omega, 0, +\Omega$ to the eigenstates $|-\rangle, |d\rangle, |+\rangle$, where $\Omega = \sqrt{g^2 + \delta^2}$,

$$|-\rangle = \frac{1}{\sqrt{2}} \begin{pmatrix} \cos\alpha \\ -1 \\ -\sin\alpha \end{pmatrix}, \quad |d\rangle = \begin{pmatrix} \sin\alpha \\ 0 \\ \cos\alpha \end{pmatrix}, \quad |+\rangle = \frac{1}{\sqrt{2}} \begin{pmatrix} \cos\alpha \\ 1 \\ -\sin\alpha \end{pmatrix}, \tag{4.6}$$

and we introduced the mixing angle, $\tan\alpha = \delta/g$. The state $|d\rangle$ is called the dark state as it has a vanishing eigenvalue and therefore does not evolve under the Hamiltonian.

4.1.1. Electromechanical interaction

Let us now compute the time evolution of the electromechanical interaction with initial state $|\psi_0\rangle = |e\rangle$,

$$|\psi(t)\rangle = e^{-i\hat{H}_{\mathrm{XM}}t/\hbar}|e\rangle = \sin\alpha\,|d\rangle + \frac{\cos\alpha}{\sqrt{2}}\left(e^{i\Omega t}|-\rangle + e^{-i\Omega t}|+\rangle\right) \tag{4.7}$$

$$= \left(\sin^2\alpha + \cos^2\alpha\cos\Omega t\right)|e\rangle - i\cos\alpha\sin\Omega t\,|B_{\mathrm{e}}\rangle \tag{4.8}$$

$$+ \cos\alpha\sin\alpha\,(1-\cos\Omega t)\,|B_{\mathrm{o}}\rangle\,. \tag{4.9}$$

While at first this seems a bit cluttered, let us ask the question if there is a time, t_{sw}, where the qubit swaps all of its population to the mechanics. The coefficient of the state

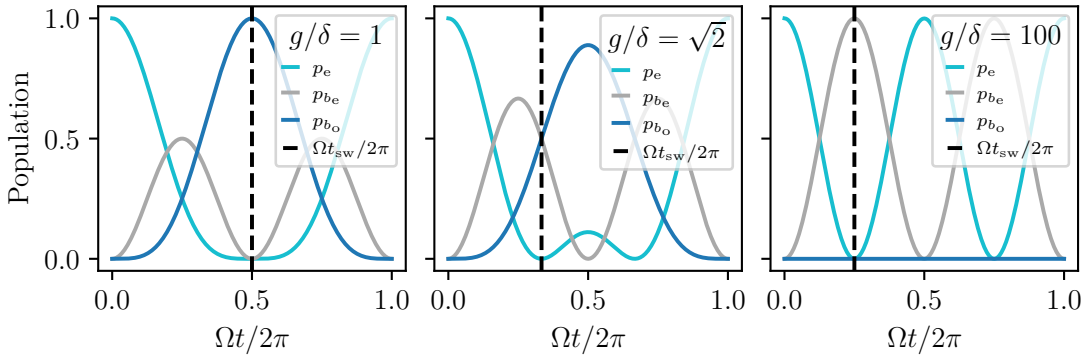

Figure 4.2.: Populations of qubit, and electric and optical bright states as a function of time (see Equation 4.7), evaluated at three ratios of g/δ. This ratio is responsible for the mechanical state resulting from the interaction at t_{sw}.

$|e\rangle$ in $|\psi(t)\rangle$ drops to zero if

$$\cos \Omega t_{sw} = -\tan^2 \alpha = -\frac{\delta^2}{g^2}, \tag{4.10}$$

which means that the swap time only exists if $g \geq \delta$, i.e. if the EM coupling is faster than the bare phase evolution of the mechanical state. The resulting mechanical state at this time is

$$|\psi(t_{sw})\rangle = \cos\frac{\varphi_0}{2}|B_e\rangle + \sin\frac{\varphi_0}{2}|B_o\rangle = \frac{1}{\sqrt{2}}\left(|1\rangle_1|0\rangle_2 - e^{-i\varphi_0}|0\rangle_1|1\rangle_2\right), \tag{4.11}$$

$$\tan\frac{\varphi_0}{2} = \frac{\delta\left(1+\frac{\delta^2}{g^2}\right)}{\Omega\sqrt{1-\frac{\delta^4}{g^4}}}, \tag{4.12}$$

which is a superposition of the electric and optical bright states whose weight depends on the ratio g/δ. Figure 4.2 shows the time evolution of the populations of the qubit excited state, p_e, and the electric (optical) bright state, p_{b_e} (p_{b_o}), for $g/\delta = 1$ (left), $g/\delta = \sqrt{2}$ (center), and $g/\delta = 100$ (right). For $g/\delta = 1$, the electromechanical swap time equals the rephasing time, such that the optical bright state results from the electromechanical interaction at t_{sw}. In the other extreme case, $g/\delta \to \infty$, rephasing is negligible during the EM interaction time, and the electric bright state is produced. It turns out that for $g/\delta = \sqrt{2}$, the electric and optical bright state become equally populated at t_{sw}.

In this toy model, we can thus prepare an arbitrary mechanical state with the EM interaction by choosing the parameters accordingly. In the following, we will simulate the OM-interaction, as it is analytically not well tractable because it contains dissipation of the optical mode. There, we will see the influence of starting in a specific mechanical state.

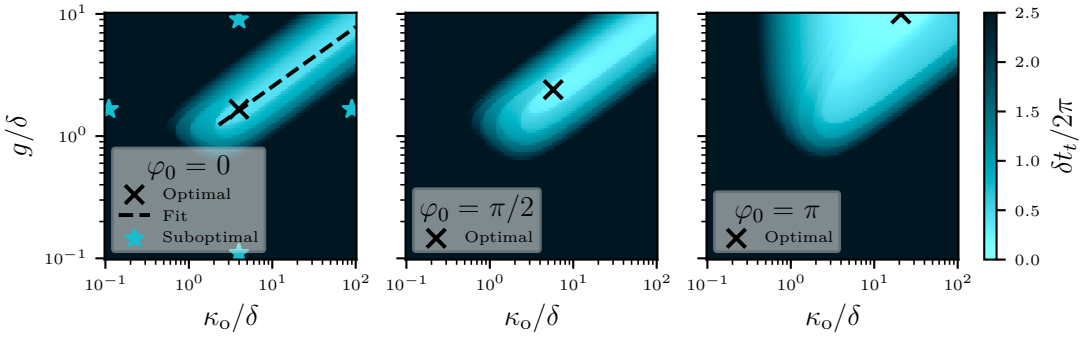

Figure 4.3.: Colormaps of the transduction time, t_t, as a function of g and κ_o for $\delta = 2\pi$. The three plots correspond to different values of φ_0, i.e. different initial mechanical states.

4.2. Simulations on the optomechanical interaction

Having established how mechanical states result from the EM interaction, let us now investigate how these states evolve under the OM interaction. This problem is slightly more complicated, as now the question is no longer, how population can be transferred between states, but how population can be transferred to a bath, which is the optical fiber leading to the SPDs. As always, we model this decay to the bath, with the optical cavity decay rate, κ_o. The dynamics of the interaction are fully governed by the parameters δ, $g = g_{o,tot}$, and κ_o.

4.2.1. Exploration of the parameter space

We will now run a brute force simulation, similar to the geometry optimization in Chapter 3, where we sweep the parameters g and κ_o for $\delta = 2\pi$, to find the optimumal values. As a figure of merit will use the transduction time, t_t, it takes to achieve $\eta_t(t_t) = 1 - e^{-3} \approx 95\,\%$. Figure 4.3 shows maps of the transduction time as a function of g and κ_o for the initial mechanical state being $|B_e\rangle$ (left), $\frac{1}{\sqrt{2}}(|B_e\rangle + |B_e\rangle)$ (center), and $|B_o\rangle$ (right), corresponding to the values $\varphi_0 = 0, \pi/2, \pi$. Transduction times exceeding $\delta t_t/2\pi = 2.5$ are colored with this maximum value.

In the case of $\varphi_0 = 0$, we can clearly observe a staff-shaped region of efficient transduction with an optimal value at $g/\delta = 1.66$ and $\kappa_o/\delta = 3.98$ (marked with a cross). We perform a power law fit of the type $g/\delta = a(\kappa_o/\delta)^b$ (dashed line) on all points with $\delta t_t/2\pi < 0.5$. The result is $a = 0.825 \pm 0.004$ and $b = 0.489 \pm 0.013$ for $\kappa_o \gtrsim \delta$, which tells us the relation of g and κ_o that leads to efficient transduction. We will develop a physical intuition for why transduction is inefficient outside this parameter regime in Subsection 4.2.3, where we look at the time dynamics of the points marked with stars.

Starting the OM interaction with $\varphi_0 = \pi$ on the other hand, a much wider parameter space results in efficient transduction. Towards lower values of g, the region of efficient

transduction is bound in the same way as for $\varphi_0 = 0$, but there seems to be no upper bound on the values of g, where the transduction time would decrease again. The optimal parameters are found on the edge of the simulation range for $g/\delta = 10$ and $\kappa_o/\delta = 20.9$.

When starting in the superposition state for $\varphi_0 = \pi/2$, a compromise between the two extreme cases has to be found, $g/\delta = 2.40$ and $\kappa_o/\delta = 5.75$. This compromise is rather close to the case of $\varphi_0 = 0$.

4.2.2. Transduction dynamics for optimal parameters

Figure 4.4 shows the time evolution of the transduction efficiency, η_t, the optical cavity population, p_o, and electric (optical) bright state population, p_{b_e} (p_{b_o}) for the optimal parameters found in Figure 4.3. For $\varphi_0 = 0$, a transduction time of $\delta t_t/2\pi = 0.41$ can be achieved. As in Section 3.3, the optical cavity population only starts to increase as soon as the electric bright state has partly rephased into the optical bright state. For $\varphi_0 = \pi$, The population is transferred much faster. Since initially $p_{b_e} = 0$, it is optimal to choose the coupling as high as possible, to have $|B_e\rangle \approx |d\rangle$, such that dynamics are essentially those of a driven two level system. The transduction time is then only limited by how fast the population can decay to the fiber, i.e. by κ_o. Here, a transduction time of $\delta t_t/2\pi = 0.06$ could be reached, but in principle this time can become arbitrarily low when increasing g and κ_o. For $\varphi_0 = \pi/2$, we can slightly increase the values of g and κ_o compared to the first case, since less population needs to rephase into the optical bright state, allowing for a smaller mixing angle. The transduction time achieved here is $\delta t_t/2\pi = 0.22$.

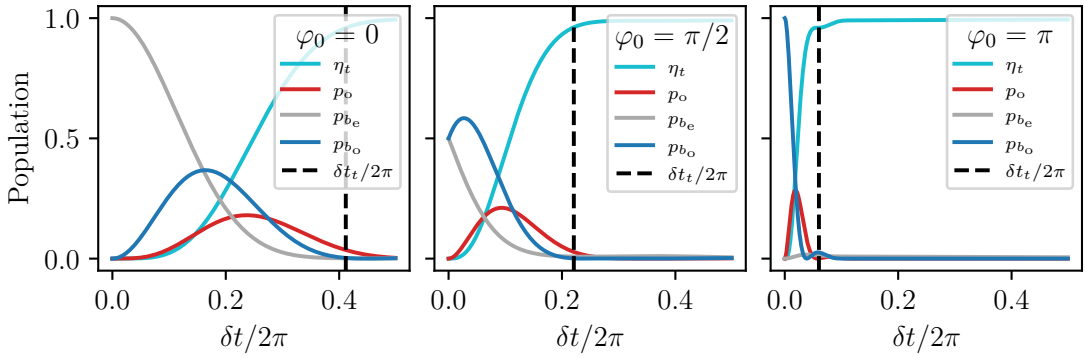

Figure 4.4.: Time dynamics of the transduction efficiency, η_t, optical cavity population, p_o, and electric (optical) bright state population, p_{b_e} (p_{b_o}) for different values of φ_0, in the case of optimal parameters found in Figure 4.3. The transduction time, t_t is marked with the black dashed line.

In Section 3.3, we saw that in realistic devices, we prepare mechancial states which have already evolved a decent amount from $|B_e\rangle$. In a transducer with a higher value of $g_{e,tot}$, states closer to $|B_e\rangle$ would be prepared in the EM interaction. For such a transducer, starting in the optical bright state could be implemented by a wait time, t_{wait}, between

the EM and OM interactions. Assuming that we can perfectly prepare the electric bright state, we would need to wait $\delta t_{\mathrm{wait}}/2\pi = 1/4$ ($\delta t_{\mathrm{wait}}/2\pi = 1/8$) before turning on the OM interaction, to start the latter with the optical bright state (equal superposition state) in this toy model. The total time to transduce the electric bright state to the optical fiber would therefore be $\delta t_0^{\mathrm{total}}/2\pi = 0.41$, $\delta t_{\pi/2}^{\mathrm{total}}/2\pi = 0.22 + 0.125 = 0.345$, and $\delta t_\pi^{\mathrm{total}}/2\pi = 0.06 + 0.25 = 0.31$, where we labeled the times with the values of φ_0 at the beginning of the OM interaction. The last value can probably be reduced further by exploring a larger parameter space. Here, the transduction time can thus be slightly reduced by waiting between the EM and OM interactions.

4.2.3. Transduction dynamics for suboptimal parameters

To build a physical intuition of why transduction is only efficient in a certain parameter regime, we look at the time dynamics of four parameter pairs, where transduction is inefficient for $\varphi_0 = 0$. The points are chosen such that either g or κ_{o} is at its optimal value, and the other one is at the edge of the simulated parameter space. Since three of the four points are outside the efficient transduction region for any φ_0, the explanations apply generally for those points.

Figure 4.5 shows the time dynamics of the transduction sequence for the four points marked with a star in Figure 4.3. The top row shows the two cases where g is optimal, but κ_{o} is not. If κ_{o} is lower than optimal (left), population is coherently exchanged between the mechanical states and the optics. The optical and electric bright state population oscillate at the frequency $\Omega = 1.94\delta$, while the optical bright state population oscillates with twice that frequency. Transduction is inefficient here, because only little population leaks from the optical state, and a large portion of the optical population is transferred back to the mechanics. Multiple oscillations are thus necessary to transduce an appreciable amount of population. If kappa is too large on the other hand (right), the optical population always stays close to zero, and the electric and optical bright state exchange population at rate 2δ. The time dynamics are thus fully dictated by the rephasing of mechanical states and no time scale related to the value of g is observed. This is because $\kappa_{\mathrm{o}} \gg g$, such that any dynamics resulting from optomechanical coupling of the optical bright state and the optical cavity quickly decays to steady state. To understand why this results in inefficient transduction, let us treat the system as a two-level transition with high decoherence (the optical cavity) driven by the optical bright state with the slowly varying drive strength, $\xi \propto g p_{b_{\mathrm{o}}}$. The transduction efficiency is then the integral of the average number of dissipated photons,

$$\left\langle \frac{\mathrm{d}N}{\mathrm{d}t} \right\rangle = \kappa_{\mathrm{o}} p_{\mathrm{o}}^{\mathrm{ss}} = \kappa_{\mathrm{o}} \frac{s}{2(s+1)} \approx \frac{\xi^2}{\kappa_{\mathrm{o}}}, \tag{4.13}$$

where $p_{\mathrm{o}}^{\mathrm{ss}}$ is the steady state value of the optical cavity population, $s = \frac{2\xi^2}{\kappa_{\mathrm{o}}^2}$ is the saturation parameter for resonant interaction, and we approximated the expression to linear order in $\xi^2/\kappa_{\mathrm{o}}^2$ [46]. This means that the transduction efficiency increases whenever the

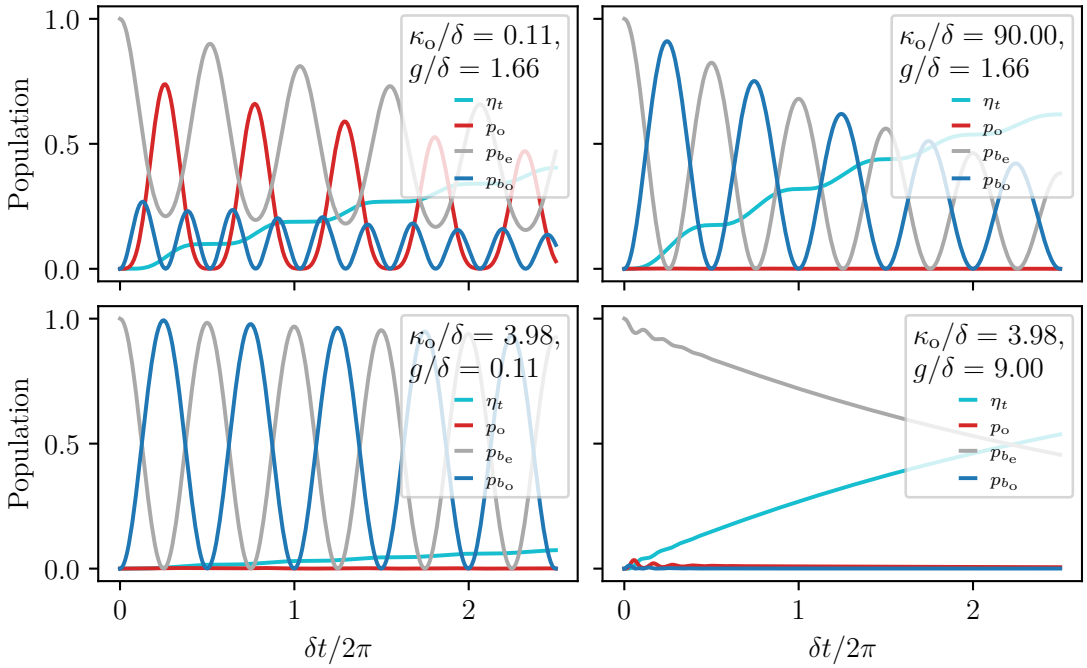

Figure 4.5.: Time dynamics of the transduction efficiency, η_t, optical cavity population, p_o, and electric (optical) bright state, p_{b_e} (p_{b_o}) for $\varphi_0 = 0$, in the case of suboptimal parameters, marked with a star in Figure 4.3.

population in the optical bright state is high, and that transduction is overall inefficient because $\left\langle \frac{dN}{dt} \right\rangle \propto \kappa_o^{-1}$.

In the bottom row, the cases of optimal κ_o and suboptimal g are shown. If g is too low (left), the optomechanical interaction is again in steady state. This is the same case as in the top right plot. It is very interesting what happens if we increase g beyond its optimal value. The mixing angle, α is very low in this case, so that the dark state, $|d\rangle$, has large overlap with the electric bright state, $|B_e\rangle$, which initially hosts all population. Only the small portion of population that is not in the dark state initially, participates in the time dynamics, giving rise to small oscillations in the population, which die out as soon as this population is transduced. The remaining population in the dark state, continues to sink very slowly due to inherited decay from the optical cavity. Starting the OM interaction with $\varphi_0 = \pi$, does not lead to these kinds of dynamics. This is because initially all population is in the state $|B_o\rangle$, which has zero overlap with the dark state. Increasing g to arbitrarily high values therefore does not hurt the transduction time (see Figure 4.3).

4.3. Discussion of the results

While in Section 3.3, we investigated how the geometry of HBARs influences the rephasing properties of the mechanical bright states. In this chapter we assumed perfect rephasing and investigated the influence of the parameters $g_{\mathrm{e,tot}}$, $g_{\mathrm{o,tot}}$ and κ_{o} on the transduction time, neglecting decoherence of the qubit and the mechanics. Let us evaluate which findings we can apply to the realistic transducers.

In the toy model, we found that in the EM interaction all population could be swapped from the qubit to the mechanical states, resulting in a superposition of electric and optical bright states depending on the mixing angle. In the simulation of all realistic transducers, the EM swap resulted in almost zero qubit population, and a mechanical state with only moderate electric bright state fidelity. Especially for the cylinder, the mechanical state at t_{sw} had low values of $\mathcal{F}_{\mathrm{e}}$ and $\mathcal{F}_{\mathrm{o}}$. This behavior is only possible with more than two mechanical modes.

We then went on to simulate the OM interaction and found that when starting in the electric bright state, there is an optimal value of g for $\kappa_{\mathrm{o}} > \delta$, due to the formation of eigenstates under the OM Hamiltonian. Including more mechanical modes in the realistic device gives rise to similar eigenstates, which is why we observed an optimal value of $g_{\mathrm{o,tot}}$ in the optimization process.

Furthermore, we found in this chapter that including a wait time between the EM and OM interaction can be beneficial to the transduction time, because the OM interaction time can be reduced indefinitely by increasing g when starting in the optical bright state. Experimentally, the optomechanical coupling is tuned by the intracavity photon number, which scales with the applied pump laser power and inversely scales with κ_{o}. The experiment sets a limit on the maximum pump power, as the attenuation of the pump laser light needs to be strong enough such that detection of pump photons by the SPDs is rare compared to the detection of signal photons. We estimated that we can achieve values of $g_{\mathrm{o},n} \approx 2\pi \cdot 230\,\mathrm{kHz}$ (see Appendix A), assuming the strongest value, $g_{0,n} = 2\pi \cdot 7.75\,\mathrm{Hz}$, observed in the previous OM experiment of the group [25]. This photon enhanced coupling rate of a single mode, n, is significantly higher than the optimal total coupling rate of $g_{\mathrm{o,tot}} \approx 2\pi \cdot 160\,\mathrm{kHz}$ found in the simulations of Section 3.3. It might therefore be advantageous to include a wait time in the transduction experiment, to make use of these large coupling rates.

So far in this chapter, we developed an understanding of the physics of an idealized multimode transducer. In the following section, we will try to find an HBAR geometry that behaves similarly to this toy model.

4.4. HBARs in double-well geometry

A realization of the two mode transduction example can be constructed from two individual HBARs. As the first device we pick an $\hbar$BAR of the type in reference [22], where the qubit antenna electric field overlaps almost exclusively with the fundamental mode of a spherical cap HBAR. For the second device, we pick an optomechanical system of the type in reference [33], again with exclusive overlap of the laser to the fundamental mode of the HBAR. We can think of the mechanical modes in the separate HBARs as the electric and optical bright states. If the two HBARs have the same geometry, they host indistinguishable phonons. Bringing the domes closer together enables tunneling of the phonons between the localized states, at a rate J, which gives rise to symmetric and antisymmetric hybridized eigenmodes, with frequency splitting $\delta = J$. In this particular geometry, the rephasing dynamics we investigated in this chapter are equivalent to tunneling of phonons between the localized electric and optical bright states.

In the following, we construct a physical realization of the double-well HBAR geometry. For this we use the potential,

$$U(x, y) = A(x^2 - a^2)^2 + By^2, \tag{4.14}$$

which is a quartic potential in x-direction with steepness A and minima at $\pm a$, and a harmonic potential in y-direction with steepness B. We assume that the centers of the qubit pad antenna and the laser are at a distance of 200 µm, and the optical waist to be $w_0 = 60\,\mu\text{m}$ as previously. The parameter B is set by requiring perfect overlap between the optical forcing field and the fundamental mode of the harmonic oscillator in the y-direction. This yields $B = \frac{8}{\mu w_0^4} = 5922\,\text{m}^{-2}$, where μ is the effective mass of the ASE (see Equation 2.3). The parameters of the potential in x-direction, A and a, are optimized for total overlap of the laser field with the hybridized modes, $\mathfrak{g}^2_{\text{o,tot}} = \mathfrak{g}^2_{\text{o,1}} + \mathfrak{g}^2_{\text{o,2}}$, with a brute force parameter sweep. This gave the values $a = 106\,\mu\text{m}$, $A = 171 \times 10^9 \text{m}^{-4}$, and $\mathfrak{g}^2_{\text{o,tot}} = 0.998$. As a last step, the radius of the qubit pad antenna, r_p, is optimized for total electromechanical overlap, $\mathfrak{g}^2_{\text{e,tot}} = \mathfrak{g}^2_{\text{e,1}} + \mathfrak{g}^2_{\text{e,2}}$. For simplicity, we assume a simple door function as the electric forcing field. The optimal antenna radius is $r_p = 48\,\mu\text{m}$ yielding a total overlap of $\mathfrak{g}^2_{\text{e,tot}} = 0.810$. The hybridized mechanical modes were simulated with 2D-DASE (see Subsection 3.1.2) for this optimization. Figure 4.6 shows the piezo profile creating the potential of Equation 4.14 on the left, and a cut through the x-axis on the right, which displays the forcing functions, mechanical mode functions and the potential. We can see that the potential barrier between the two wells is large enough to localize the individual parts of the hybridized modes in their respective wells, which results in large forcing overlaps.

In principle, the latter design is very close to the toy model we investigated in this chapter. The tradeoff for the large forcing overlaps in this design, is relatively weak mode hybridization. The resulting frequency splitting between the hybridized mechanical modes, $2\delta = 2\pi \cdot 104\,\text{Hz}$, is way too low to be useful in any experiment, because the transduction time, $t_t = 0.41 \cdot 2\pi/\delta = 7.9\,\text{ms}$ (see Figure 4.4), exceeds the expected lifetime of phonons in HBARs by orders of magnitude. A way to speed up the process,

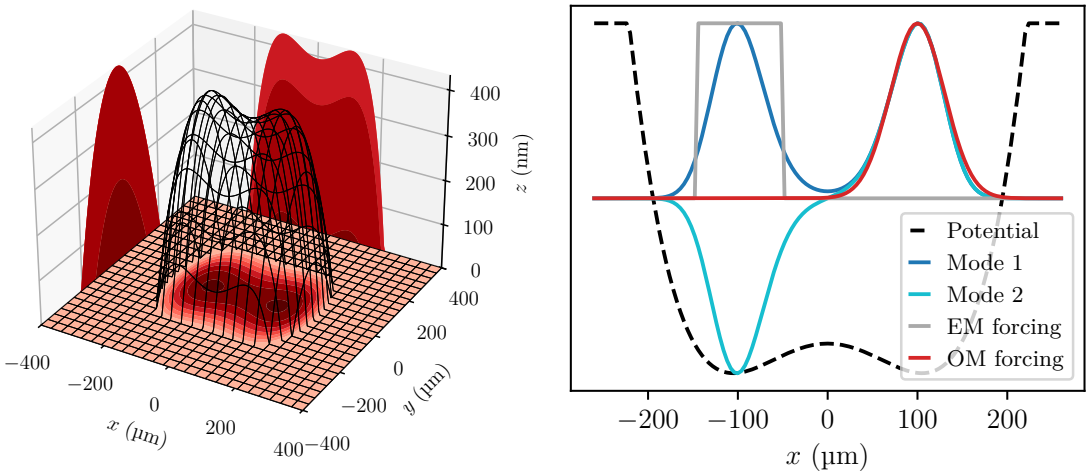

Figure 4.6.: First design of a double-well HBAR. Left: Double well profile of AlN on quartz (see Equation 4.14) that results from optimization of forcing overlaps. Right: Potential, forcing functions, and displacement amplitudes of the hybridized mechanical modes at $y = 0$.

is to choose a geometry with stronger mode hybridization. For the following design we require $t_t < 50\,\mu s$, i.e. $2\delta > 16.4\,kHz$, and see how we can vary the parameters of the double-well to match this requirement. The mode detuning can be adjusted with the parameters A and a by lowering the potential barrier. We keep the forcing functions from the last design and do a parameter sweep to maximize the overlaps to $\mathfrak{g}^2_{e,tot} = 47.46\,\%$ and $\mathfrak{g}^2_{o,tot} = 61.43\,\%$, under the transduction time constraint. The resulting potential uses the parameters $a = 76\,\mu m$ and $A = 17.3 \times 10^9 m^{-4}$. Figure 4.7 shows corresponding piezo profile (left), and the first two mechanical modes together with the forcing fields. We see that the reduced transduction time comes at a cost of worse EM and OM overlaps. The double-well potential basically merged into a single elongated well, where the former symmetric mode is now a single peak. Having less overlaps with the two modes shown, means that overlap to higher order mechanical modes increases, and the device is no longer an example of a two mode transducer. This is visualized in Figure 4.8 where the EM (top) and OM (bottom) overlaps to the mechanical modes of the first (left) and second (right) double-well HBAR are shown. The first design is indeed a good example of a two mode transducer. In fact, the mode spacing between these two modes is so small, that it the corresponding bars completely overlap in the plot. The second design has significant overlap with four mechanical modes within the first 100 kHz and is no longer a two mode transducer.

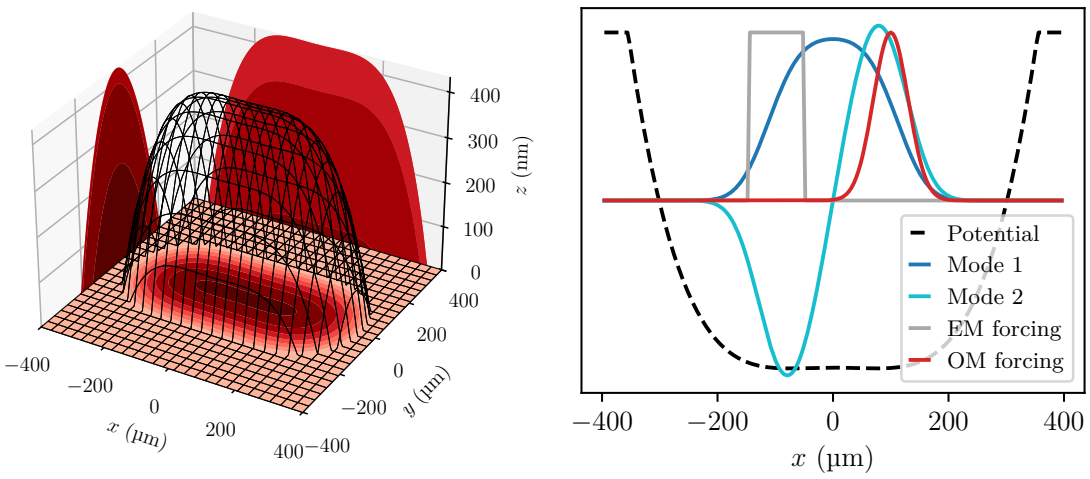

Figure 4.7.: Second design of a double-well HBAR. Left: Double well profile of AlN on quartz (see Equation 4.14) that results from constraining the transduction time. Right: Potential, forcing functions, and displacement amplitudes of the hybridized mechanical modes at $y = 0$.

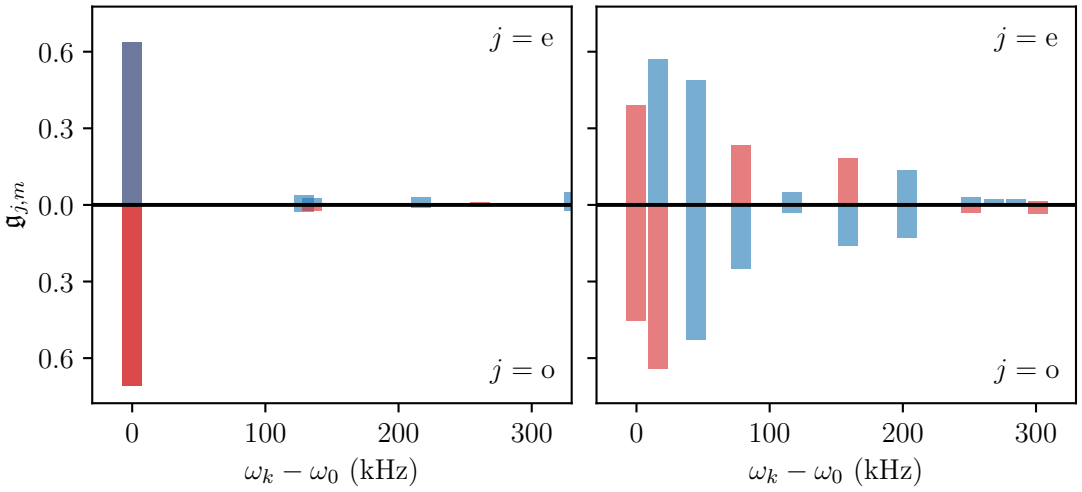

Figure 4.8.: EM (top row) and OM (bottom row) overlaps with the mechanical eigenmodes of the two potentials shown in Figure 4.6 (left plot) and 4.7 (right plot). Red bars represent positive and blue bars negative values. In the left plot, the bars representing overlap to the fundamental and first excited mode completely overlap due to the small frequency difference.

The examples in this section showed an important tradeoff that has to be made in HBAR transducers. In general the size of the transducer is set by the electric and optical forcing functions, which must not overlap. For a given size, a two mode transducer with perfect efficiency comes at the cost of reduced speed. For the same size, a faster transducer can be built using multiple strongly hybridized modes, which might not have perfect rephasing properties. The HBARs with rotational symmetry investigated in Chapter 3 are an extreme example of strongly hybridized modes, where the notion of localized modes does not really exist. They are thus much faster than the double-well HBAR with strongly localized modes.

A possible path towards a fast transducer with perfect rephasing could be a geometry similar to the one in Figure 4.7, but with a harmonic profile in x-direction. The harmonic potential would lead to uniform frequency spacing of mechanical modes, and the symmetry plane at $x = 0$ could lead to similar EM and OM forcing overlap envelopes. The combination of the two would result in high fidelity rephasing even with more than two mechanical modes. Simulations on this geometry were unfortunately out of the scope of this work.

5. Measurements on cylinder HBARs

In this chapter we will present the results of electromechanical measurements performed on HBARs with cylinder piezo shapes, flip-chip bonded to a superconducting qubit, i.e. $\hbar$BARs. The purpose of these measurements is to extract information about phonon coherence and electromechanical coupling strengths.

Three devices of this kind were measured. An overview of which is presented in Table 5.1, where we label the devices with the cooldown (CD) number of the dilution refrigerator that they were measured in. The device CD 38 is designed in the geometry resulting from optimization prior to this work (see Figure 3.1). Out of the three, it is closest to the design of the final transduction device as its qubit has a ring antenna and a frequency close to the Brillouin frequency in quartz, $\Omega_B = 12.64\,\mathrm{GHz}$ (see Subsection 2.2.2). The same HBAR was bonded to a qubit with lower frequency and a pad antenna in CD 43 in order to obtain data on its phonon coherence at this frequency. Finally, a second HBAR was bonded to this qubit in CD 45 for more statistics. The main difference between the two HBARs is their surface roughness and their distance from the qubit antenna. Figure 5.1 shows pictures of the devices CD 38 and CD 43. Note that the antenna of CD 43 is misaligned by about 20 µm from the center of the HBAR. Unfortunately there is no picture available for CD 45.

As we will see in Section 5.3 the devices measured are not in the strong coupling regime. Section 5.1 thus gives a brief overview of the relevant aspects of cQAD in the weak-coupling regime. Next, the measurement procedure and apparatus will be described in Section 5.2. In Section 5.3 to 5.6 the measurement data will be analyzed and discussed.

device label	CD 38	CD 43	CD 45
qubit label	W2424-TR09	W2430-L14	
qubit antenna	ring	pad	
qubit frequency	11.4 GHz	6.1 GHz	
HBAR label	W2405Q3-D20		W2446Q2-D19
AlN cylinder radius	266 µm		266 µm
AlN thickness	425 nm		430 nm
HBAR-antenna-gap	2.4 µm		0.9 µm
surface roughness (RMS)	4.2 nm		11.9 nm

Table 5.1.: Overview of measured $\hbar$BARs.

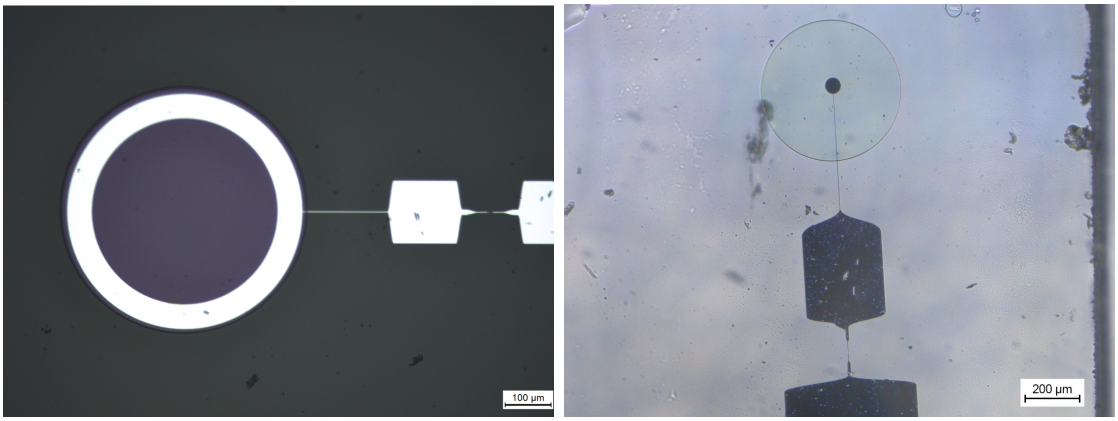

Figure 5.1.: Photographs of the devices CD 38 (left) and CD 43 (right). The antenna of CD 43 is misaligned by about 20 µm from the center of the HBAR.

5.1. The weak-coupling regime of cQAD

Here we give a brief introduction to the behavior of a weakly coupled cQAD-system. The unitary dynamics of the system are governed by the electromechanical Hamiltonian (see Equation 2.20),

$$\hat{H}_{\mathrm{EM}}/\hbar = \omega_q \hat{\sigma}^\dagger \hat{\sigma} + \sum_n \left(\omega_n \hat{b}_n^\dagger \hat{b}_n + g_{\mathrm{e},n} \left(\hat{b}_n \hat{\sigma}^\dagger + \hat{b}_n^\dagger \hat{\sigma} \right) \right), \tag{5.1}$$

where the sum includes all kinds of mechanical modes, i.e. longitudinal and transversal mode numbers as well as polarizations. We assume Markovian decoherence for both the qubit and mechanical modes at the qubit relaxation and pure dephasing rates, γ and γ_ϕ, and the relaxation and pure dephasing rates, Γ_n and $\Gamma_{\phi,n}$, of the phonon mode n. Additionally, we assume the environment to be at zero temperature.

If the coupling strengths exceed the decoherence, we expect vacuum Rabi oscillations between the qubit and phonon populations. This is called strong-coupling and is required for high effieciency transduction. As we will see in Section 5.3, no coherent oscillations but only exponential decay of the qubit population are observed in this experiment, indicating that the phonon modes act as an incoherent environment for the qubit. This is the weak-coupling regime of cQAD.

A similar situation has been studied in the context of qubit decoherence due to an environment of incoherent two-level-systems (TLS) [47, 48]. Although phonon modes are harmonic oscillators, which have more than two levels, they behave identically to TLS if we assume them to be in the ground state initially. This is because the Jaynes-Cummings interaction in Equation 5.1 couples the phonon ground state only to the first excited state, such that higher phonon Fock states cannot get populated. Solving the master-equation for the coupled system in the limit $\Gamma_n > g_{\mathrm{e},n} > \gamma$ yields the phonon

enhanced qubit decay rate [47],

$$\gamma_1(\omega_q) = \gamma + \sum_n \frac{2g_{e,n}^2 \kappa_{2,n}}{\kappa_{2,n}^2 + (\omega_q - \omega_n)^2}, \tag{5.2}$$

where $\kappa_{2,n} = \gamma/2 + \gamma_\phi + \Gamma_n/2 + \Gamma_{\phi,n}$ is the total decoherence rate. We observe that each phonon mode enhances the intrinsic qubit relaxation rate γ by a Lorentzian profile around its resonance frequency. By measuring γ_1 as a function of frequency ω_q we can thus extract information about the decoherence rates $\kappa_{2,n}$ and coupling rates $g_{e,n}$. This will be the main goal of this chapter.

5.2. Experimental methods

The measurements in this work use standard techniques from cQED. We will thus only briefly cover some relevant aspects here. For a detailed treatment we refer to references [1, 49]. Subsection 5.2.1 presents the basic principle of dispersive qubit readout, Subsection 5.2.2 sketches the experimental setup, and Subsection 5.2.3 introduces the relevant calibration measurements for this experiment.

5.2.1. Dispersive qubit readout

Qubit readout is performed via dispersive coupling of the qubit at rate g to a microwave readout resonator at frequency ω_r, where $|\Delta| = |\omega_q - \omega_r| \gg g$. In this regime the system Hamiltonian is well approximated by the dispersive Hamiltonian,

$$\hat{H}_{\text{disp}}/\hbar = \left(\omega_r + \chi \hat{\sigma}^\dagger \hat{\sigma}\right) \hat{r}^\dagger \hat{r} + \omega_q \hat{\sigma}^\dagger \hat{\sigma}, \tag{5.3}$$

where $\hat{r}$ is the microwave resonator's lowering operator, and $\chi = \frac{2g^2\alpha}{\Delta(\Delta+\alpha)}$ is the dispersive shift. The interpretation of this Hamiltonian is, that the resonator frequency depends on the qubit state, such that it is equal to $\omega_r + \chi$ if the qubit is in the excited state, and ω_r if it is in the ground state. By measuring the transmission of the resonator, we can thus infer the qubit state. This is commonly refered to as dispersive readout. Figure 5.2 shows how the transmission and the phase of the transmitted signal theoretically behave for the two qubit states [1].

The readout resonator is implemented as a stripline resonator on the qubit chip for CD 38 (see Figure 3.1) and as a 3D microwave cavity for the other devices. For all measurements presented here, we choose to readout the qubit state by measuring the amplitude of the resonator transmission at the frequency ω_r. If the qubit is in the ground state, the amplitude will be maximal, while it will be suppressed if the qubit is in the excited state.

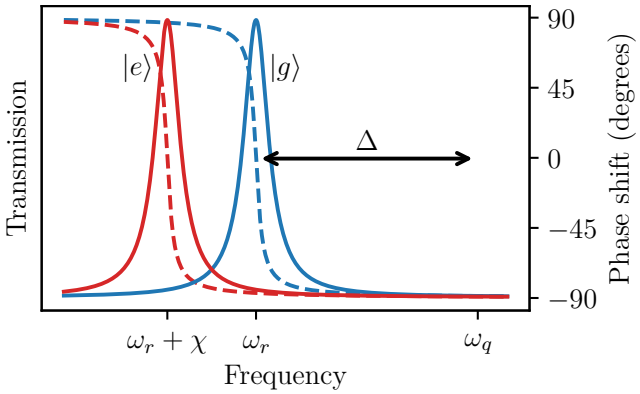

Figure 5.2.: Resonator transmission (solid line lines) and corresponding phase shifts (dashed lines) for the two qubit states (blue, ground; red, excited). The resonator response strongly depends on the state of the qubit. Frequency differences are not to scale. Adopted from [1].

5.2.2. Experimental setup

Figure 5.3 shows a schematic of the experimental setup. The $\hbar$BAR coupled to its readout resonator is mounted at the base plate of a dilution refrigerator (hereafter fridge) from *Bluefors*, which has a temperature of $T_{\text{base}} \approx 10\,\text{mK}$, when cooled down. This is necessary to operate the qubit as well as the phonon modes close to their quantum ground state, where quantum effects dominate over thermal fluctuations. Several attenuators at different temperature stages of the fridge ensure that thermal photons cannot reach the sample through the input line. A circulator isolates the sample from noise coming from the output line. The experiment requires signal generation at the qubit frequency for direct manipulation of the qubit state, and at the resonator frequency for qubit readout. The signals are generated independently and combined in a directional coupler. Each signal is composed of two frequency components, which are combined in an IQ-mixer [50] by *mini-circuits*. When calibrated (see Subsection 5.2.3), the mixer outputs a signal at the sum or difference frequency of the two components, depending on its calibration. The first frequency component is produced by a signal generator from *Windfreak* (*Rhode & Schwarz*), called the local oscillator (LO), which provides a stable sinusoidal wave the frequency ω_q^{LO} (ω_r^{LO}). This frequency is detuned from the qubit (resonator) frequency by $+50\,\text{MHz}$ ($-200\,\text{MHz}$). The second frequency component is provided by *Quantum Machines'* Operator-X [51] (OP-X). The OP-X creates arbitrary waveforms in a frequency range of 0 to 500 MHz, called the intermediate frequency (IF), for the qubit (resonator) signal at ω_q^{IF} (ω_r^{IF}). It is thus responsible for shaping pulses and sweeping the frequency.

Signal detection is only required at the resonator frequency. The signal coming from the output line of the fridge is down-converted to ω_r^{IF} by mixing it with the resonator-LO in an image-rejection-mixer [50]. The OP-X then records the I- and Q-

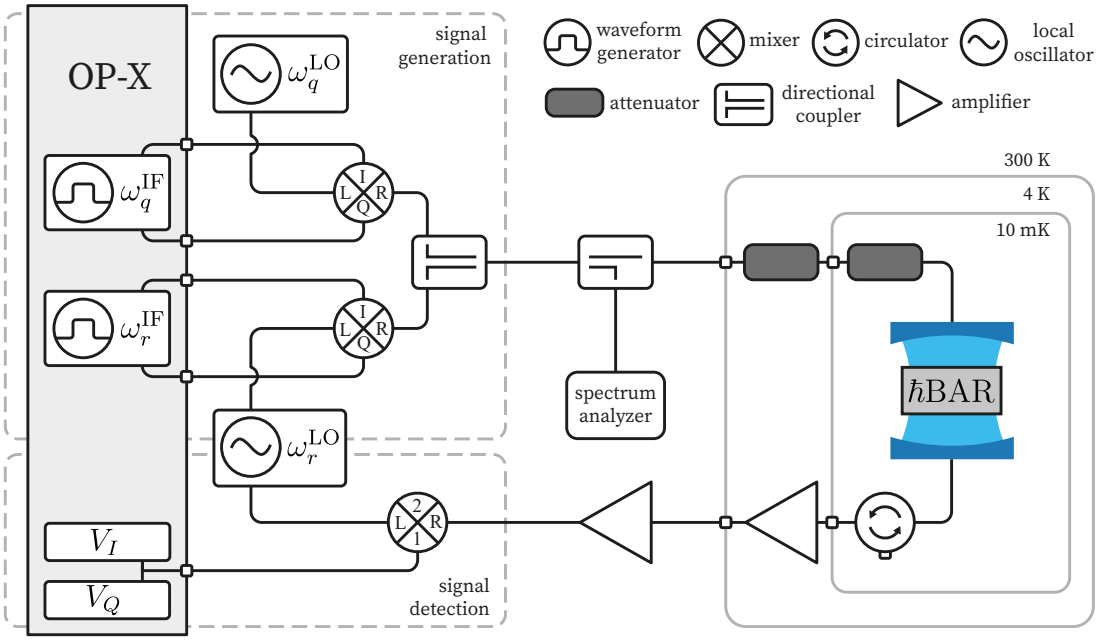

Figure 5.3.: Sketch of the most relevant microwave components for performing measurements on the ħBAR inside a microwave resonator.

quadratures of the down-converted signal, which can be converted to an amplitude and a phase. For the measurements presented here, we only require the average amplitude $V_{\text{meas}} = \left\langle \sqrt{V_I^2 + V_Q^2} \right\rangle$. A small fraction ($-30\,\text{dB}$) of the input signal is recorded in a spectrum analyzer (SA), which is necessary for mixer calibration and useful for monitoring purposes.

5.2.3. Device calibration

Before performing the electromechanical measurements, it is necessary to do calibration steps. We will use measurements from CD 43 as an example in this section. The calibration measurements for the other devices can be found in Appendix B.

Qubit readout and drives

Basic requirements for the experiment are the knowledge of the qubit and resonator frequencies, as well as the the ability to perform qubit rotations and readout. The first step towards this is the calibration of the IQ-mixers. Mixing the the LO-signal at ω^{LO} with the OP-X signal at ω^{IF} and direct current (DC) results in the creation of a carrier at ω^{LO} and upper and lower sidebands at $\omega^{\text{LO}} \pm \omega^{\text{IF}}$. By calibrating the DC-amplitudes and the ratio of amplitudes between the I- and Q-output channels of the OP-X, the mixed signals constructively interfere at the frequency of one sideband, while destructively

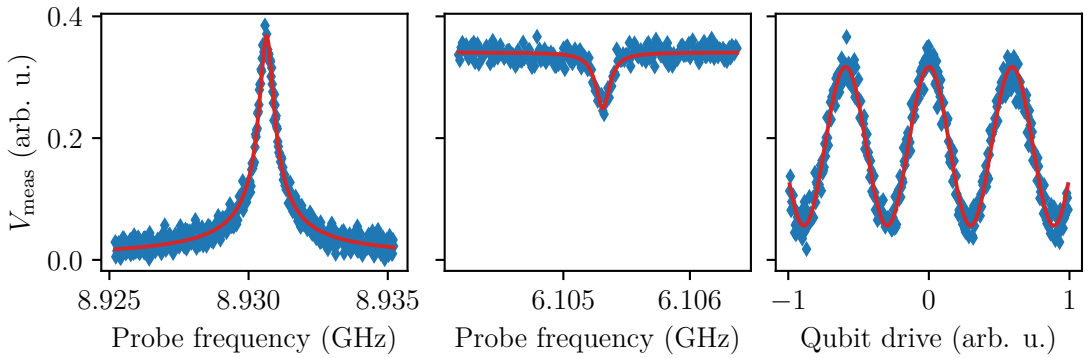

Figure 5.4.: Resonator frequency (left), Qubit frequency (center), and π-amplitude (right) calibration measurements (blue) and fits (red) for CD 43.

interfering at the carrier frequency and the other sideband frequency. By controlling ω^{IF} and the amplitude of the OP-X output, one can generate flexible waveforms at the constructively interfering sideband. Since the correct mixer calibration depends on the frequencies, amplitudes, and bandwidths of the generated signals, it should be redone when changing any of these parameters drastically. In this experiments, mixer calibration is done with an automatized software, which controls the OP-X output, while monitoring the mixed signal on the SA. More on mixer calibration can be found in [52].

To find out the resonator and qubit frequencies, we perform spectroscopy measurements. For the resonator spectroscopy, we record the resonator transmission as a function of frequency. We then fit a Lorentzian function to the resonance, which allows us to extract the resonance frequency ω_r and the linewidth of the resonance. We will perform dispersive qubit readout by applying a readout pulse at ω_r in all future measurements. The average voltage V_{meas} is then related to the qubit ground state population by an affine trasnformation. Qubit spectroscopy is done by applying a long pulse at variable probe frequency followed by qubit readout. If the probe frequency matches the qubit's resonance, the qubit is driven and it eventually saturates to steady state. By averaging, we arrive at a spectrum with a notch with Lorentzian shape at the qubit frequency ω_q, which we extract by fitting. For full control of the qubit, we now need to calibrate the qubit drive amplitude required to perform a π-rotation. For this we apply a Gaussian pulse with a fixed duration at the qubit resonance, followed by qubit readout. Varying the drive amplitude and averaging results in Rabi oscillations on which we perform a sinusoidal fit. We call the amplitude of the first minimum in the oscillations the π-amplitude. Figure 5.4 shows the three calibration measurements for CD 43, where the the measured data is plotted as blue diamonds and the Lorentzian and sinusoidal fits as a red solid line.

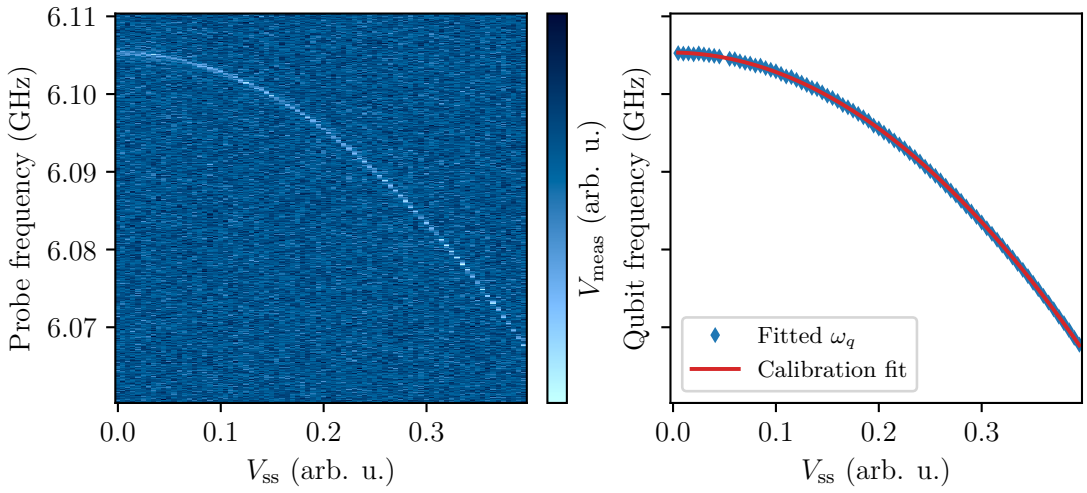

Figure 5.5.: Stark shift to frequency calibration for CD 43. Left: Qubit spectroscopy for different Stark shift amplitudes. Right: Fitted qubit frequencies (blue) and fitted calibration curve (red).

Stark shift to frequency calibration

In Section 5.1, we saw that information about electromechanical couplings and phonon coherences can be extracted from measurements of the qubit relaxation rate at different frequencies. This requires control of the qubit frequency, which we achieve by applying an off-resonant drive with frequency ω_d and strength ξ_d to the qubit. The drive induces a frequency shift on the qubit, the so called Stark shift $\delta_{\text{Stark}} = \frac{\alpha\xi_d^2}{2\Delta_d(\Delta_d+\alpha)}$, where $\Delta_d = \omega_q - \omega_d$ [39]. In this setup, the drive is applied at the frequency ω_r^{LO} by changing the DC-output of the OP-X from the calibrated value. This way the carrier of the resonator signal will have a nonzero amplitude, V_{ss}, instead of destructively interfering. We call this the Stark shift amplitude.

In order to match a given Stark shift amplitude to a frequency shift, a calibration measurement is performed (see Figure 5.5). In this measurement, qubit spectroscopy is done for a set of Stark shift amplitudes (left plot). Performing a second order polynomial fit on the resulting qubit frequencies (right plot) yields a function which converts between Stark shift amplitude and qubit frequency.

Qubit decoherence

As we saw in Section 5.1, extracting information about phonon coherence, requires knowledge about the bare qubit relaxation rate γ, and pure dephasing rate γ_ϕ. These can be extracted from standard T_1-measurements and T_2^*-Ramsey-measurements [49], examples of which are shown in Figure 5.6 for CD 43. To extract the T_1 and T_2^* values we fit an exponential decay and a sinusoidally modulated exponential decay respectively.

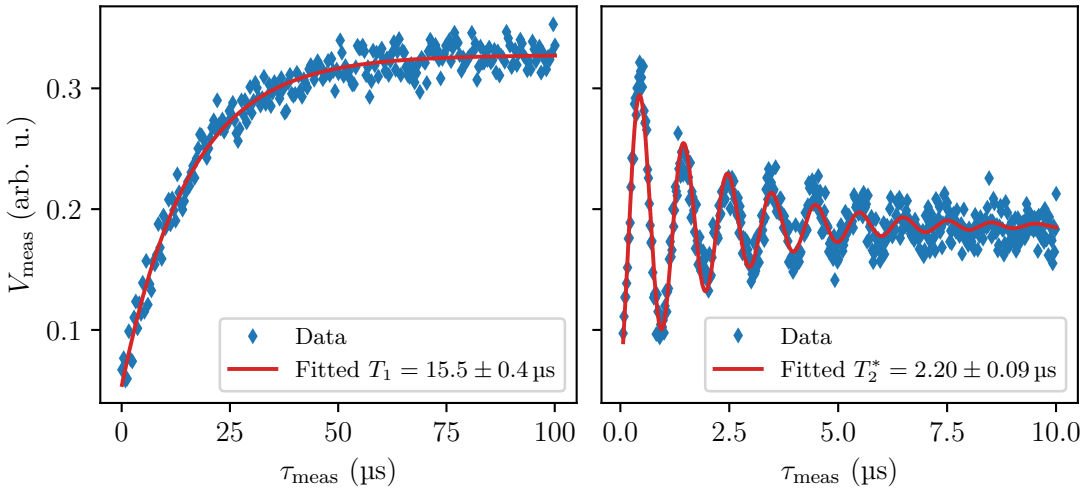

Figure 5.6.: Qubit T_1-measurement and T_2^*-Ramsey-measurement for CD 43.

device label	CD 38	CD 43	CD 45
$\omega_q^{\mathrm{meas}}/2\pi$ (GHz)	11.4180	6.10115	6.04287
bonded $\gamma_\phi/2\pi$ (kHz)	239±8	67.5±1.7	8.2±0.4
unbonded $\gamma_\phi/2\pi$ (kHz)	none	3.7±2.2	3.7±2.2

Table 5.2.: Qubit dephasing rates (Equation 5.4) of the two qubits before and after bonding to the HBAR, and the frequency where the measurements were performed for the bonded case. Errors are from linear error propagation of Equation 5.4.

Since γ will be a fit parameter of the model, we only need to determine

$$\gamma_\phi = \frac{1}{T_2^*} - \frac{1}{2T_1} \tag{5.4}$$

from calibration measurements.

In the devices measured here, it is hard to tell what are the bare qubit decoherence rates, as coupling to the incoherent phonon modes induces additional decoherence. The best we can do is measure the qubit dephasing at a frequency ω_q^{meas}, where the influence of phonon modes is minimized, to get an upper bound on γ_ϕ. A lower bound can be obtained from qubit measurements of a previous CD before the qubit was bonded to an HBAR. Table 5.2 shows the result of these measurements. Unfortunately, there are no available data for CD 38 before bonding.

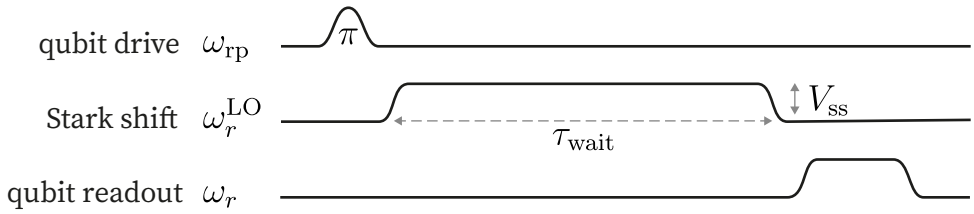

Figure 5.7.: Sequence of applied pulses for a single run of the qubit T_1 spectroscopy measurement.

5.3. Qubit T_1-spectra

Let us now turn to the electromechanical measurements. We will go through the analysis step by step, simultaneously for the three devices.

To obtain data about phonon coherence and coupling strengths, we record the temporal evolution of the qubit population as a function of qubit frequency. Figure 5.7 shows the sequence of pulses of a single run of this measurement. The qubit starts at its rest point frequency ω_{rp}, and is excited with a π-pulse. After that, the qubit is Stark shifted to a frequency ω_q by applying a voltage V_{ss} at the frequency ω_r^{LO}. After a time τ_{wait} of evolution due to qubit-phonon interaction and decoherence, it is measured with dispersive readout. The results is averaged over $n_{\mathrm{avg}} = 10^3$ runs for each pair $(\omega_q, \tau_{\mathrm{wait}})$. The average voltage V_{meas} is related to the qubit ground state population by an affine transformation.

The spectra for CD 43 and CD 45 were recorded in five to seven chunks and concatenated afterwards. The data for CD 38 were obtained by Tom Schatteburg, a PhD-student from the group.

Spectrum of CD 38

Figure 5.8 shows the recorded spectrum for CD 38 in the left plot. As will be the case for all recorded spectra in this work, no vacuum Rabi oscillations, but only a modification of the qubit's decay rate due to the phonons are observed. This a sign of weak coupling as discussed in Section 5.1. For each frequency, we fit an exponential decay of the form,

$$V_{\mathrm{meas}}(\tau_{\mathrm{wait}}) = A - B \exp\left(-\gamma_1 \tau_{\mathrm{wait}}\right), \tag{5.5}$$

to the measured voltage, where γ_1 is the fitted decay rate, and the fit parameters A and B account for the affine relation between V_{meas} and the qubit ground state population.

We plot the extracted decay rates γ_1 as a function of frequency in the right plot of Figure 5.8. The decay rates have a baseline at around 140 kHz with two peaks emerging up to 220 kHz. We can estimate the frequency spacing between the two peaks to be around 3.3 MHz, which is consistent with the expected FSR for longitudinally polarized phonons, $\mathrm{FSR}_l = 3.17\,\mathrm{MHz}$ (see Subsection 2.1.2). From this, we can conclude that the device CD 38 shows weak coupling between the qubit and longitudinally polarized phonon modes. We will proceed in Section 5.4 with further analysis.

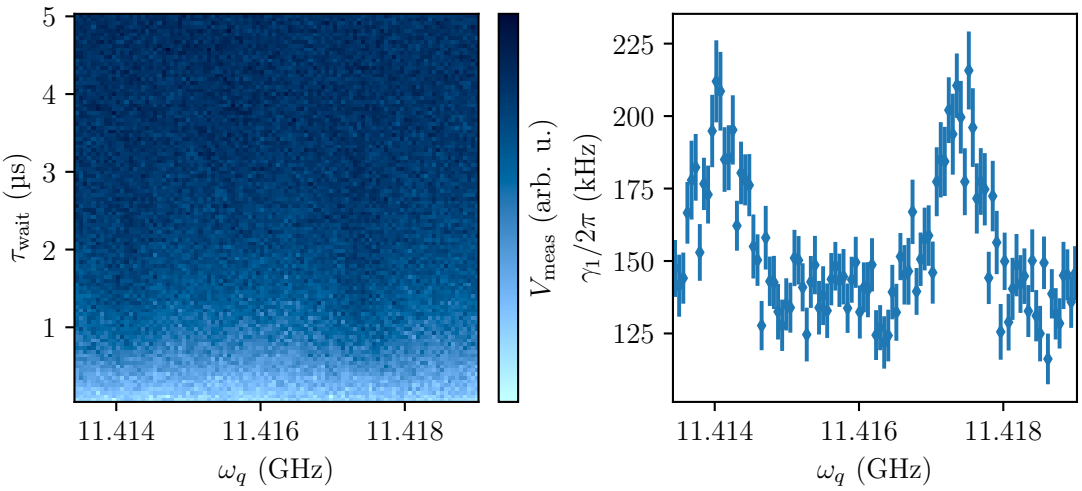

Figure 5.8.: T_1-spectrum (left) and fitted decay rates (right) for CD 38.

Spectra of CD 43

Figure 5.9 shows the spectrum (top), and fitted decay rates (center) of CD 43. The frequency range is much larger here, spanning several longitudinal FSRs, and the wait time range was chosen larger due to longer qubit coherence times. Looking at the decay rates, the structure is much more complicated than in CD 38. Most notably, it is different from peaks occurring at the periodicity of the longitudinal FSR.

To make sense of this structure, we compute the fast Fourier transform (FFT) of the decay rates (bottom plot of Figure 5.9) in order to find out, at which periodicity, features in decay rates occur. The two largest contributions in the FFT occur at 2.3 MHz and 3.1 MHz, which match the expected FSR for transversely and longitudinally polarized phonon modes, $\mathrm{FSR}_t = 2.34\,\mathrm{MHz}$ and $\mathrm{FSR}_l = 3.17\,\mathrm{MHz}$ respectively. The peaks at lower periodicity in the FFT, are harmonics of these two main contributions. The harmonics are expected to show up in the FFT since the peaks in the decay rates are not sinusoidal, but have a more complicated structure. We conclude that the observed spectrum is described by the qubit weakly coupling to transversely and longitudinally polarized phonons.

Since the transduction experiment is designed around longitudinally polarized phonons, we are interested in their coherence and coupling strengths. For this we record another spectrum, with smaller frequency range, but higher resolution. The fitted decay rates to this spectrum are plotted in Figure 5.10. Looking at this data carefully, we can match the features to the observed periods in the FFT. It turns out that the transversely polarized modes consist of a triple peak structure, with a broad central feature, a more narrow feature to its left and a tiny feature to its right. We mark these features in cyan and observe that most of the spectrum is covered with some part of them. On the other hand, the peaks corresponding to longitudinally polarized phonons (red patches) are

narrower and oftentimes appear on top of transverse peaks. To analyze the longitudinal peaks, we want to minimize the transversal background. For this we choose the two peaks marked with arrows, as they appear in conjunction with only the tiny transversal side peaks.

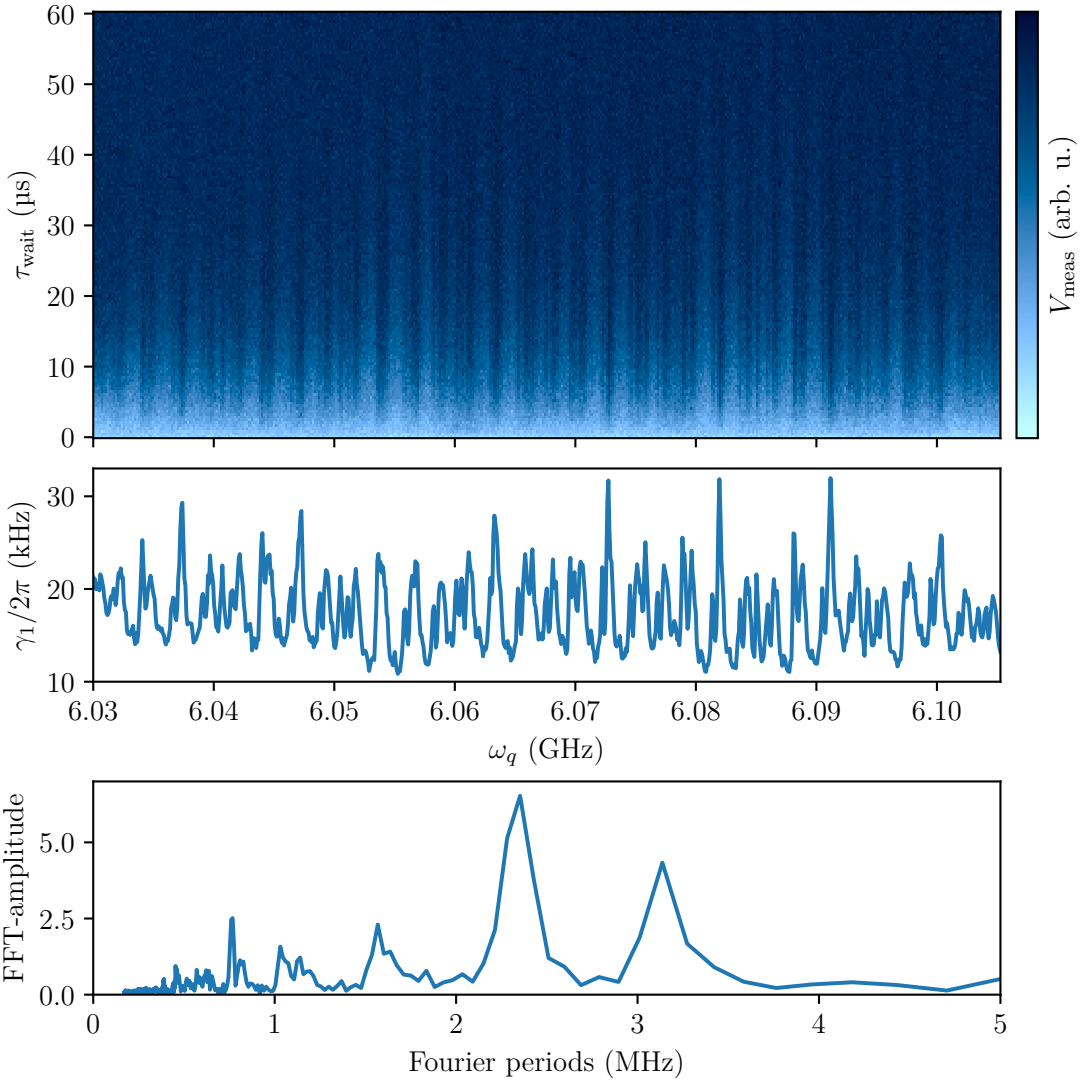

Figure 5.9.: T_1-spectrum (top), fitted decay rates (center), and FFT of decay rates (bottom) for CD 43.

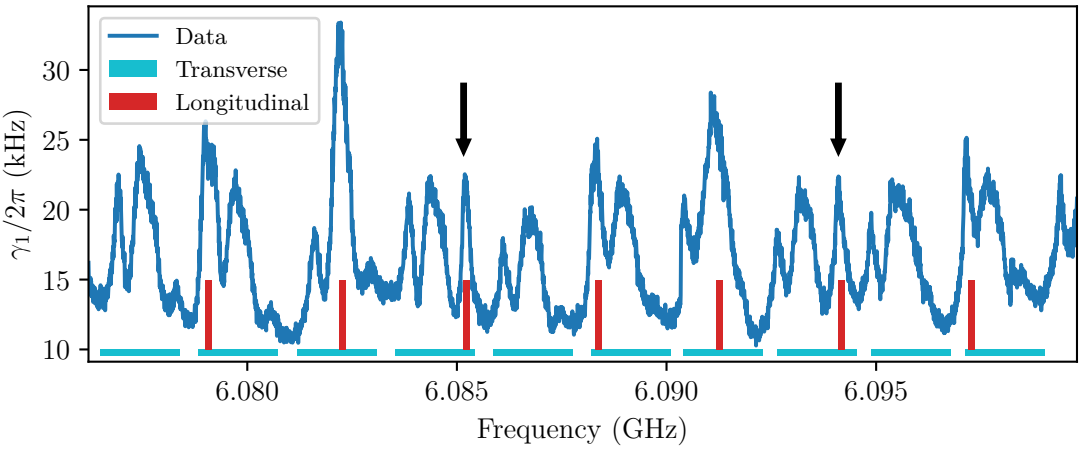

Figure 5.10.: Fitted decay rates to a second T_1-spectroscopy measurement of CD 43 with finer resolution and smaller frequency range. Features corresponding to transversely (longitudinally) polarized phonons are marked with cyan (red) patches. The two peaks to be analyzed are marked with arrows.

Spectra of CD 45

For CD 45 we again look at the spectrum (top), the fitted decay rates (center), and their FFT (bottom) in Figure 5.11. The data is recorded over a comparable frequency range as Figure 5.9, but the structure of the decay rates is notably different, as the peaks seem to appear much more frequently and regularly. From 6.040 GHz to 6.049 GHz, and from there to 6.058 GHz, we can see the background level increase. This is likely not a signature of qubit-phonon coupling, but rather of the measurement electronics, as the sudden jumps in decay rate coincide with frequencies, where individual measurements were concatenated. Looking at the FFT of the decay rates confirms, that a single periodicity at 1.2 MHz and its harmonics dominate the spectrum. In fact no signs of the expected FSRs for longitudinally and transversely polarized phonons can be found in the FFT.

To interpret this, we again look at a spectrum with smaller frequency range and higher resolution, and plot the decay rates in Figure 5.12. We clearly see the peaks occurring at the expected periodicity. Looking at the peak shapes, we can distinguish between two types, which we mark in red and cyan. The red peaks are broader and have somewhat of a double peak structure, while the red ones are narrower with a broader bottom. If we assume the peaks to have different physical origin, i.e. corresponding to different phonon modes, we notice that each of them appears at the periodicity of transversely polarized phonons $\mathrm{FSR}_t = 2.34\,\mathrm{MHz}$. Since red peaks appear right at the center between cyan peaks and vice versa, this periodicity does not show up in the FFT, but only the joint periodicity of 1.2 MHz.

From this data, we can conclude that in this device the qubit couples to two kinds of

transversely polarized modes, but not to longitudinally polarized ones.

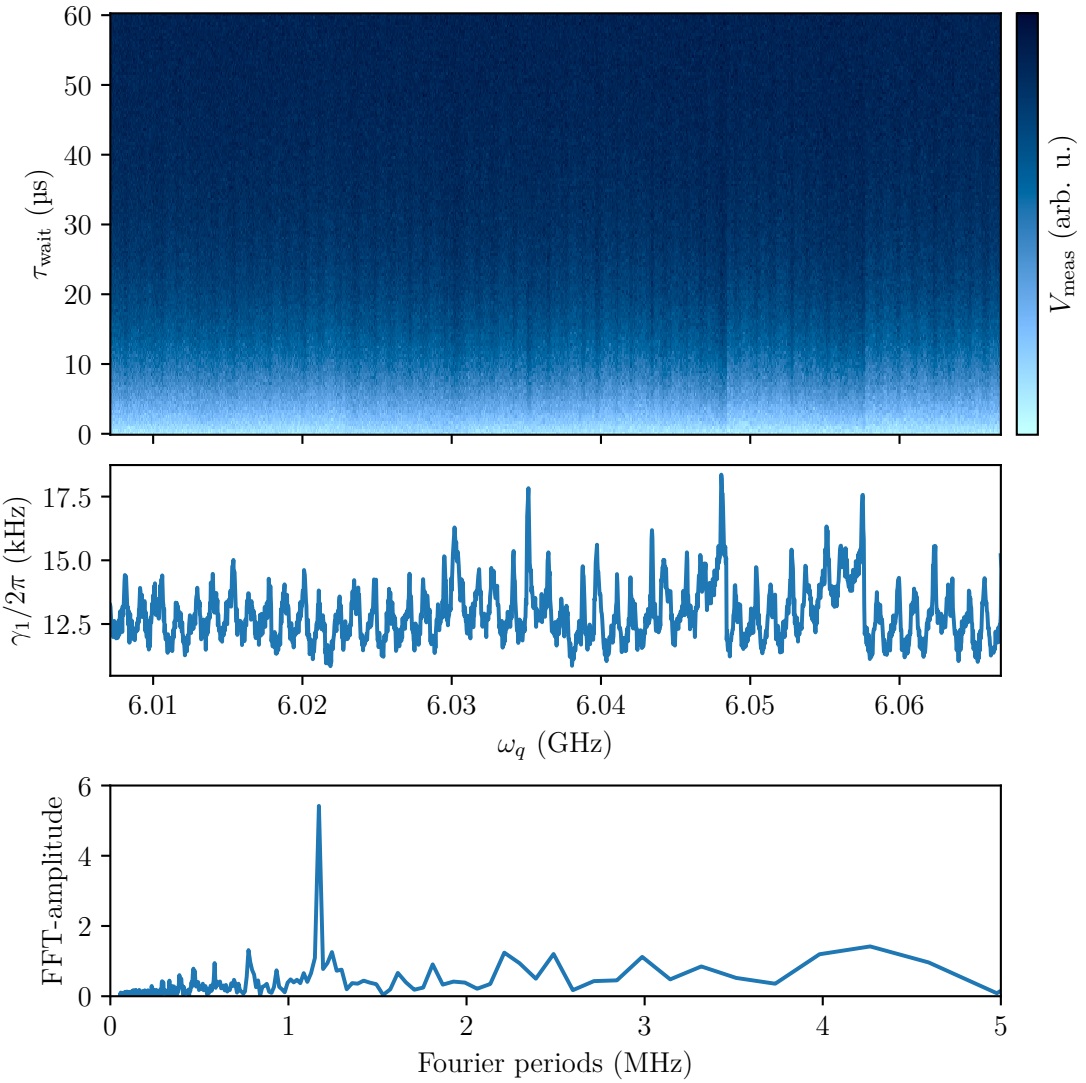

Figure 5.11.: T_1-spectrum (top), fitted decay rates (center), and FFT of decay rates (bottom) for CD 45.

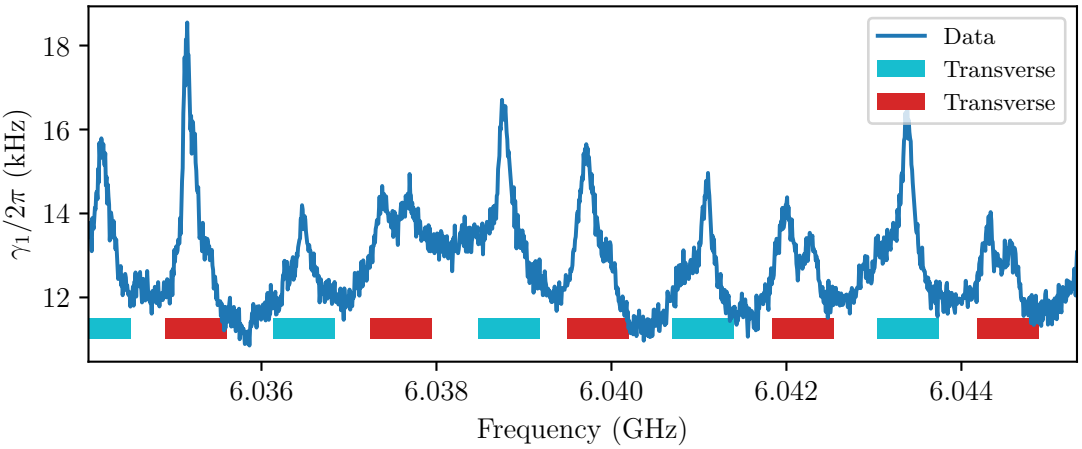

Figure 5.12.: Fitted decay rates to a second T_1-spectroscopy measurement of CD 45 with finer resolution and smaller frequency range. There are two types of features, marked with cyan and red patches, which correspond to transversely polarized phonons

5.4. Analysis of longitudinally polarized phonon modes

In the spectra of CD 38 and CD 43, we were able to find two peaks in decay rates each, corresponding to longitudinally polarized phonons. More precisely, corresponding to a longitudinal mode number of longitudinally polarized photons. As we saw in Subsection 2.1.2, for each longitudinal mode number, there exists a set transverse modes. For the cylinder HBAR, these are the described by the Bessel functions of the first kind. This means that the peaks in decay rates combine information about the coupling to a set of transverse eigenmodes.

The goal of this section is to fit Equation 5.2 to the peaks in decay rates and to extract values for $g_{e,m}$ and $\kappa_{2,m}$, where m labels the transverse eigenmodes of the HBAR. By making assumptions and including simulations in the analysis, we will reduce the number of fit parameters to four for each peak. To verify if the extracted fit parameters accurately describe the dynamics of the system, we will then simulate the system in QuTiP using these parameters. This will also help us to estimate the contributions of phonon and qubit decoherence to $\kappa_{2,m}$.

5.4.1. Fitting results

To start, we simulate the transverse mechanical eigenmodes in DASE (see Subsection 3.1.2) with the geometry parameters of the HBAR (see Table 5.1) and the frequencies 11.415 GHz (6.090 GHz) for CD 38 (CD 43). This gives us the mode functions as well as their detunings Δ_m from the fundamental mode. The frequency of the fundamental mode ω_0 will then serve as a fit parameter. Additionally we perform an eigenmode

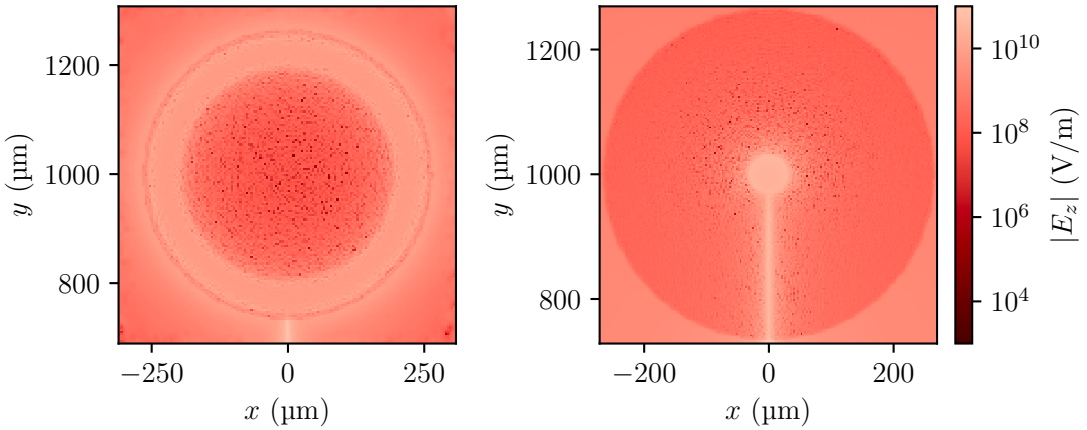

Figure 5.13.: Electric field inside the AlN cylinder for CD 38 (left) and CD 43 (right), simulated in Ansys.

simulation of the two devices in Ansys HFSS (see Subsection 3.1.1), which allows us to extract the qubit electric field inside the AlN cylinder. This is shown in Figure 5.13 for the two devices. One can see the different antenna shapes and how their sizes compare to the cylinder, which has a radius of $r_{\text{cut}} = 266\,\mu\text{m}$. The electric field increases outside of this radius because of the material boundary. Using Equation 2.13, we then calculate the electromechanical couplings $g_{\text{e},m}^{\text{sim}}$. The absolute values of these couplings usually deviate significantly from the experiment. To account for this, we normalize them by the total coupling $g_{\text{e,tot}}^{\text{sim}} = \sqrt{\sum_m^N \left(g_{\text{e},m}^{\text{sim}}\right)^2} = 2\pi \cdot 403\,\text{kHz}$ ($2\pi \cdot 158\,\text{kHz}$) with $N = 12$ (7) for CD 38 (CD 43). The number of modes N was chosen such that the mode frequencies match the frequency range where we will perform the fit. This leaves us to use a scaling factor $g_{\text{e,tot}}$ as a fit parameter. In order to further decrease the number of fit parameters, we have to make an assumption about the decoherence rates of the phonons. We do not have a good way of simulating the scaling of the decoherence with mode number, which is why we choose the simplest possible model, assuming equal decoherence, Γ_2, for all modes. The parameters $\kappa_{2,m}$ in Equation 5.2 thus become independent of the mode number, $\kappa_{2,m} = \gamma/2 + \gamma_\phi + \Gamma_2$.

Having reduced the number of fit parameters using simulations and assumptions, we fit the following function to the data,

$$\gamma_1(\omega_q) = \gamma + g_{\text{e,tot}}^2 \sum_{m=0}^{N-1} \frac{2(g_{\text{e},m}^{\text{sim}}/g_{\text{e,tot}}^{\text{sim}})^2\,(\gamma/2+\kappa)}{(\gamma/2+\kappa)^2 + (\omega_q - (\omega_0 + \Delta_m))^2}. \tag{5.6}$$

The fit parameters are the intrinsic qubit relaxation rate, γ, the frequency of the fundamental mode, ω_0, the total coupling rate, $g_{\text{e,tot}}$, and a decoherence rate $\kappa = \gamma_\phi + \Gamma_2$. Figure 5.14 shows the experimental data (blue) together with the fit (red) and the frequency interval (black), where the fit was performed. Additionally the fitted couplings

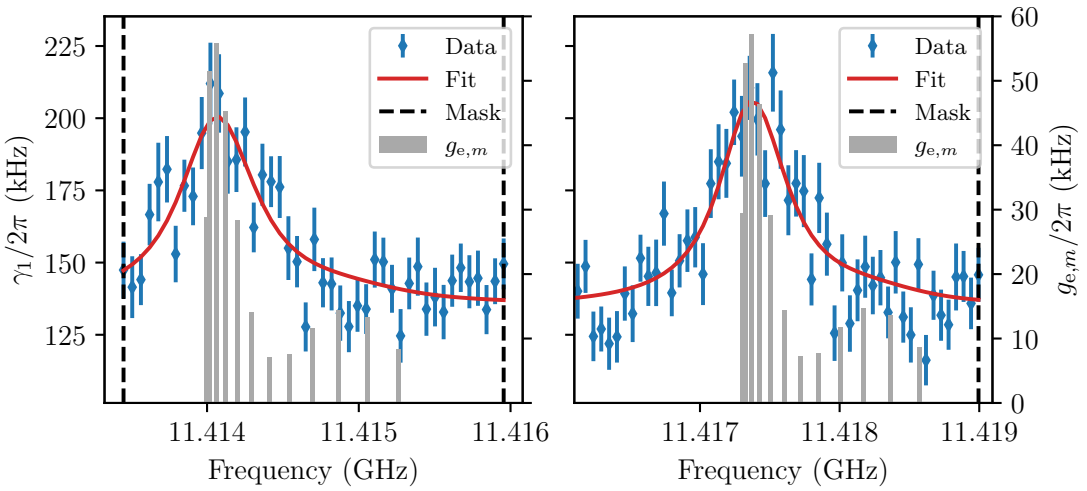

Figure 5.14.: Experimental data (blue), fitting function (red), fitting interval (black), fitted couplings (gray) of the two peaks of CD 43.

$g_{e,m} = g_{e,tot}(g^{sim}_{e,m}/g^{sim}_{e,tot})$ are plotted as gray bars. The fit is able to match the experimental data well, with the caveat that the data set is rather sparse and has large errorbars. The fit itself is reminiscent of a single Lorentzian, which is because the most strongly coupled modes are much closer in frequency than the overall width of the peak.

In Figure 5.15 the results for CD 43 are plotted. The data set is much richer in this case, and we can clearly see deviations from the fit to the data at similar positions in both peaks. The most prominent deviation is at the zenith of the peak, where the data increases to values of γ_1, which are approximately 2 kHz larger than in the fit. A potential reason for this deviation is the transversal background. Comparing with Figure 5.10, this background indeed has an extent of about 2 kHz. A second deviation is observed at the fifth mechanical mode, where the fit goes to higher values than the data. This deviation and parts of the first deviation, could be caused by the simplifying assumption of equal decoherence rates for all phononic modes. A higher decoherence rate of the fifth mode would decrease the amplitude and increase the width of the Lorentzian caused by this mode, and could thus be more consistent with the data. At last, mechanical modes without rotational symmetry could play a role in CD 43. The qubit electric field is notably asymmetric due to the antenna lead, as well as a slight misalignment of the antenna to the HBAR center, which is not captured by our model. This could also be a reason for the deviations.

All values extracted from the fits are presented in Table 5.3. We can now check if the condition $\Gamma_m > g_{e,tot} > \gamma$, for Equation 5.2 to be valid, is satisfied so that our analysis is self-consistent. Assuming sufficiently large contribution of phonon relaxation to κ, the condition is satisfied for both peaks in CD 43. For the peaks in CD 38 the condition is violated, as $\gamma > g_{e,tot}$, so that the fitting result violates the assumptions.

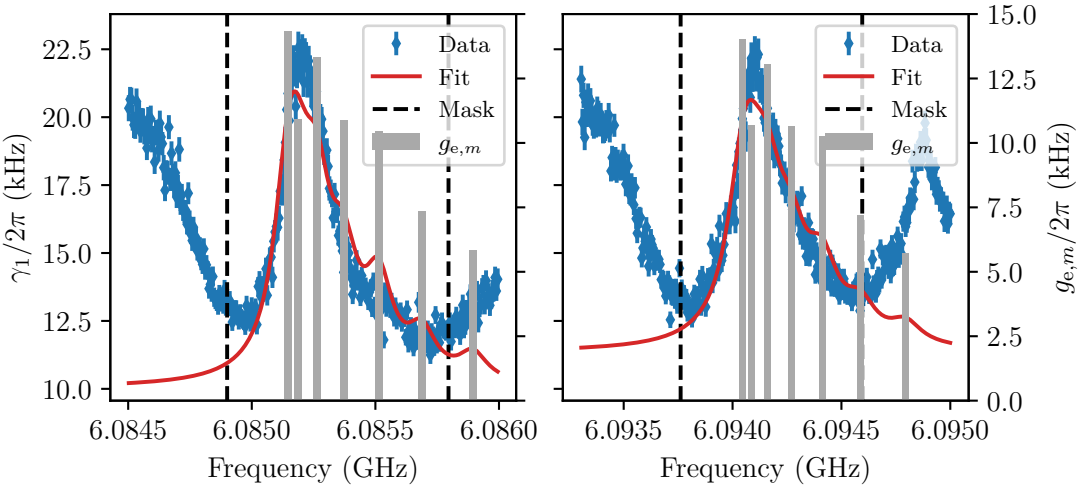

Figure 5.15.: Experimental data (blue), fitting function (red), fitting interval (black), fitted couplings (gray) of the two peaks of CD 43.

peak label	CD 38-1	CD 38-2	CD 43-1	CD 43-2
$\gamma/2\pi$ (kHz)	135±4	134.4±2.2	10.02±0.23	11.34±0.22
$\omega_0/2\pi$ (GHz)	11.41400	11.41730	6.085147	6.094046
$g_{e,tot}/2\pi$ (kHz)	102±9	104±7	28.6±0.8	28.0±0.8
$\kappa/2\pi$ (kHz)	220±60	200±50	64±6	80±7

Table 5.3.: Parameters from fitting Equation 5.6 to the data in Figure 5.8 and Figure 5.10. Errors for ω_0 are smaller than the given digits.

5.4.2. Further analysis using QuTiP simulations

We will now further investigate the validity of our fitting results with QuTiP master equation simulations of the Hamiltonian in Equation 5.1 using the extracted fit parameters. The simulations, as well as the independently measured qubit dephasing rates (Table 5.2), will help us to set bounds on the contributions of γ_ϕ and Γ_2 to the fit parameter κ. For simplicity we will assume zero phonon dephasing, as it is usually weak in HBARs [44]. This means that the phonon relaxation rate is $2\Gamma_2$.

A lower bound $\gamma_{\phi,\text{lower}}$ on qubit dephasing is set by the measurements of the unbonded qubit. For CD 38, we have to use $\gamma_{\phi,\text{lower}} = 0$ as there is no available data. For the upper bound, $\gamma_{\phi,\text{upper}}$, we use the minimum between κ and the measurements of the bonded sample for now. We refine the value by checking for consistency between experimental and simulation data.

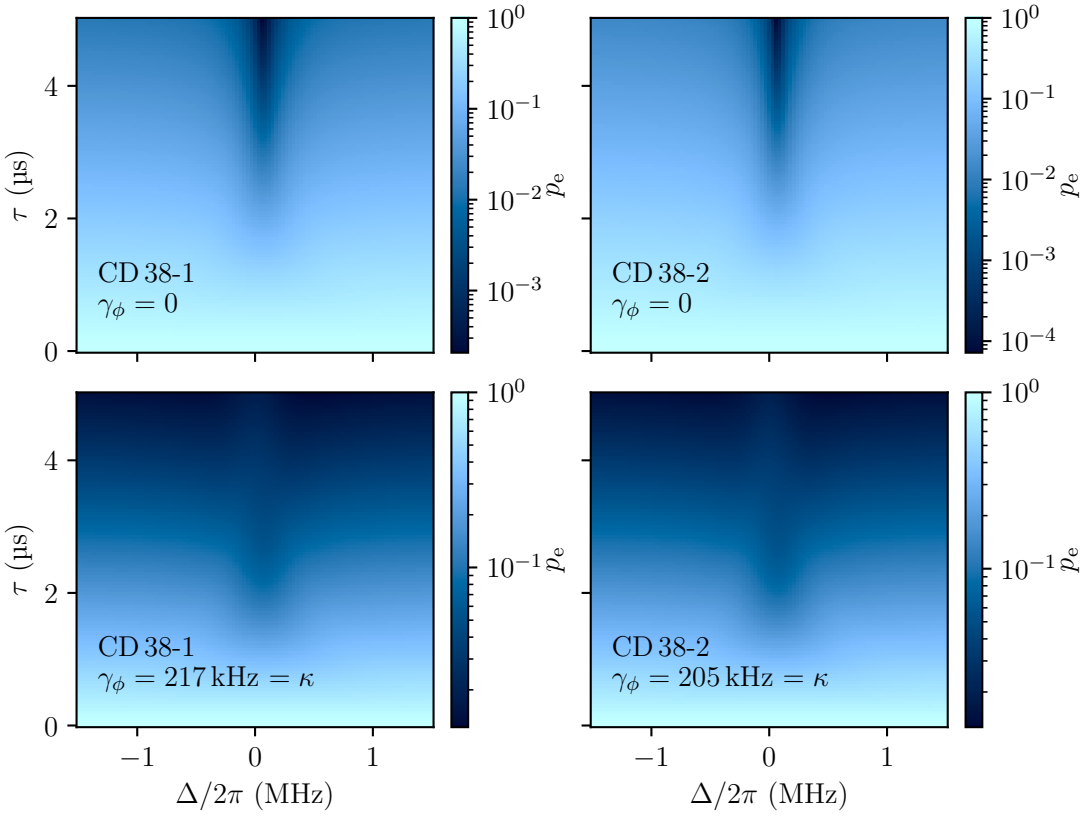

Figure 5.16.: Simulated time dynamics of the qubit population for the peaks CD 38-1 (left column) and CD 38-2 (right column). The top (bottom) row assumes minimal (maximal) qubit dephasing.

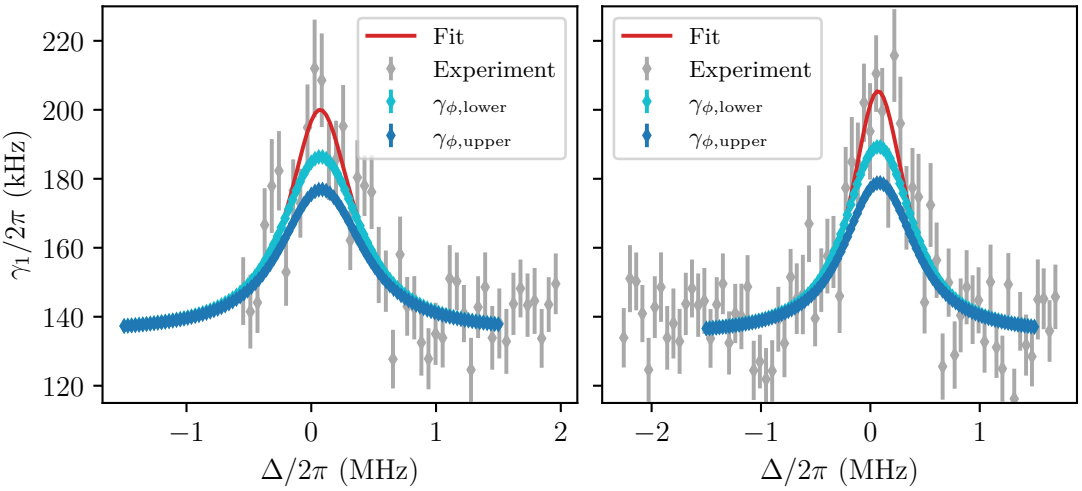

Figure 5.17.: Simulated decay rates of peaks CD 38-1 and CD 38-2 for $\gamma_\phi = \gamma_{\phi,\text{lower}} = 0$ (cyan) and $\gamma_\phi = \gamma_{\phi,\text{upper}} = \kappa$ (blue). The simulated data do not reproduce the function (red), that was fit to the experimental data (gray), rendering Equation 5.2 invalid for this parameter regime.

Simulations of CD 38

Using seven mechanical modes, we simulate the time dynamics of the the peaks from CD 38 for both bounds on γ_ϕ. Figure 5.16 shows the simulated qubit excited state population p_e as a function of interaction time τ and detuning Δ from ω_0. The top row shows the case of zero qubit dephasing, where the time dynamics are exponential. In the bottom row maximal qubit dephasing is assumed. On resonance the the time dynamics are not quite exponential, as the color seems to not change much beyond $\tau = 2\,\mu\text{s}$. We still fit an exponential decay,

$$p_e(\tau) = \exp(-\Gamma\tau), \tag{5.7}$$

to the simulation data and plot the results in Figure 5.17 (blue and cyan diamonds) together with the fitting result from Figure 5.14 (red) and the experimental data (gray). As expected, neither of the simulation results are consistent with the fit, as the system is in a regime, where the fit function is not valid. The simulation results in lower decay rates than the experimental data, but only close to resonance.

At this point, it becomes hard to analyze the data, as all relevant time scales are presumably on the same order of magnitude. One option would be a brute force sweep of the simulation parameters $g_{e,\text{tot}}$, Γ_2, and γ_ϕ, to see if we can find a set of parameters, which is consistent with the experimental data. This was unfortunately out of the scope of this thesis, which is why we have to leave the measurement unconcluded.

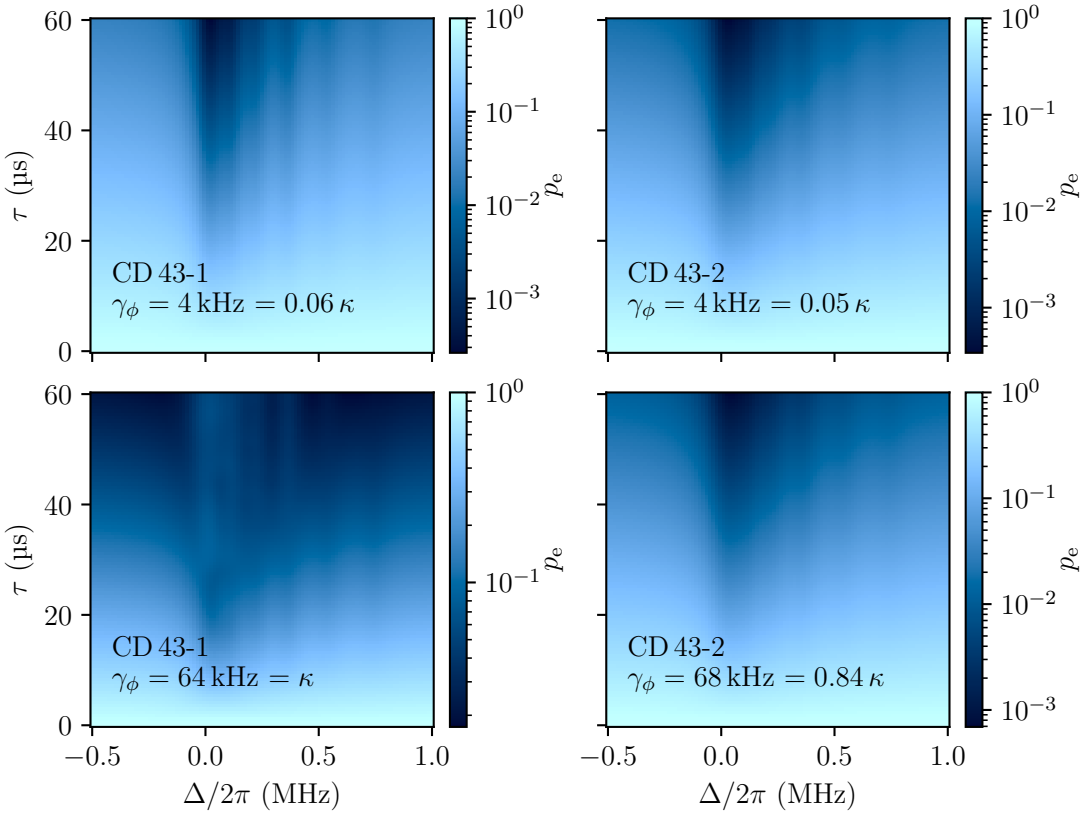

Figure 5.18.: Simulated time dynamics of the qubit population for the peaks CD 43-1 (left column) and CD 43-2 (right column). The top (bottom) row assumes minimal (maximal) qubit dephasing.

Simulations of CD 43

For CD 43, we simulate the time dynamics of the system with six mechanical modes. Figure 5.18 shows the simulated qubit population for both bounds of γ_ϕ for both peaks. The time dynamics are exponential for all panels but the bottom left, which shows the simulation for peak CD 43-1 for $\Gamma_2 = 0$ and $\gamma_\phi = \kappa$. There we see the qubit population slightly increase again after $\tau = 30\,\mu\mathrm{s}$ on resonance. This behavior is not consistent with the experimental data, where only exponential decay is observed.

To find a threshold of γ_ϕ, where the simulation data is consistent with exponential decay, we simulate the time dynamics of peak CD 43-1 at ω_0, sweeping γ_ϕ/κ. We fit Equation 5.7 to each time trace and plot the summed residuals of the fit in Figure 5.19. We can see a clear onset of increasing residuals, after which the simulation is less well described by an exponential decay. We choose $\gamma_{\phi,\mathrm{upper}}/\kappa = 0.91$ as the threshold value, which is still consistent with exponential decay. At this threshold, we simulate again the dynamics of CD 43-1, and fit the decay rates for each detuning.

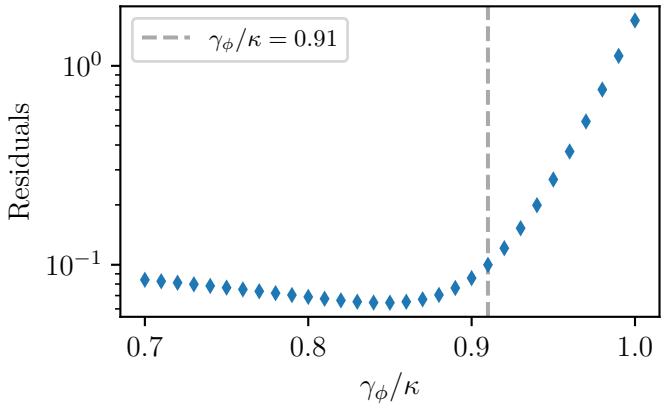

Figure 5.19.: Summed residuals of exponential fits to qubit population at $\Delta = 0$ for CD 43-1. As the contribution of γ_ϕ to κ increases, we observe an onset at the threshold value.

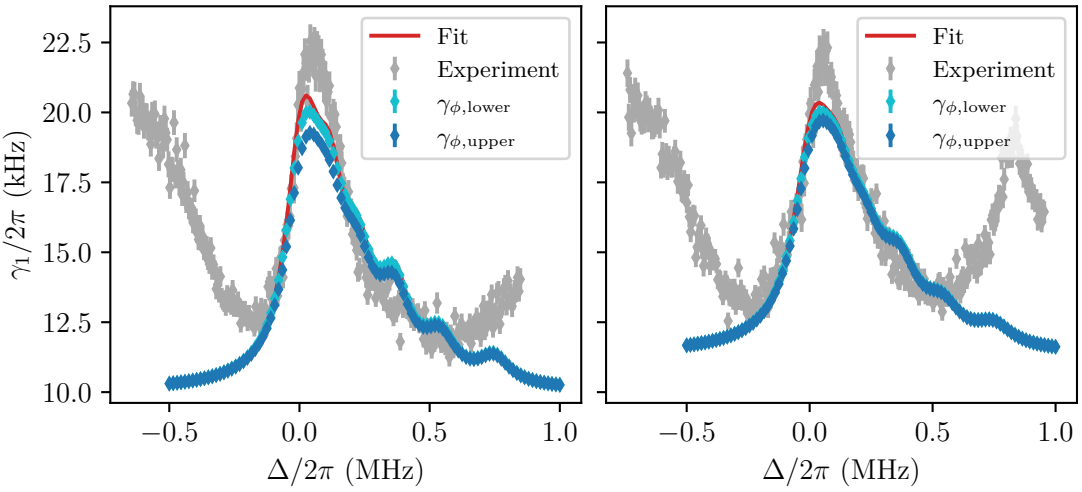

Figure 5.20.: Simulated decay rates of peaks CD 43-1 and CD 43-2 for $\gamma_\phi = \gamma_{\phi,\text{lower}}$ (cyan) and $\gamma_\phi = \gamma_{\phi,\text{upper}}$ (blue). The simulated data match the function (red), that was fit to the experimental data (gray) quite well, rendering the model self-consistent.

Figure 5.20 shows the fitted decay rates for both peaks and both bounds of γ_ϕ (blue and cyan), as well as the fitting result (red) from Figure 5.15 and the experimental data (gray). The simulated data agree reasonably well with the fitting function, which means that both boundaries lead to the dynamics observed in the experiment. Note that for the case of qubit dephasing assuming $\gamma_{\phi,\mathrm{upper}}$, Γ_2 falls short of $g_{\mathrm{e,tot}}$, meaning Equation 5.2 is not in a valid regime. This does not take away from the fact, that these parameters are still able to approximately reproduce the fitting result in the simulations.

The resulting intervals of γ_ϕ and Γ_2 which are consistent with the measurements of CD 43 are presented in Table 5.4. Since we assumed no phonon dephasing in the simulations, we calculate the phonon relaxation rate as $T_1 = (2\Gamma_2)^{-1}$.

peak label	CD 38-1	CD 38-2
$\gamma_\phi/2\pi$ (kHz)	$(3.7 \pm 2.2, 58 \pm 6)$	$(3.7 \pm 2.2, 67.5 \pm 1.7)$
$\Gamma_2/2\pi$ (kHz)	$(5.7 \pm 0.6, 60 \pm 7)$	$(13 \pm 7, 76 \pm 7)$
T_1 (µs)	$(1.32 \pm 0.16, 14.0 \pm 1.5)$	$(1.05 \pm 0.10, 6.1^{+7.2}_{-2.2})$

Table 5.4.: Intervals of qubit dephasing rates and phonon coherences, which are consistent with the measurements of CD 43. Errors with a ±-sign are calculated with linear error propagation. Errors of the upper bound on T_1 for CD 38-2 are assuming the plus and minus values of the Error on Γ_2 respectively.

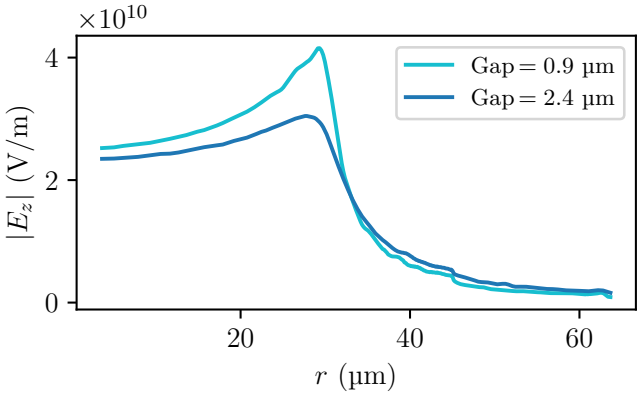

Figure 5.21.: Ansys simulation of E_z inside the AlN cylinder for the two gap sizes between qubit chip and HBAR, averaged over the angle coordinate.

5.4.3. Absence of longitudinally polarized phonons in CD 45

After having the longitudinally polarized phonon modes in devices CD 38 and CD 43, it is left to ask why we did not observe any longitudinally polarized modes in CD 45. We can be sure that the sample did not unbond, since we obseved transversely polarized phonons. Thus, the only possible reason for not observing longitudinally polarized phonons are high decoherence rates or low electromechanical couplings to these modes. This would cause the signatures of phonon enhanced qubit decay to be very broad and low in amplitude, such that they effectively form a uniform background. We can identify potential reasons for this behavior by looking at the differences between the two HBARs (see Table 5.1). The two HBARs follow the same design, nevertheless there were differences regarding the material quality and fabrication process.

The first difference to notice is the gap size between qubit chip and the AlN cylinder. To see the effect on the qubit electric field, we simulate the two geometries in Ansys and plot the electric field inside the AlN cylinder in Figure 5.21. There is indeed a slight difference in the magnitude of the electric field. But this difference cannot account for an orders of magnitude change in electromechanical coupling strength, which would be necessary to explain the absence of longitudinally polarized modes.

The second difference lies in the surface roughness of the samples. The higher roughness of CD 45 could lead to increased surface loss of the phonons. This seems to be the most likely reason for not observing coupling to longitudinally polarized phonons. We can estimate roughly what this would mean for the T_1 of a longitudinally polarized phonon. Let us assume, the enhancement of qubit decay rate due to longitudinally polarized phonons is less the $\Delta\gamma_1 = 2\pi \cdot 1\,\mathrm{kHz}$, because otherwise we would have been able to detect it. For a single mechanical mode, the enhancement of qubit decay rate is given by (see. Equation 5.2),

$$\Delta\gamma_1 = 4g_e^2 T_1, \tag{5.8}$$

on resonance, assuming that the phonon decoherence rate dominates the total decoher-

ence of the coupled system. In CD 43, the fundamental mode couples to the phonons with about $g_{e,0} = 2\pi \cdot 14\,\mathrm{kHz}$ (see Figure 5.15), which we also assume for this estimate. This lets us conclude that,

$$T_1 < \frac{\Delta\gamma_1}{4g_e^2} \approx 0.18\,\mu\mathrm{s}, \tag{5.9}$$

for the case that high phonon loss due to surface roughness is the correct explanation for not observing longitudinally polarized phonons in CD 45.

Which ever physical mechanism is responsible for not being able to observe longitudinally polarized phonons, it is apparent that this mechanism does not suppress the transversely polarized modes in the same way, as we can clearly see enhanced qubit decay due to these modes.

5.5. Analysis of transversely polarized phonon modes

Transversely polarized modes, were observed in the spectra of CD 43 and CD 45, but not in CD 38. Since these modes are not relevant for the transduction experiment, we will only do a qualitative analysis here.

The first question that comes to mind is how the mode shapes and polarizations look like. One can think of several possibility here. In general the mode shapes have to depend on the polarization. A mode with linear transversal polarization will experience similar boundary conditions as the longitudinally polarized one. One could also think of modes with polarizations in radial (breathing mode) or angular (twisting mode) direction. These modes must have zero amplitude at the center of the HBAR because of their symmetry. The dominant strain components of transversely polarized modes are the S_{xz} and S_{yz} components. Using the same arguments as in Subsection 2.2.1, we can deduce that the E_x/E_y components of the qubit electric field dominantly couple to linearly polarized modes with x/y polarization, and the E_r/E_ϕ components dominantly couple to breathing/twisting modes, where r, ϕ are the polar coordinates of the cylinder.

In CD 43/CD 45, we observed that transversely polarized modes come in families with frequency splitting between the members. Recall the triple peak structure in CD 43 and the alternation of peaks with cyan and red coloring in CD 45. A similar observation was made in reference [53], where acoustic radiation of a superconducting qubit into sapphire HBARs was investigated. The authors observe coupling to two kinds of transversely polarized phonons with a small frequency splitting, $\Delta\omega$, and they attribute this splitting to a slight angle, $\Delta\theta$, between the crystal's c-axis and the geometrical z-axis of the device. Looking back at Figure 2.1, this explanation also holds for quartz. The two branches of transversely polarized phonons only overlap precisely at the the q_z-axis of the velocity surface. For $\Delta\theta \neq 0$, there are two transversal phase velocities, giving rise to two distinct FSRs and thus to a frequency splitting. Following the authors formula,

$$\frac{\Delta\omega}{\omega} = \Delta\theta \frac{2|C_{14}|}{C_{44}}, \tag{5.10}$$

where C is the stiffness tensor, the splittings are consistent with

$$\Delta\theta_{43} = 0.012^\circ, \tag{5.11}$$
$$\Delta\theta_{45} = 0.018^\circ. \tag{5.12}$$

where we assumed a splitting of $\Delta\omega_{43} = 2\pi \cdot 0.8\,\mathrm{MHz}$ between the central and left feature of transversal phonons for CD 43, and $\Delta\omega_{45} = 2\pi \cdot 1.2\,\mathrm{MHz}$ for CD 45. Unfortunately, we do not have specifications from the manufacturers of the quartz wafers on their accuracy when it comes to that angle. It still seems reasonable to attribute the observed splitting to such an angle mismatch. The existence of the triple peak structure in CD 43, remains unexplained.

At last, we can ask ourselves, why there was no sign of transversely polarized phonons in CD 38. Although the data set was quite sparse, the measured frequency range should have been enough to observe these modes. There are two differences between CD 38 and the other devices, the operation frequency and the antenna geometry. The frequency could play a role if the loss mechanism for transversely polarized phonons scales strongly with frequency such that these modes are so lossy at high frequency, that they are not observed. A second effect of the frequency difference is related to the AlN thickness, which was optimized for longitudinally polarized phonons at the Brillouin frequency, $\Omega_B = 12.64\,\mathrm{GHz}$ in all devices. The AlN thickness is thus too large for optimal coupling to the shorter wavelength transversely polarized modes at high frequency in CD 38, but too small for optimal coupling to the lower frequency transversely polarized modes in CD 43 and CD 45. This means that coupling to longitudinally polarized phonons is favored in the higher frequency device, while coupling to transversely polarized modes is not. The perhaps stronger effect comes from the ring geometry of the qubit antenna. The transversal electric field components, which drive transversely polarized phonons, are always pointing outwards of the ring. This means that above the ring, the electric field changes sign rather quickly through space, posing strict requirements on the symmetry of phonon modes it can couple to.

Overall, the transversely polarized phonons are undesired for the transduction experiment, as they introduce additional loss into the system. Not observing them in CD 38 is a promising sign, that they will not be the limitation of future transduction experiments.

5.6. Discussion of the results

Let us now discuss the implications of these results for moving closer towards the goal of microwave to optical transduction of single photons. It is apparent that the overall volume of results is very underwhelming. Only one of the three measured devices, CD 43, could provide meaningful values for electromechanical coupling rates and phonon lifetimes, of which the latter could fall within the range of one order of magnitude. Moreover, the device CD 43 that was able to provide these values has significant differences in design to the final transduction device regarding antenna geometry and operation frequency. It is fair to say that the measurements of especially CD 38 and to an extend

CD 43 were limited by qubit decoherence. A lower qubit dephasing rate in CD 43 would have set stricter bounds on phonon lifetimes or even enabled vacuum Rabi oscillation, depending on the true phonon lifetime. In CD 38, the high qubit decay rate prohibited the usage of an analytical treatment entirely. It is thus crucial for future experiments to reliably produce high coherence qubits, especially for high frequencies. CD 45 was likely not limited by qubit decoherence, but by phonon decoherence due to increased surface roughness, as we were able to detect longitudinally polarized phonons in CD 43 with the same qubit.

An alternative way to collect data on quality factors of HBARs, is to bond them to a microwave antenna and measure their frequency response with a vector network analyzer. The phononic resonances appear as notches in the reflected signal, whose lineshapes determine the internal and external quality factors of the HBAR [54]. This kind of measurement has the advantage of being able to collect information over a broad frequency range, without having to rely on qubit coherence times. The group attempted such a measurement of a cylinder HBAR without success, due to low signal to noise ratio as well as problems in the measurement electronics that were only later resolved.

In spite of the low yield of the measurements, we can still draw conclusions. Unfortunately, we were not able to extract reliable values for the electromechanical couplings in CD 38. This would be desirable, in order to do simulations on further optimization of the device. We can make a very rough estimate by comparing the simulated couplings $g_{\mathrm{e,tot}}^{\mathrm{sim}}$ for the two devices CD 38 and CD 43 (see Subsection 5.4.1) and assume their ratio $r \approx 2.5$ to be somewhat reasonable. Using then the measured values from CD 43, we can estimate $g_{\mathrm{e,tot}} \approx 2\pi \cdot 75\,\mathrm{kHz}$ for the ring antenna geometry. This is the value we used for geometry optimizations in Section 3.3. As we saw in Figure 3.7, the corresponding electromechanical swap time is $t_{\mathrm{sw}} \approx 4\,\mu\mathrm{s}$, which sets requirements on qubit coherence times for the transduction experiment.

For the electromechanical, but especially for the optomechanical interaction, sufficient phonon lifetimes are required. In the optimized cylinder HBAR design, the optomechanical interaction takes more than 15 µs (see Figure 3.7). The measured interval of phonon lifetimes, $1\,\mu\mathrm{s} < T_1 < 14\,\mu\mathrm{s}$, in CD 43 is thus not sufficient, already at this low frequency of 6 GHz. Going to higher frequencies (Ω_B), phonon lifetimes are not expected to increase but rather to fall off [55]. Looking additionally at CD 45, where phonon lifetimes were too low to even be measured, it becomes clear that the current cylinder HBARs are not good enough for the transduction protocol they were designed for. Besides qubit fabrication, we thus identified the lacking phonon life times in cylinder HBARs as the factor limiting progress. Because of the groups experience in fabrication of high quality dome HBARs [23, 44] and an improved recipe for fabricating domes with large radius of curvature, we made a decision, to move to dome HBARs for the next iteration of devices. This will hopefully allow us to observe vacuum Rabi oscillations at the Brillouin frequency.

6. Conclusion and Outlook

The first part of this thesis investigated the implications of operating a quantum transducer with multiple intermediary oscillators. We saw that the transduction process with multiple mechanical modes is dictated by the time evolution of the mechanics. This is in contrast to a single mode transducer, which uses one mechanical eigenmode. Optimizing the transduction efficiency is thus a matter of engineering the mechanical mode spectrum, which we did for rotationally symmetric HBARs with various simulation methods in Chapter 3. We concluded that achieving perfect mechanical rephasing is not possible for this symmetry. In Chapter 4, we approached the system from another angle, investigating the properties of an idealized transducer with just two mechanical modes. The double-well HBAR could approximately resemble this two mode structure, but came at the cost of unreasonably long transduction times. From these two chapters we concluded that perfect rephasing has to be realized with more than two mechanical modes. An elongated harmonic dome could potentially be a good candidate for this. A more general approach for achieving perfect transduction efficiency is to find a way to model the multimode transducer as a chain of bosonic quantum channels as mentioned in the introduction. For these systems, a generalized matching condition of system parameters has been derived, which allows for unity transduction efficiency at a certain frequency [11]. Looking even a step further, a multimode transducer is in principle able to outperform a single mode transducer, because it is able to reach a higher quantum capacity for a given coupling rate [13].

In practice, progress in the transduction experiment is currently not limited by the rephasing of mechanical states. As we saw in Chapter 5, we are currently unable to reach the strong coupling regime of cQAD with HBARs with cylinder piezo shapes, which is a basic requirement for the transduction experiment. From the measurement of three $\hbar$BAR devices, we concluded that both qubit and HBAR coherence times need to improve to reach the strong coupling regime at the Brillouin frequency. For this reason, we decided to transition to spherical cap domes, where the team is able to consistently achieve high mechanical quality factors. As we saw in Section 3.3, this piezo shape is only slightly disadvantageous compared to the cylinder in terms of transduction efficiency. Together with recent progress in qubit fabrication, reaching electromechanical strong coupling at the Brillouin frequency in transduction $\hbar$BARs is within sight.

Acknowledgments

First and foremost, I would like to thank Prof. Yiwen Chu for giving me the opportunity to conduct this project in her group. Ever since the start of my studies in my Bachelor's, I was fascinated by mechanics because it felt so close to reality. The mechanical systems I studied in my Master's Thesis feel very far from reality as they behave in a quantum mechanical way. Thank you Prof. Chu for doing such a good job of giving a lecture on this fascinating field of quantum acoustics and Optomechanics. It was honestly the best module of my studies here at ETH.

I also want to commend the group environment. From the very start, all group members were dedicated to create an enjoyable environment for the new Master students. Asking questions was always welcomed and encouraged. I had lots of fun at the group events. At Christmas dinner, I had the best Chinese food of my life. The bench press competition and the ping pong tournament were also great events, although I wasn't able to beat Dominic in the finals. He is just too good.

I have to give a huge thank you especially to the members of the transduction team. Everyone in that team is incredibly skilled, and everyone was very willing to share their knowledge with me. Rodrigo introduced me to the procedure of performing measurements with the dilution refrigerator setup, Tom "the fridgemaster" showed me all the components of the inside of the fridge and helped me a lot with Ansys and coding, Max has an incredible overview over the literature and helped me with basically every aspect of my thesis, and finally Sam, my supervisor, had a similar way of thinking about physics as me, which made it really pleasant to discuss. Thank you for always being there to listen and to help me move forward at the pace that was good for me. I really have to commend you for not putting pressure or expectations on me, because I was already putting them on myself. At times I had to take time off to rest, and you always made it clear that I should prioritize feeling healthy over forcing myself to work. When the time was right, you gave great input and ideas on simulations that could be interesting and it was very fun discussing the results with you.

At last, I must not forget my family and friends. Traveling home to my parents always felt like a safespace during this intense time of my life. My friends at home always welcomed me with a warm heart. Having very close friends here in Zurich was essential to enjoying my time. I will never forget living with my flatmates. It was probably the best form of cohabitation imaginable and I got to see so much of Switzerland because of you. Finally, I want to give a massive thank you to my fellow physics student friends. Our energy was always very positive and uplifting. Spending time with you got me to discover many great things like volleyball, Doppelkopf, or UK garage music. To finish, I want to especially highlight my good friend Casimir, who was always there to cheer me up with a joke when it was adequate and also when it was not.

Bibliography

[1] A. Blais, A. L. Grimsmo, S. M. Girvin, and A. Wallraff, "Circuit quantum electrodynamics," *Rev. Mod. Phys.*, vol. 93, p. 025005, May 2021.

[2] J. M. Martinis, M. H. Devoret, and J. Clarke, "Quantum josephson junction circuits and the dawn of artificial atoms," *Nature Physics*, vol. 16, no. 3, pp. 234–237, 2020.

[3] S. Storz, J. Schär, A. Kulikov, P. Magnard, P. Kurpiers, J. Lütolf, T. Walter, A. Copetudo, K. Reuer, A. Akin, *et al.*, "Loophole-free bell inequality violation with superconducting circuits," *Nature*, vol. 617, no. 7960, pp. 265–270, 2023.

[4] H. Takesue, S. D. Dyer, M. J. Stevens, V. Verma, R. P. Mirin, and S. W. Nam, "Quantum teleportation over 100 km of fiber using highly efficient superconducting nanowire single-photon detectors," *Optica*, vol. 2, pp. 832–835, Oct 2015.

[5] H. J. Kimble, "The quantum internet," *Nature*, vol. 453, no. 7198, pp. 1023–1030, 2008.

[6] C. Simon, "Towards a global quantum network," *Nature Photonics*, vol. 11, no. 11, pp. 678–680, 2017.

[7] O. c. v. Černotík and K. Hammerer, "Measurement-induced long-distance entanglement of superconducting qubits using optomechanical transducers," *Phys. Rev. A*, vol. 94, p. 012340, Jul 2016.

[8] E. Zeuthen, A. Schliesser, A. S. Sørensen, and J. M. Taylor, "Figures of merit for quantum transducers," *Quantum Science and Technology*, vol. 5, no. 3, p. 034009, 2020.

[9] X. Deng, S. Li, Z.-J. Chen, Z. Ni, Y. Cai, J. Mai, L. Zhang, P. Zheng, H. Yu, C.-L. Zou, *et al.*, "Quantum-enhanced metrology with large fock states," *Nature Physics*, pp. 1–7, 2024.

[10] D. J. Brod, E. F. Galvão, A. Crespi, R. Osellame, N. Spagnolo, and F. Sciarrino, "Photonic implementation of boson sampling: a review," *Advanced Photonics*, vol. 1, no. 3, p. 034001, 2019.

[11] C.-H. Wang, M. Zhang, and L. Jiang, "Generalized matching condition for unity efficiency quantum transduction," *Phys. Rev. Res.*, vol. 4, p. L042023, Nov 2022.

[12] C. Zhong, X. Han, and L. Jiang, "Microwave and optical entanglement for quantum transduction with electro-optomechanics," *Phys. Rev. Appl.*, vol. 18, p. 054061, Nov 2022.

[13] C.-H. Wang, F. Li, and L. Jiang, "Quantum capacities of transducers," *Nature Communications*, vol. 13, no. 1, p. 6698, 2022.

[14] Y. Chu and S. Gröblacher, "A perspective on hybrid quantum opto- and electromechanical systems," *Applied Physics Letters*, vol. 117, p. 150503, 10 2020.

[15] R. Sahu, L. Qiu, W. Hease, G. Arnold, Y. Minoguchi, P. Rabl, and J. M. Fink, "Entangling microwaves with light," *Science*, vol. 380, no. 6646, pp. 718–721, 2023.

[16] A. Kumar, A. Suleymanzade, M. Stone, L. Taneja, A. Anferov, D. I. Schuster, and J. Simon, "Quantum-enabled millimetre wave to optical transduction using neutral atoms," *Nature*, vol. 615, no. 7953, pp. 614–619, 2023.

[17] M. Eichenfield, J. Chan, R. M. Camacho, K. J. Vahala, and O. Painter, "Optomechanical crystals," *nature*, vol. 462, no. 7269, pp. 78–82, 2009.

[18] M. Mirhosseini, A. Sipahigil, M. Kalaee, and O. Painter, "Superconducting qubit to optical photon transduction," *Nature*, vol. 588, no. 7839, pp. 599–603, 2020.

[19] F. M. Mayor, S. Malik, A. G. Primo, S. Gyger, W. Jiang, T. P. M. Alegre, and A. H. Safavi-Naeini, "A two-dimensional optomechanical crystal for quantum transduction," in *Quantum 2.0 Conference and Exhibition*, p. QTu4A.3, Optica Publishing Group, 2024.

[20] R. Delaney, M. Urmey, S. Mittal, B. Brubaker, J. Kindem, P. Burns, C. Regal, and K. Lehnert, "Superconducting-qubit readout via low-backaction electro-optic transduction," *Nature*, vol. 606, no. 7914, pp. 489–493, 2022.

[21] M. B. Kristensen, N. Kralj, E. C. Langman, and A. Schliesser, "Long-lived and efficient optomechanical memory for light," *Phys. Rev. Lett.*, vol. 132, p. 100802, Mar 2024.

[22] Y. Chu, P. Kharel, T. Yoon, L. Frunzio, P. T. Rakich, and R. J. Schoelkopf, "Creation and control of multi-phonon fock states in a bulk acoustic-wave resonator," *Nature*, vol. 563, no. 7733, pp. 666–670, 2018.

[23] M. Bild, M. Fadel, Y. Yang, U. Von Lüpke, P. Martin, A. Bruno, and Y. Chu, "Schrödinger cat states of a 16-microgram mechanical oscillator," *Science*, vol. 380, no. 6642, pp. 274–278, 2023.

[24] P. Kharel, G. I. Harris, E. A. Kittlaus, W. H. Renninger, N. T. Otterstrom, J. G. E. Harris, and P. T. Rakich, "High-frequency cavity optomechanics using bulk acoustic phonons," *Science Advances*, vol. 5, no. 4, p. eaav0582, 2019.

[25] H. M. Doeleman, T. Schatteburg, R. Benevides, S. Vollenweider, D. Macri, and Y. Chu, "Brillouin optomechanics in the quantum ground state," *Phys. Rev. Res.*, vol. 5, p. 043140, Nov 2023.

[26] F. I. Fedorov, *Theory of elastic waves in crystals*. Springer Science & Business Media, 2013.

[27] J. W. Jaeken and S. Cottenier, "Solving the christoffel equation: Phase and group velocities," *Computer Physics Communications*, vol. 207, pp. 445–451, 2016.

[28] G. G. Gurzadyan and P. Tzankov, *Dielectrics and Electrooptics*, pp. 817–901. Berlin, Heidelberg: Springer Berlin Heidelberg, 2005.

[29] T. Schatteburg, *In preparation*. PhD thesis, ETH Zürich, 2025.

[30] Y. Chu, P. Kharel, W. H. Renninger, L. D. Burkhart, L. Frunzio, P. T. Rakich, and R. J. Schoelkopf, "Quantum acoustics with superconducting qubits," *Science*, vol. 358, no. 6360, pp. 199–202, 2017.

[31] A. J. O. Röell, "Design and microfabrication of high-overtone bulk acoustic resonators," Master's thesis, ETH Zürich, 2023.

[32] M. A. M. Marte and S. Stenholm, "Paraxial light and atom optics: The optical schrödinger equation and beyond," *Phys. Rev. A*, vol. 56, pp. 2940–2953, Oct 1997.

[33] P. Kharel, Y. Chu, M. Power, W. H. Renninger, R. J. Schoelkopf, and P. T. Rakich, "Ultra-high-q phononic resonators on-chip at cryogenic temperatures," *APL Photonics*, vol. 3, p. 066101, 05 2018.

[34] C. Gerry and P. Knight, *Field quantization*, p. 10–42. Cambridge University Press, 2004.

[35] H. Banderier, M. Drimmer, and Y. Chu, "Unified simulation methods for quantum acoustic devices," *Phys. Rev. Appl.*, vol. 20, p. 024024, Aug 2023.

[36] A. Vives, *Piezoelectric Transducers and Applications*. Springer Berlin Heidelberg, 2008.

[37] P. Muralt, J. Conde, A. Artieda, F. Martin, and M. Cantoni, "Piezoelectric materials parameters for piezoelectric thin films in ghz applications," *International Journal of Microwave and Wireless Technologies*, vol. 1, no. 1, p. 19–27, 2009.

[38] L. B. Herrmann, "Simulations and measurements of high-frequency transmons for a quantum transduction experiment," Master's thesis, ETH Zürich, 2024.

[39] P. Zhao, T. Ma, Y. Jin, and H. Yu, "Combating fluctuations in relaxation times of fixed-frequency transmon qubits with microwave-dressed states," *Phys. Rev. A*, vol. 105, p. 062605, Jun 2022.

[40] R. H. Brown and R. Q. Twiss, "Correlation between photons in two coherent beams of light," *Nature*, vol. 177, no. 4497, pp. 27–29, 1956.

[41] A. Uhlmann, "The transition probability in the state space of a $\star$-algebra," *Reports on Mathematical Physics*, vol. 9, no. 2, pp. 273–279, 1976.

[42] Ansys Contributors, "Ansys hfss: Best-in-class 3d high frequency structure simulation software." https://www.ansys.com/products/electronics/ansys-hfss, 2025.

[43] Z. K. Minev, Z. Leghtas, S. O. Mundhada, L. Christakis, I. M. Pop, and M. H. Devoret, "Energy-participation quantization of josephson circuits," *npj Quantum Information*, vol. 7, no. 1, p. 131, 2021.

[44] Y. Yang, I. Kladarić, M. Drimmer, U. von Lüpke, D. Lenterman, J. Bus, S. Marti, M. Fadel, and Y. Chu, "A mechanical qubit," *Science*, vol. 386, no. 6723, pp. 783–788, 2024.

[45] D. Barthlott, "Optimized grayscale lithography for double-sided bulk acoustic wave resonators," Master's thesis, ETH Zürich, 2025.

[46] G. Grynberg, A. Aspect, and C. Fabre, *Complement 2C: The density matrix and the optical Bloch equations*, p. 140–166. Cambridge University Press, 2010.

[47] R. Barends, J. Kelly, A. Megrant, D. Sank, E. Jeffrey, Y. Chen, Y. Yin, B. Chiaro, J. Mutus, C. Neill, P. O'Malley, P. Roushan, J. Wenner, T. C. White, A. N. Cleland, and J. M. Martinis, "Coherent josephson qubit suitable for scalable quantum integrated circuits," *Phys. Rev. Lett.*, vol. 111, p. 080502, Aug 2013.

[48] M. Odeh, K. Godeneli, E. Li, R. Tangirala, H. Zhou, X. Zhang, Z.-H. Zhang, and A. Sipahigil, "Non-markovian dynamics of a superconducting qubit in a phononic bandgap," *Nature Physics*, pp. 1–6, 2025.

[49] P. Krantz, M. Kjaergaard, F. Yan, T. P. Orlando, S. Gustavsson, and W. D. Oliver, "A quantum engineer's guide to superconducting qubits," *Applied Physics Reviews*, vol. 6, p. 021318, 06 2019.

[50] R. Setty, "Iq mixers, image reject down-conversion and single sideband (ssb) up-conversion." https://blog.minicircuits.com/iq-mixers-image-reject-down-conversion-single-sideband-ssb-up-conversion/, 2022.

[51] Qunatum Machines Contributers, "Qop conceptual overview." https://docs.quantum-machines.co/1.2.2/docs/Introduction/qop_overview/, 2025.

[52] S. W. Jolin, R. Borgani, M. O. Tholén, D. Forchheimer, and D. B. Haviland, "Calibration of mixer amplitude and phase imbalance in superconducting circuits," *Review of Scientific Instruments*, vol. 91, Dec. 2020.

[53] V. Jain, V. D. Kurilovich, Y. D. Dahmani, C. U. Lei, D. Mason, T. Yoon, P. T. Rakich, L. I. Glazman, and R. J. Schoelkopf, "Acoustic radiation from a superconducting qubit: From spontaneous emission to rabi oscillations," *Phys. Rev. Appl.*, vol. 20, p. 014018, Jul 2023.

[54] S. Probst, F. B. Song, P. A. Bushev, A. V. Ustinov, and M. Weides, "Efficient and robust analysis of complex scattering data under noise in microwave resonators," *Review of Scientific Instruments*, vol. 86, p. 024706, 02 2015.

[55] A. A. Maznev, "Boundary scattering of phonons: Specularity of a randomly rough surface in the small-perturbation limit," *Phys. Rev. B*, vol. 91, p. 134306, Apr 2015.

A. Estimate on experimentally achievable optomechanical coupling

The experimentally achievable optomechanical coupling is limited by the laser power used to pump the lower frequency optical mode. The coupling to a single mechanical mode n is given by

$$g_{\mathrm{o},n}^2 = \frac{4Pg_{0,n}^2\kappa_{\mathrm{ext}}}{\hbar\omega\kappa^2}, \tag{A.1}$$

where P is the laser power, ω the laser frequency, $g_{0,n}$ the single photon coupling, κ_{ext} the output coupling of the optical cavity, and κ the linewidth of the optical cavity. We assume the largest value of $g_{0,n} = 2\pi \cdot 7.5\,\mathrm{Hz}$ observed in [25], and a ratio of $\kappa_{\mathrm{ext}}/\kappa = 0.9$ with $\kappa = 2\pi \cdot 1\,\mathrm{MHz}$. From input-output theory we get the reflection coefficient of the pump light at the optical cavity $R_p = \left(1 - 2\frac{\kappa_{\mathrm{ext}}}{\kappa}\right) = 0.64$. Our filter cavity setup attenuates the pump light by 120 dB and signal photons by 3 dB. The average number of pump photons incident on the SPDs per transduction sequence is then

$$N_p = 10^{-12}\frac{PR_p t_{\mathrm{OM}}}{\hbar\omega}, \tag{A.2}$$

where $t_{\mathrm{OM}} = 25\,\mu\mathrm{s}$ is the pulse length of the pump laser. The average number of signal photons is

$$N_s = 10^{-0.3}\frac{\kappa_{\mathrm{ext}}}{\kappa}\eta_t = \eta_{\mathrm{tot}} = 0.27, \tag{A.3}$$

where $\eta_t = 0.6$ is the transduction efficiency simulated in Section 3.3. Requiring a signal to pump ration of $SPR = N_s/N_p = 10$, we calculate the allowed pump power to be

$$P = 10^{12}\frac{\hbar\omega\eta_{\mathrm{tot}}}{R_p t_{\mathrm{OM}}}\frac{1}{SPR} = 217\,\mu\mathrm{W}, \tag{A.4}$$

while the pulse is on. Plugging this into Equation A.1, we get $g_{\mathrm{o},n} = 2\pi \cdot 233\,\mathrm{kHz}$.

B. Calibration measurements

Here we show for completeness the calibration measurements for CD 38 (see Figure B.1) and CD 45 (see Figure B.2). The measurements are standard for the most part. In CD 38, the notch of qubit spectroscopy is comparatively small because of poor qubit coherence times. In CD 45 The cavity spectroscopy does not extend to the same amplitude as the other measurements. This is because a different readout amplitude was chosen for the other measurements. In the T_2^*-Ramsey-measurement, we can observe a beatnote. It is unclear, what causes this. Multiple T_2^*-Ramsey-measurements (not shown here) were performed at different qubit frequencies, which the beating frequency was not affected by. To account for the beating, we include an additional cosine in the fitting function.

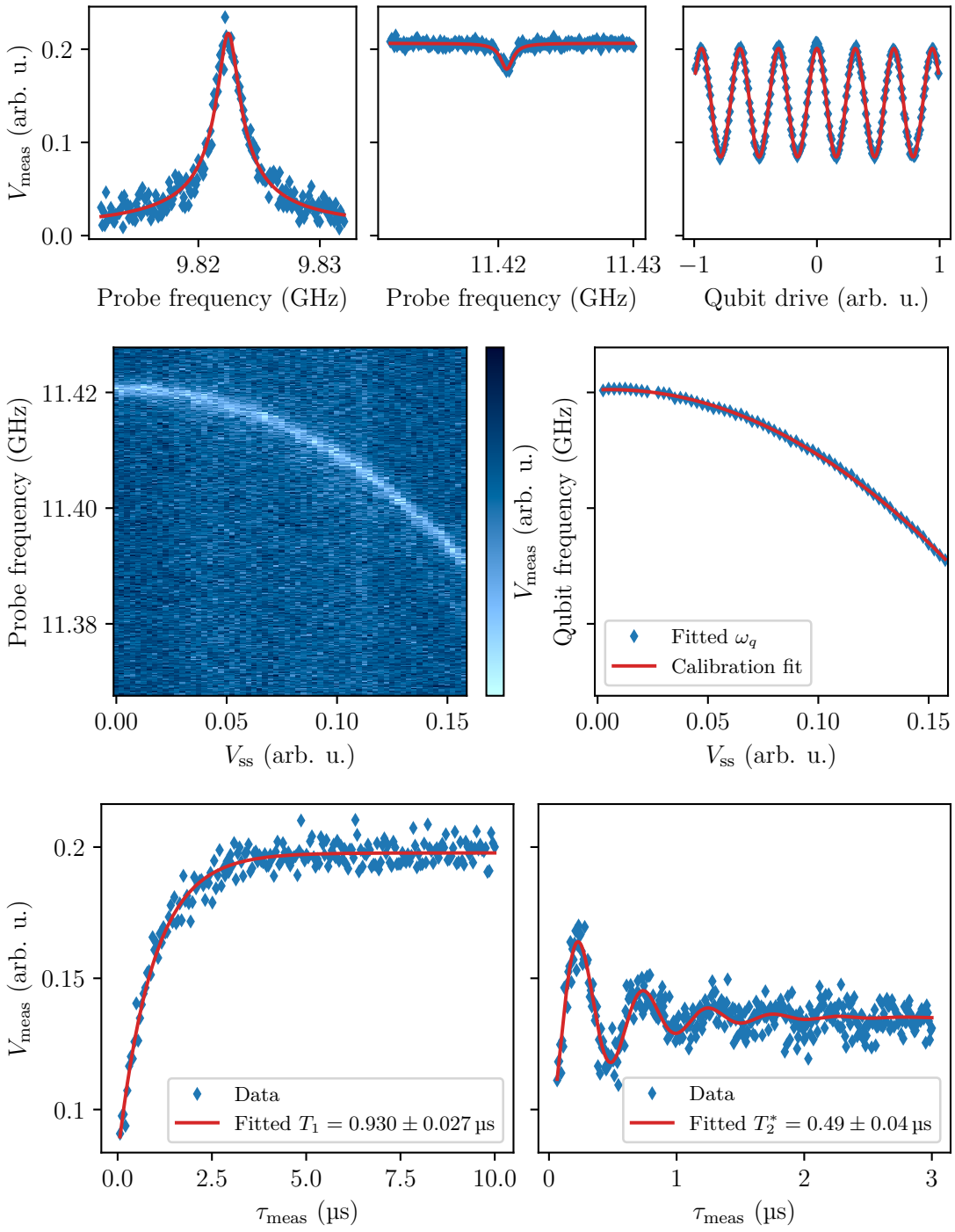

Figure B.1.: Calibration measurements of CD 38. From top left to bottom right: Cavity spectroscopy, qubit spectroscopy, Rabi measurement, Stark shift to frequency calibration, T_1-measurement, T_2^*-Ramsey-measurement.

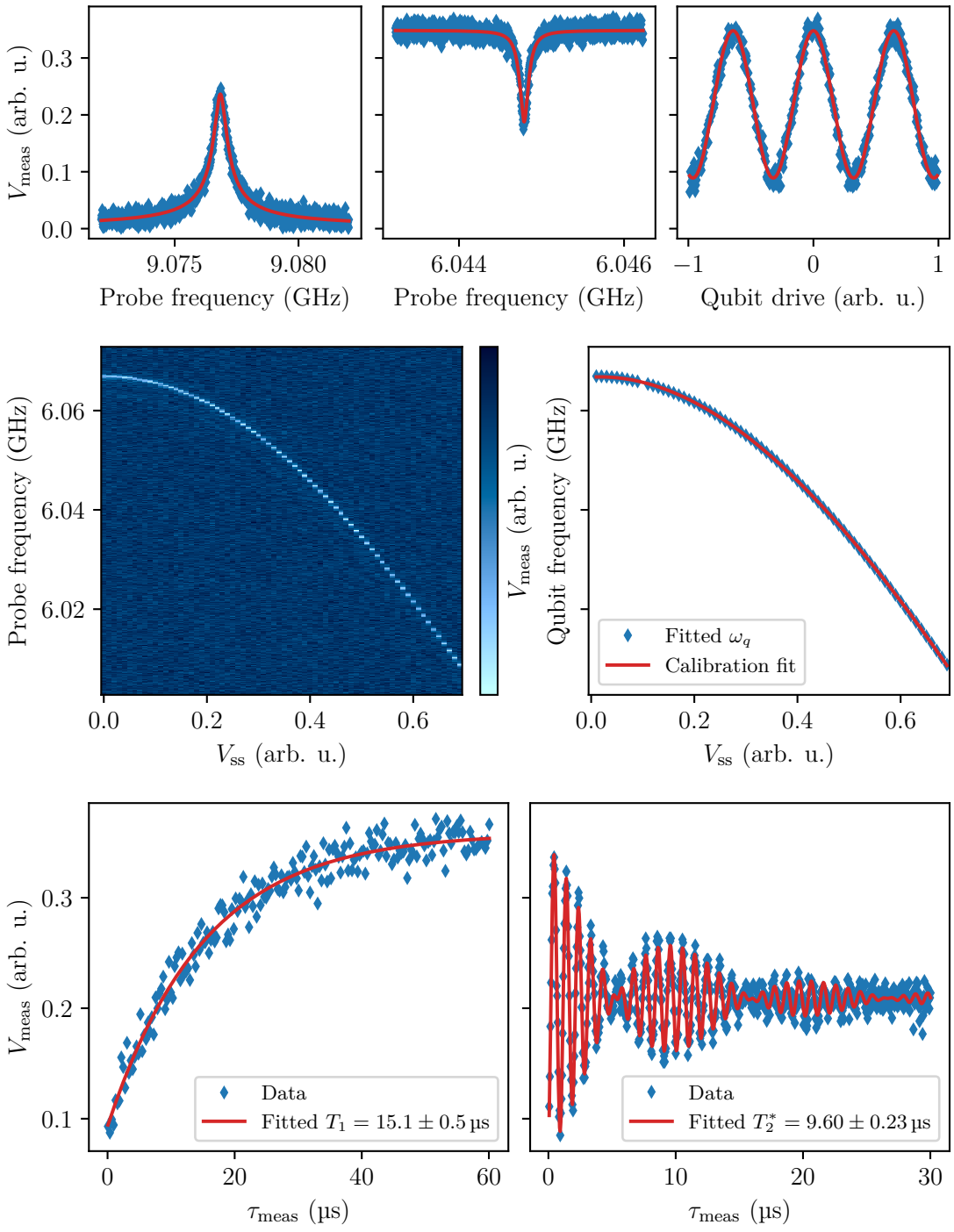

Figure B.2.: Calibration measurements of CD 45. From top left to bottom right: Cavity spectroscopy, qubit spectroscopy, Rabi measurement, Stark shift to frequency calibration, T_1-measurement, T_2^*-Ramsey-measurement.